THE EFFECT OF COOLING RATE ON THE MICROSTRUCTURE CONFIGURATION OF CONTINUOUSLY CAST STEEL SLABS

by

Mohammad Reza Allazadeh

B.S. in Mechanical Engineering, Miskolc University, Miskolc, Hungary, 1997

M.S. in Computer Aided Technology Planning, Miskolc University, Miskolc, Hungary, 1999

M. S. in Solid Mechanic Engineering, Brown University, Providence RI, 2004

Submitted to the Graduate Faculty of

Swanson School of Engineering in partial fulfillment

of the requirements for the degree of

Doctor of Philosophy in Mechanical Engineering

University of Pittsburgh

2009

UNIVERSITY OF PITTSBURGH

SWANSON SCHOOL OF ENGINEERING

This dissertation was presented

by

Mohammad Reza Allazadeh

It was defended on

January 12, 2009

and approved by

Dr. Issac C. Garcia, Research Professor, Mechanical Engineering and Materials Science

Dr. Anthony J DeArdo, Professor, Mechanical Engineering and Materials Science

Dr. Roy D. Marangoni, Emeritus Professor, Mechanical Engineering and Materials Science

Dissertation Director: Dr. Michael R. Lovell, Dean of the College of Engineering & Applied Science, University of Wisconsin-Milwaukee

THE EFFECT OF COOLING RATE ON THE MICROSTRUCTURAL CONFIGURATION OF CONTINUOUSLY CAST STEEL SLABS

Mohammad Reza Allazadeh, PhD

University of Pittsburgh, 2009

This research work is another step for increasing the efficiency and productivity of the steel making process by enhancing both quality and quantity of the steel produced by the Continuous Casting process. When steels cool from a high temperature, austenite transforms into other phase configurations according to the austenite composition and cooling rate. As result of phase transformation, the steel crystal structure and, consequently, both the shape and the lattice parameter of the unit cell, change. These changes may introduce dilatational strains into the microstructure, which result in the creation of residual stress concentration zones within the microstructure. These stress concentration zones are vulnerable regions to the formation of microcracks or growth of the flaws in these regions. The main objective of this dissertation is to develop a method to define the optimum cooling rate for cooling continuously as-cast steel on industrial level. An FEM algorithm developed with the ANSYS codes is introduced in this dissertation to simulate the cooling of as-cast steel from any temperature below the solidification temperature. The algorithm is capable of being customized to simulate the thermodynamic behavior of as-cast steel microstructure with any chemical composition and any casting geometry imposed to desired cooling method. The phase transformation simulations were based on the CCT diagram and, therefore, they were quasi-real models. The models predict, analytically, the generation of the stress concentration regions due to the thermodynamic strains during cooling a

sample from the austenite temperature range with different cooling rates. Another series of FEM models presented in this dissertation and post non-destructive tests (NDT) ultrasonic image analysis tests suggested in this work, can be used in the discussion of the effect of the cooling rate on the altering of the soundness of the tested steel. A combination of the suggested FEM algorithm and post image processing of NDT ultrasonic images along with laboratory cooling experiments and microstructural analysis provide a guideline to find the cooling rate for each grade of steel in the casting steel industry. Results of JMATPRO software also are deployed to increase the accuracy of the experimental set up and to obtain the required input data to run the proposed numerical algorithm cooling simulation.

TABLE OF CONTENTS

LIST OF TABLES

LIST OF FIGURES

ACKNOWLEDGEMENTS

Upon the successful completion of this research endeavor, first and foremost, I give praise to almighty God for empowering me with strength, wisdom, and tenacity to accomplish my long path of education toward my PhD degree. I would not be able to acknowledge all the scientists, advisors, academic instructors, friends and colleagues whose knowledge and inspiration during my academic education led me to this level of knowledge. My deepest gratitude goes to graduate committee members: Dr Michael R. Lovell, Dr Calixto I Garcia, Dr Roy Marangoni, and Dr Anthony J. DeArdo for supporting my PhD education. I am thankful to those in ANSYS Inc. who helped me in debugging my code. I extend my gratitude to Dr K. M. Goldman for proofreading this dissertation. I would also like to thank staff members of the administration of the Mechanical Engineering and Materials Science department for helping me during my education in the University of Pittsburgh.

I dedicate this dissertation to my parents, my wife and my sisters for all of their support, help and love.

1.0 INTRODUCTION

The continuing increase in the demand for steel around the world has been establishing the competition between countries and companies in producing steel. Figure 1 presents the fast growth of steel production since 1950 until 2005 around the world [1]. This annual increase in demand for steel and competition to dominate the market encouraged worldwide investment on research in increasing the production rate and lowering the cost of the final steel without sacrificing the quality of the steel.

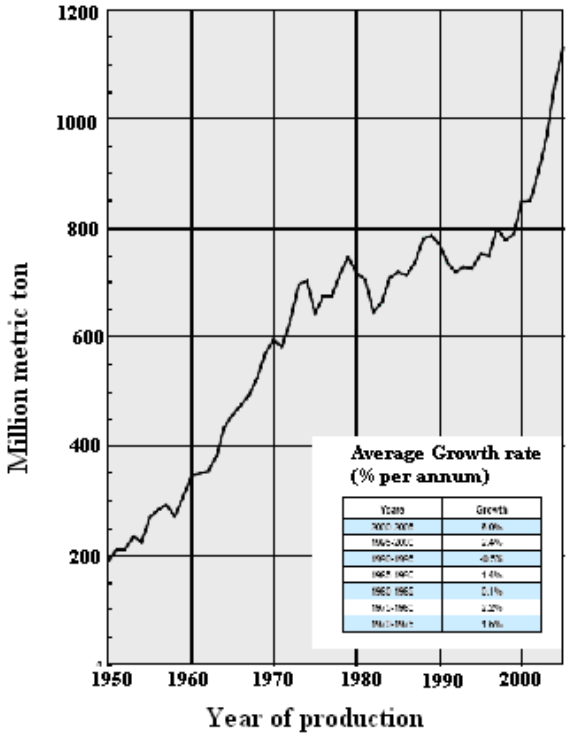

Year	World
2005	1,132
2004	1,067
2003	969
2002	904
2001	850
2000	848
1999	789
1998	777
1997	799
1996	750

Year	World
1995	752
1990	770
1985	719
1980	717
1975	644
1970	595
1965	456
1960	347
1955	270
1950	189

Figure 1 Production of crude steel in 1950-2005; source International Iron & Steel Institute.

Continuous casting, initially introduced in 1840, is an attractive method in mass producing semi-finished metal shapes (slabs, blooms, and billets) from molten metal. More than 50% of current world's steel production is produced by continuous casting. Thousands of experimental results and theoretical analyses led to higher profit for the steel industries and fast investment return by reducing the cost of the steel production process and shortening the inventory time of the steel in the production line. The last step of the process on continuous cast steel before delivery or further machining is to cool the hot solidified cast product to obtain desired microstructure. Imposing a high cooling rate to the hot slab decreases inventory cost by decreasing the storage time for cooling as-cast steel and making available the casting line for the next ladle of molten steel. It also increases productivity and gives faster return of investment. However, it might have disadvantages because of lowering soundness of the steel product due to formation of cracks and flaws because of thermal gradients and, especially, residual stresses generated by phase transformation. The attempt in this research work is to optimize the cooling rate for cooling the hot steel slab to low temperature for delivery or storage. Three temperature regions in the Fe-Fe_3C phase diagram may be considered based on the temperature of the as-cast steel prior to quenching. These temperature regions are super-critical (austenite-γ), sub-critical (ferrite-α) regions and inter-critical ($\gamma+\alpha$).

There are many developments with the sole purpose of maintaining and/or increasing high production rate. Most of these developments, supported by extensive research, have been aimed at increasing the sophistication of the continuous caster machine design and process controls in order to decrease the casting time. Despite all the efforts to maintain the high production rate, one area that has received limited attention is the investigation of changes in the defect density during the rapid cooling of slabs during the phase transformation of solid

(austenite) to solid (phase transformation products). For example, the following questions need to be addressed: what is the effect of accelerated cooling on the overall soundness of the slab when cooled from the supercritical, intercritical and/or subcritical temperatures at rates higher than air-cooling? What would be the difference in reaction of the inclusions if there is or is not bonding forces between inclusion and steel matrix during cooling? What is the interaction of inclusions with the steel matrix and interaction of different phases to each other during quenching? How the composition of the steel dictates the industrial optimum cooling rate? How can the formation of the flaw and micro-cracks be predicted and prevented during cooling process?

This research work is another step toward increasing the efficiency and productivity of the steel making process by enhancing both quality and quantity of the steel produced by the continuous casting process. Efficient cooling rates obtained for a specific grade of steel provide an increase in productivity of steel and a decrease in the inventory time of production of steel slabs, blooms, and billet without degrading the quality of the steel. Degradation of quality is a term that corresponds to any deviation from desirable composition; microstructure, application, commercial requirement specifications or chemical composition and mechanical properties, as well as corrosion or heat resistance and formability. Figure 2 summarizes, schematically, the objective of this dissertation. This optimum cooling rate must provide an increase in production rate without sacrificing the quality of the steel. The optimum cooling rate also lowers the final steel production cost in different ways, such as more efficient use of equipment in the production line, shortening the inventory level by shortening steel production line, lowering working temperature, lowering labor cost, less delays in the shipment and decreasing the waste cutting part of cast steel content undesirable defects formed during cooling of the hot as-cast steel.

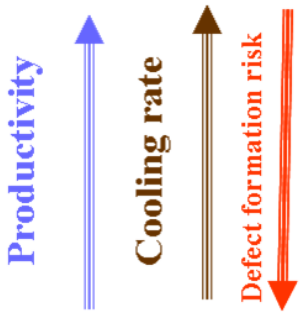

Figure 2 Optimum cooling rate of the as-cast slab based on the criteria of the objective of this dissertation.

On the other hand, too fast cooling may increase the yield loss. The critical cooling rate is subjected to different factors which some of them are discussed through chapters of this dissertation. In this research work, three grades of steel were tested in cooling experiments under laboratory conditions. Three grades of steel slab samples are designated as 1010, 1091 and 1319.

This research work proposes an ANSYS algorithm in combination with the non-destructive tests, NDT, and cooling experiments to study the effect of the cracks and inclusions on the cooling rate and to optimize cooling rate for cooling as-cast continuous cast slab steel. The extensive literature review on each of the mentioned topic is provided in the chapter 2. Chapter 3 lists the objectives of this dissertation. The numerical method and related formulas to the objectives are collected in the chapter 4. The results of ultrasonic tests and the post image processing of NDT developed for this research work are described in the chapter 5. Chapter 6 shows the finite element method (FEM) results of the interaction of inclusions with a steel matrix. The detail of experimental work is given in chapter 7. Chapter 8 is devoted for the cooling model based on the ANSYS algorithm developed in this dissertation to present the effect of the phase transformation on the defect density via generation of residual stress concentration zones in the microstructure of the steel. The proposed FEM algorithm to simulate the cooling as-cast steel from supercritical, intercritical and subcritical temperature ranges are presented in the

Chapter 9. Chapter 10 contains the summary and conclusions of the dissertation. Some future works on the topic of the objectives of this dissertation are mentioned in Chapter 11.

2.0 BACKGROUND

2.1 MICROSTRUCTURE OF STEEL

The microstructure of steel is responsible for the macro-behavior of steel or in other words steel's material properties. Understanding the concepts and phenomena related to microstructure helps to perceive the relation of defects characterization and solid-solid phase transformation with optimum cooling rate of as-cast slabs of specific steel grade. These topics, including microstructural phases, the steel classification and cleanliness of the steel, are defined briefly in this section.

It is general knowledge that the material components and their arrangement with respect to each other influence the material properties. Properties of elements and compositions in the microstructure and compositional arrangement in the microstructure define the properties of the unit cell in steel. The long-range arrangement of these units in a crystal structure determines local and global properties of the crystal built by these unit cells. The complexity of arrangement and variety of microstructure's unit cells are responsible for the difference between the properties of the unit cells and the properties of bulk material. These arrangements in the microstructure depend on the history of the material relevant to different phenomena such as previous mechanical and thermodynamic processes on the material. Unit cells with the same arrangement grouped in a single crystal are called grains and borders of this similar arrangement

of unit cells, are defined as grain boundaries. Properties of the collection of different crystals in polycrystalline material depend on grains and grain boundaries. These factors specify the steel's property as polycrystalline texture.

Different grades of steel have different material properties because they contain different chemical compositions. However, steels with the same grade experiencing a different heat treatment process or deformation processing have different properties.

2.1.1 Microstructural Phases

Low iron carbon alloys with carbon content between 0.02% and 2.1% by weight are considered as steel. The microstructure configuration of solid steel is defined by the phases present in the steel microstructure. A defined layout of iron and carbon in steel is recognized as a specific phase in steel. Steel microstructure may be formed by more than one phase depending on its grade and previous heat treatment. Type, fraction and number of each phase present in a steel microstructure as well as the position of these phases with respect to each other, mainly define the properties of the steel.

Iron carbon phase metallurgy is an arrangement of iron and carbon atoms respect to each other, which, like the physical definition of a phase, have the same crystallographic structure, density, index of refraction and/or other uniform chemical composition, and physical properties. It is known that we can produce various desired microstructures such as bainite, martensite, cementite (iron carbide, Fe_3C), ferrite (α-iron) , pearlite (ferrite, cementite), ferritic-pearlitic, austenite and some other microstructures or different percentages combination of them by controlling cooling rate of hot steel from the austenite temperature.

Much work has been done to produce a specific microstructure of steel using suitable cooling techniques. Many different heat treatment techniques and processes are deployed to achieve a microstructure with defined characteristics such as, spheroidizing, full annealing, process annealing, normalizing, quenching, martempering (mar quenching), quench and tempering and austempering, flame hardening, induction hardening, carburizing (e.g. pack carburizing, liquid carburizing, gas carburization ,…).

2.1.2 Classification of steel

The subject of steel grade is related to the classification of steel. Many metallurgists raised the issues of classification and quantifying the microstructure of steel ([1]-[5]). Thousands of different steels in today's steel industry can be classified in many different classification systems.

The main factor in steel classification is by its carbon content because of its effect in final cost of the steel. However, several other elements, such as manganese, phosphorus, sulfur, silicon, nickel, chromium, molybdenum, copper, cobalt, tungsten, and vanadium may be added to steel to obtain certain desired properties but the additional elements to the steel is not limited to these. These elements mainly increase solid solution strength, hardness, hardenability, although some elements have more specific duties in the steel such as high level of manganese for enhancing wear and abrasive resistance and adding sulfur to improve the machinability, and some elements like oxygen are undesirable elements in the microstructure of steels.

There are number of different national classification systems in different countries. Major classifications in the US are AISI, SAE or AISI/SAE, ASTM and ASME. The well-defined classifications are based on different factors in steel including composition, microstructure, application, specification, commercial name or chemical composition, mechanical properties,

and corrosion or heat resistance and formability. ASM Handbook Volume 1, gives the details of all major classifications.

In this project, a series of experiments are conducted to investigate the cooling rate of AISI designation grades of 1010*, 1091* and 1319*. In this classification, the last two digits are (in case of steel with C %> 1.3 digits) stand for the carbon content in the texture of each grade of steel and the first specifies other alloying elements in the steel. Table 1 shows the designation standard given by AISI for steels used in this project.

Table 1 AISI designation system for the steels used in the experiments.

AISI Designation	Type of Steel
10xx	Plain Carbon (Mn 1.00% max)
13xx	Mn 1.75%

2.1.3 Cleanliness of steel

Anomaly is abnormality, which is defined literally as deviation from normal or regular arrangement, general rule or known method [6]. In this dissertation, anomaly is a general term referring to desirable inclusions, and all type of defects including non-desirable inclusions, voids and cracks present in the iron-carbon texture. In fact, steel is an iron-carbon structure with other elements located interstitially in its crystal structure. Nevertheless, inclusions and other anomalies, such as, voids and cracks are almost inevitable in its microstructure. The additive elements to steel mainly control the material properties such as tensile strength, formability, toughness, weldability, resistance to stress cracking and corrosion behavior. These properties for steel are defined by every special caster application. A portion of the essential and incidental

elements react chemically with each other and form non-metallic inclusions like manganese sulfide, aluminum oxide or titanium nitride which may or may not be desirable, depending on application of the steel, but they are major sources of additional microcracks in the steel during heat treatment or machining. It is evident that nonmetallic inclusions are less in continuous cast stainless steel than in ingot cast stainless slabs [7]. Non-metallic inclusions in steel produced by continuous casting can be classified according to their sources and formation process into different categories and subcategories as follow, [8];

1. Indigenous inclusions
    a. Deoxidation products
    b. Precipitated inclusions from cooling and solidification of the steel
2. Exogenous inclusions from
    a. Re-oxidation
    b. Slag entrainment
    c. Erosion/corrosion lining refractory
    d. Chemical reaction;

Indigenous inclusions are formed during cooling and solidification of steel and their types depend on the type of deoxidation [8]. Exogenous inclusions are formed because of incidental chemical and mechanical interaction of liquid steel with its surroundings. During solidification of steel, in addition to inclusion formation, voids, cracks and microcracks are also created [8]. However, they may be generated later because of the cooling process of the as-cast slab. All these anomalies in the steel are studied under the title of '*Cleanliness or Soundness of steel*'. The concept of cleanliness of steel deals with the study of controlling the composition of nonmetallic inclusions and size and distribution of the anomalies. The requirement of High quality steel

forces steel industries to pay special attention to cleanliness of steel products. This is because some inclusions affect the machinability of the steel. Other decrease the fracture toughness and others, such as oxides or sulfides, increase the ductility behavior [8]. Hard and brittle oxides, particularly large alumina inclusions, cause fatigue problem in bearing steel [9]. Clean steels are known to have high Charpy shelf energy, high tensile ductility and very good formability [10].

Cleanliness of steel is related to a low content of non-metallic inclusions, mainly oxide and sulfide inclusions, as well as other anomalies [11]. Inclusions due to the nature of the ore and steel making procedure are also present in the steel. Therefore, clean steel is mainly characterized by an inclusion specification. A large body of literature has been published concerning cleanliness of steel ([12]-[16]). Kiessling [12] studied clean steel methods for trace and control of ingot inclusions. McPherason and McLean [13] gave a good description of inclusion types, distribution and tracking methods in the continuous casting process. Zhang and Thomas [14] offered suggestions to improve the techniques for steel cleanliness at the ladle, tundish and continuous caster.

The concept of clean steel in continuous casting is bounded between two criteria. These criteria are physical amenability to casting and maintaining ladle treatment composition. The first criterion includes elimination of blowholes in the strand, decreasing the exogenous non-metallic inclusions and creating optimum conditions that lead to separation of suspended deoxidation products. The second criterion refers to treatment for carbon, nitrogen, hydrogen, sulfur and especially oxygen [17]. Higher temperature and Cr density, increases the solubility of oxygen in steel and decreases the cleanliness of the steel product [7]. To do this reduction or elimination, the activity of primary steelmaking slag with high oxygen is used to avoid

rephosphorate. Superheating is one way to improve the cleanliness of steel by lowering the amount of inclusions in the slab [17].

Another way to enhance the cleanliness of steel is to move the inclusions to the surface and collect them. Researchers [18] were able to compute, numerically, the rising velocity of inclusions in molten steel. They verified experimentally the behavior of moving inclusions in the slab continuous casting mould by implementing solution for turbulent flow of molten and inclusion trajectory and show the movement of inclusion has relationship to inclusion diameter.

However, research work defines the conditions to produce clean steel for many different steel compositions. This ideal condition cannot be obtained because of extra processing cost and its contradiction with customer demands for quality. Another reason for deviation from the ideal clean steel is to keep the casting process continuous at the cost of lower grade products [17].

In some applications such as longitudinally welded and electric resistance welded pipes, high internal cleanliness is important [17]. Different destructive and non-destructive tests have been designed to define the level of cleanliness of the steel. In this research work, ultrasonic NDT is used to detect the cleanliness in the steel. In very clean steel, fatigue damage is related to the square root of the area of the inclusion. Consequently, the size of the inclusion is more important than its shape and composition ([19]-[21]). Different theoretical methods such as Statistics of Extreme Values (SEV) ([22]-[25]) and Generalized Pareto Distribution (GPD) [26] have been developed to determine the size of maximum the inclusion in large volume steel. A classification for the inclusions observed in the ultrasonic NDT test images are defined by the author on the basis of the size of the inclusions present in the slabs of three grades of steels tested in this dissertation.

2.2 SOLIDIFICATION PROCESS IN CONTINUOUS CASTING OF STEEL

The steel used in the experiments of this project were produced by the continuous casting method. Although the purpose of this dissertation is neither the study of steel manufacturing processes nor the formation of microstructure of steel during solidification, it is useful to have a short walk through in the continuous casting steel slab manufacturing process to understand how control of cooling the solidified slab can modify the microstructure of the slab to produce better quality steel. Studying the processes of continuous casting steel provides the knowledge of the phenomena involved in the formation of the cast slab microstructure and anomalies.

Solidification is a major source of creation of anomalies in the bulk material. In addition, residual and local stresses around anomalies or in the vicinity of grain boundaries are the source of microcrack or crack propagation during heat treatment and cooling of solidified hot steel. Crack propagation can also be prevented by anomalies formed and distributed during solidification. They provide evidence of the relation of solidification for the behavior of rate and method of cooling of as-cast hot slab and later operations such as heat treatment and machining. Consequently, it is essential to review the solidification process in continuous casting steel production within the scope of this dissertation.

The continuous casting method has many advantages such as increase in yield, better surface condition and internal quality of production, more uniform product, higher manpower productivity, easier integration into metal production systems and reducing metal production cost by saving time, energy, and capital. This is due to eliminating extra steps, such as ingot teeming, stripping, and transfers; soaking pits; and primary rolling ([27],[28]). George Seller got a patent on continuous casting of metal for producing pipe in 1840 [29]. Henry Bessemer patented process for the manufacturing of continuous sheets of iron and steel in 1946 [30]. Thereafter,

many inventions and modifications helped continuous casting process technology to grow to become the primary technique in producing ferrous and non-ferrous metals. The first vertical type large slab machine with bending of the strand to horizontal discharge was launched in 1961 [30]. Detailed historical aspects of continuous casting can be found in many papers ([31], [32]). Today, annually 750 million tons of steel in the steelmaking operation, 20 million tons of aluminum and many tons of other alloys are directly cast from molten metal.

In this process, a ladle filled with hot metal is rotated from the electric or basic oxygen furnace to a cast machine on top of the rectangular or delta and "T" shapes bath called a tundish. Molten metal is delivered from the ladle to the tundish after ladle treatment like alloying or degassing via a refractory shroud. Inserting argon gas causes a fully turbulent transient fluid motion in the tundish [28]. The main function of the tundish is to create a continuous, steady, and stable flow of liquid steel into the mold during draining of the ladle. The mold is tapered to compensate for metal shrinkage on solidification. It provides better heat transfer and, more importantly, fewer cracks.

Sigfried Junghans introduced the oscillating mold system to the continuous casting [31]. Lubrication and oscillation of the mold decrease the friction to avoid sticking of the solidifying steel, shell tearing, and liquid steel breakouts [33]. Researchers found that the length of stroke and frequency of oscillation affect the quality of the steel and should be specified depending on the type of the steel [34]. The lubricant is the powder added to the molten metal [32]. Sintering and melting of mold powder added to the top of the steel surface protects the liquid flux layer. The powder flows over the liquid steel due to its low melting point and creates a lubricant between the shell and mold. This enhances the cleanliness of the steel by trapping the inclusions and other impurities and protects the metal from re-oxidation [28]. To emphasize the effect of the

mold in steel cleanliness, McPherson used the term “Mold Metallurgy” [35]. However, it has other functions like increasing oxide inclusion separation. The mold provides a solid shell with sufficient strength extended up to the entry of the secondary spray cooling zone (Figure 3).

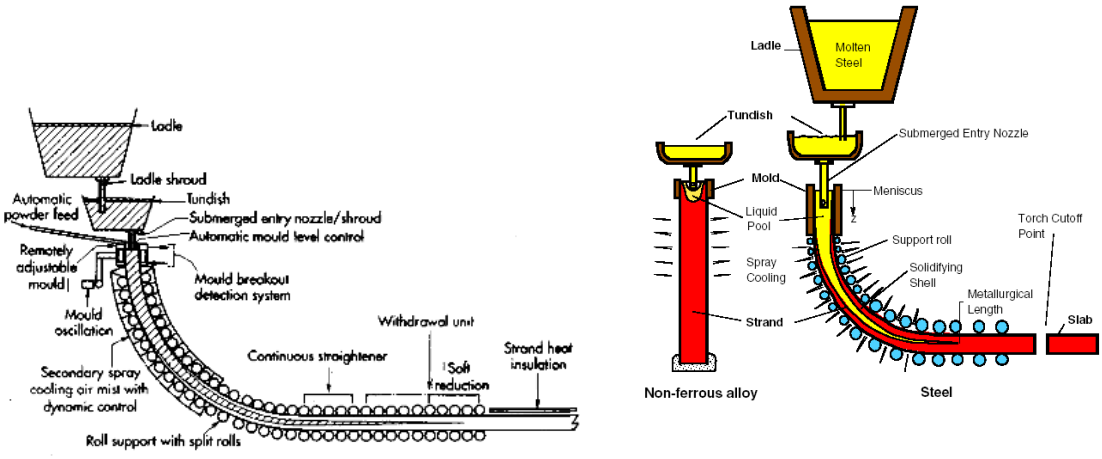

Figure 3 Process of continuous cast steel ([23], [33])

Radioactive experiments and practical observations show that below the meniscus the molten metal starts lose its superheat and forms the initial shell [36]. Various hypotheses were published to describe the mechanism of first shell formation ([36], [37]). Controlling the reciprocation process and heal time by the casting speed put the skin under compression. This causes the confrontation between the pressure of the inner still liquid metal and contraction of the mold near the skin, which gives an odd shape to the solidification profile other than a simple square shape [38]. The nozzle clogging can create fluctuation level in the mold and can be reduced by improving the cleanliness of the steel and the Ca treatment at the ladle furnace [39]

A number of experiments and theoretical models have been used to study steel solidification from the moment it leaves the tundish to the time it is quenched after it has cooled in the mold ([40]-[57]). Other researchers target other areas in the steel making processes to lower the final cost of the steel. All these procedures are very complex and precise and a miscalculation can damage the machines or stop production, which increases cost. Cracks and other anomalies are created during the solidification process. Dissipation of superheat and temperature at the meniscus entrap the inclusion and gas bubbles, and turbulent flow and liquid-

liquid and liquid-solid phases' interactions. Furthermore, thermal and solute buoyancies effect of surface tension take place during solidification of steel [28].

There are different types of casters. Steel production in the vertical bending (VB-type) caster contains a lower amount of inclusions distributed deeper compared to the curved caster (S-type) [58]. The driven force to move the strand forward is provided mainly by the rollers. However, gravity has an effect on the speed of the strand in vertical casting. Applied forces during the solidification process affect the quality and soundness of steel. Some of these forces are external and residual stress generation, tension, oscillation and gravity-induced waves, residual distortion and wear along the mold, microscopic and macroscopic coupled segregation. Figure 4 illustrates other factors and phenomena that occur during solidification inside the mold, which determines the microstructure of steel.

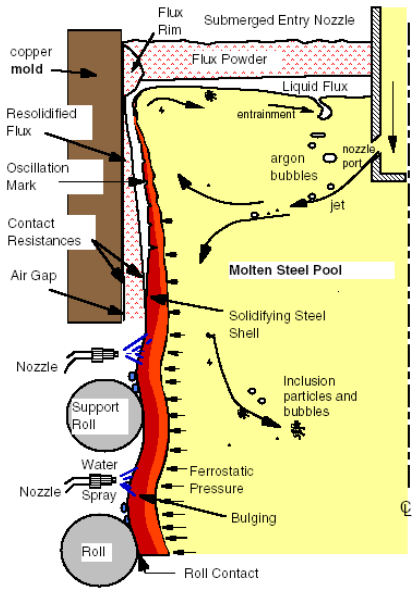

Figure 4 phenomena during solidification upon to secondary cooling stage [28]

Figure 5 Strand unbending by straightener withdrawal units during secondary cooling zone of continuous casting process of steel [59]

Proper progress in changes of the arc radius in bending and straightening process of VB-type continuous casting is important to minimize the occurrence of the crack and increasing the quality of the product. Implementation of the multi point unbending process can be seen in Figure 5 in which the radii gradually become into the horizontal plane as the strand passing the secondary cooling zone [59]. Secondary cooling is started after the steel leaves the mold (Figure 6).

Figure 6: Secondary cooling stage in continuous casting steel.

At secondary cooling molten steel is encapsulated by a solidified skin and water spray causes the release of superheat from the inner section of the steel. However, poor thermal

conductivity of steel limits the effectiveness of spray cooling and, in return, results in reheating the surface [38]. The quality of the secondary cooling process was the subject of many investigations ([60]-[62]). Higher cooling rate increases exogenous inclusions by increasing the possibility of entrapment [8]. Different methods such as dynamic control of continuous casters and dynamic spray cooling model are used to control the temperature of the strand in continuous casting. Thermal tracking of the slab cooling history is accomplished by dynamic control of continuous casters suggested in the literature [63]. Dynamic spray cooling includes techniques such as control points along the caster length [64], through slab slices [65], combined feedback with feed-forward [66]and curve fitting [67].

During the secondary stage, liquid steel is solidified to semis. Three important factors determine the type of the microstructure develops during the solidification of a casting. These factors are;

- The temperature gradient in the liquid ahead of the liquid–solid interface (G);
- The velocity of the liquid–solid interface (V)
- The alloy composition (C_0).

Depending on the G/V ratio, the microstructure is planar at first to cellular and then to dendritic, as G/V gets smaller. Hence, usually three zones in the macrostructure of a continuously cast steel semi can be recognized. These zones from the surface towards the centre, as it can be seen in Figure 7, are chilled crystal zone, columnar zone and equiaxed zone, respectively [68].

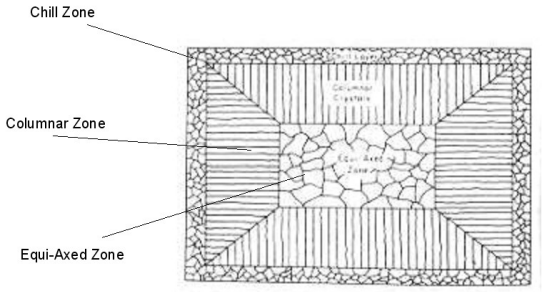

Figure 7 Three zones in microstructure in semis

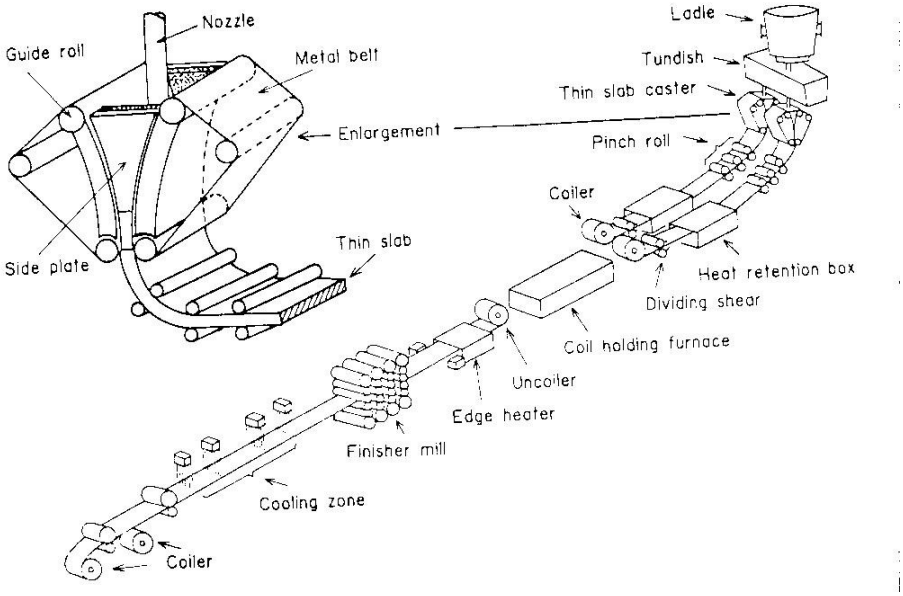

Figure 8 Schematic diagram of a Kawasaki steel twin belt caster.

Increasing application of continuous cast steel is essential to the rapid return on investment, especially because of large flow from large capacity blast furnace, makes research on increasing productivity very attractive to steelmaking companies. Different techniques were suggested to improve the productivity of ready to deliver process for slab, billet and bloom steel. These techniques include increasing the average sequence length, increasing the casting speed, increasing the averages section size cast, improving equipment utilization, ladle returns, decreasing maintenance time and increasing the strand width [17].

There are a number of other methods such as compression casting, which increases the productivity. However, all of these techniques may have a negative impact on the life of equipment used in the process, product final cost or desirable properties of the steel. An example of this aspect can be offline slitting of the wide slab or increasing the width of the strand. This method is an effective way to get higher productivity but slitting is a cold work process and not suitable for hot charging. It also needs good internal soundness of the slab. Temperature loss is a consequence of implementation with hot charges. Therefore this method is replaced with another method called twin casting [17]. A typical schematic diagram of twin casting is shown in Figure 8. Nevertheless, a disadvantage of this method is that large surface exposure of the billet to the air increases the oxidation on surfaces during solidification.

Solidification of the slab is completed over the formation of triple point and centerline within the slab. The next step of the continuous casting process after completion of the solidification of the strand of the steel is to cut with a torch, shear of solidified continuous cast strand of steel into desired lengths of slabs, bloom, or billet. However, the cooling process of the slab may continue until its temperature is lowered enough prior to cutting. There is extensive research concerning the cooling of the hot charges under the meniscus up to completion of solidification in the secondary stage to find the critical cooling rate, which provides a certain degree of cleanliness. The solid phase through the entire thickness of the strand introduces new thermal properties to it.

2.3 PREVIOUS RESEARCH WORK

This section provides a review on previous research work on the topics related to this research work to understand the extensive work done on the topics related to this research work. These literature reviews are partly with focus on the research studies on soundness and other anomalies generated during solidification whose effects determine the critical cooling rate of hot solidified strands of steel. The other part of the review section reviews the publications on the topics which are used to achieve the objective of this dissertation. Hence, the following sections presents literature review in studies on the microstructure defects and the source of the defects, monitoring of microstructure by the NDT method, effect of inclusion, on the microstructure, experimental study on cooling rate and numeral simulation and modeling methods on the study of phase transformation.

2.3.1 Previous studies on the microstructure of steel

Research on the effect of steel microstructure and anomalies on mechanical properties of steel and its machinability, have become increasingly attractive to many researchers since the middle of the 20th century. Work on steel was started with Iron Age using the trial and error method. Progress in optical physics and modern optical electrical as well as electromechanical tools and devices provided precise observation and measurement on a micro and nano scale. Invention of computers and super computers along with progress in software engineering gave researchers the opportunity to understand the microstructure of steel and the effect of anomalies in machining using computational and numerical methods in analytical and simulation results. Developing new chemical compounds and investing in producing new etching agents helped researchers to obtain

information about the microstructure of the steel. Results from experimental tests, analytical computation and numerical simulation assist promotion of both quality and quantity of steel manufactured around the world and lowered the cost of the steel making process. These researchers have mainly focused first on how the microstructure of steel is formed during solidification and second, how the microstructure affects the properties of the steel especially the mechanical and machinability properties. Work on classifying steel was published in a number of journals ([4],[5],[69]-[71]). These results helped to identify the microstructure of steel at each stage of the steelmaking process as well as final products of steel.

Customer defined properties for steel products called upon the metallurgists for new challenges in adding different additive elements and components to steel in order to modify material properties. Many publications discussed the relationship between mechanical and machining properties of steel and additive elements in steel microstructure. Additive elements to molten steel during continuous casting may introduce inclusions to the microstructure of the strand, which affect the amount of anomalies during cooling after completion of solidification. Factors such as inadequate thickness of mould powder slag, large fluctuations in mold level and clogging of the submerged nozzle may cause the formation of the inclusions. The technical process reasons for increasing density of the inclusion in the steel matrix are low bath level in the tundish, poor mold and tundish level control and insufficient pouring tube depth [17].

Reoxidation of steel is the main source of the oxide inclusions [17]. Pontius [72] studied the aluminum oxide formation during solidification. Many published papers have shown that inclusions have their own impact on material properties of steel. Studies on MnS inclusions have shown that they are responsible for chip fracture during machining by initiating cracks as a result of increasing stress in the machining shear zone ([73]-[75]). Manganese sulfide also improves

machinability by decreasing tool wear by lowering tool chip friction and, consequently, cutting temperature and cutting force [76]. However, other researchers said that the presence of oxygen causes sulfur to improve machinability ([77], [78]). Others have shown that the manganese selenide phase remains larger and more globular in the final hot rolled product [79]. Tellurides and selenides lower the quality of the sliding surfaces by resistance on seizing [80] while lead decreases shear resistance ([80] -[82]). Taylor emphasizes that the uniform quality working material as the most important factor among other factors playing a role in the machinability of the steel. He explained the advantages of high sulfur steels on machinability [83] However, some research work shows these additive elements may also degrade steel quality. Sulfur content can increase the extent of cracking at high temperature [84]. The susceptibility of steel to overheating depends on alloying and micro-additions [85].

Segregation of sulfur and phosphorous from the liquid film at grain boundaries into the interdendritic region creates a low ductility and strength region and, consequently, forms cracks in the microstructure of steel between the solidus and 2420 degrees Fahrenheit ([86][87]-[89]). The ratio of precipitation of MnS in the matrix and precipitation of AlN along grain boundaries generates cracks in steel during solidification by forming different low ductility regions at different temperature ranges ([90],[91]). Vanadium and niobium precipitation by cyclic heating and cooling in secondary cooling zone also causes embrittlement of the steel [92].

In addition to inclusions, many other defects can also be introduced into the microstructure of steel. Formation voids and cracks are inevitable during solidification and may increase in the cooling process of hot solid steel slabs to room temperature or any future heat treatment and machining of the steel. Voids and cracks have irregular shapes compared to hard inclusions. Different type of defects such as surface and internal cracks, bulging, pinholes,

inclusions, central unsoundness defects caused by mold oscillation and lubrication process have been seen in blooms and slabs [72].

Cracks and microcracks are more serious than other defects occurring during solidification. Brimacombe and Sorimachi have classified the origin of cracks systematically [93]. Internal and external forces higher than ductility to fracture stress concentration of the steel, generate cracks [94]. Internal stresses during surface reheating create cracks because of zero ductility of steel at solidification temperature [95]. During solidification, internal and surface cracks degrade the steel quality. Surface cracks may be caused by uneven heating, which introduces transverse and longitudinal facial cracks [96]. Figure 9 presents an example of transverse cracks on a steel slab produced by continuous casting.

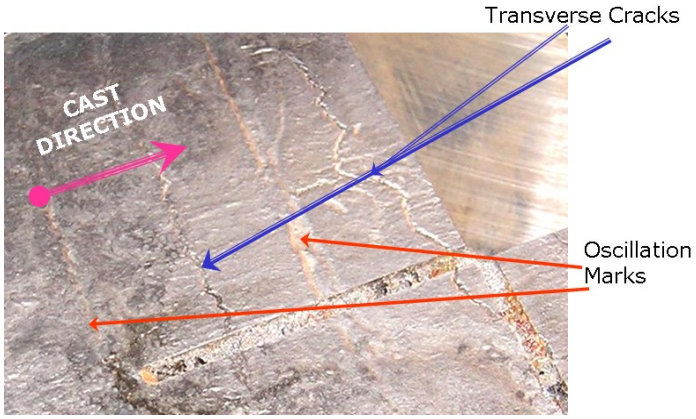

Figure 9 An example of transverse cracks formed during solidification of continues casting steel process.

Journal of longitudinal cracks are sensitive to certain chemical composition, insufficient narrow face taper, non-uniform mold powder slag level and poor mold level control. Longitudinal cracks can be formed from stress at the meniscus during solidification by high mold wear and poor mold surface as well as insufficient strand support below the mold, including caster or mold misalignment and thermal stresses due to non-uniform cooling [17]. Transverse cracks in steel may be generated by too large mold taper, poor oscillation conditions, a low

surface temperature at straightening and abrupt cast speed changes. Three main in line sources have been reported for transverse cracking in Mittal plants [34]: (1) falling the strand surface into ductile behavior range and straightening strains (2) intrinsic hot tearing in the mold because of thermal contraction (3) external hot tearing at or near the mold because of applied external stresses. Figure 10 shows how these transverse cracks can extend to more severe cracks during hot rolling.

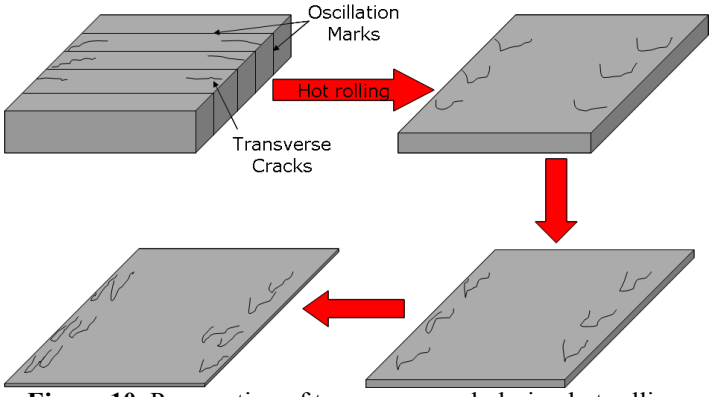

Figure 10 Propagation of transverse crack during hot rolling.

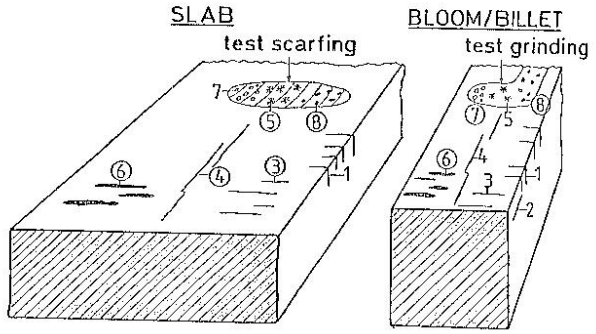

Figure 11 Surface cracks on a continuous cast steel slab: (1) Transverse corner cracks (2)Longitudinal corner cracks (3)Transverse cracks (4)Longitudinal cracks (5)Star cracks (6)Deep oscillation marks (7)Pinholes (8)Macro inclusions.

High content of foreign elements, such as aluminum, niobium, vanadium or copper, form crazing cracks due to local shortness of the steel [92]. Uneven cooling of the surface also causes

local type star cracks [17]. Figure 11 illustrates different types of defects on a continuous cast steel slab.

Internal cracks formed during solidification can be classified into five groups of halfway and midway cracks, start or centerline cracks, diagonal cracks, bending cracks and pinch roll cracks. The work of Morozenskii et al. [97], shows that near solidification elongation to rupture in steel with carbon content of 0.17 to 0.2% is minimum. Halfway and midway cracks appear to be formed mainly because of excessive secondary cooling and creation of sudden changes in temperature ([98]-[103]). This sudden change can be caused by an unbalanced rate between radiation and convection cooling along secondary cooling zones or different boundary conditions such as below the mold where the hot surface is cooled suddenly by water spray. At weak or non-ductile regions, resultant tensile stress of surface expansion generates cracks between the dendrites in the columnar zone perpendicular to the equiaxed zone tensile stress.

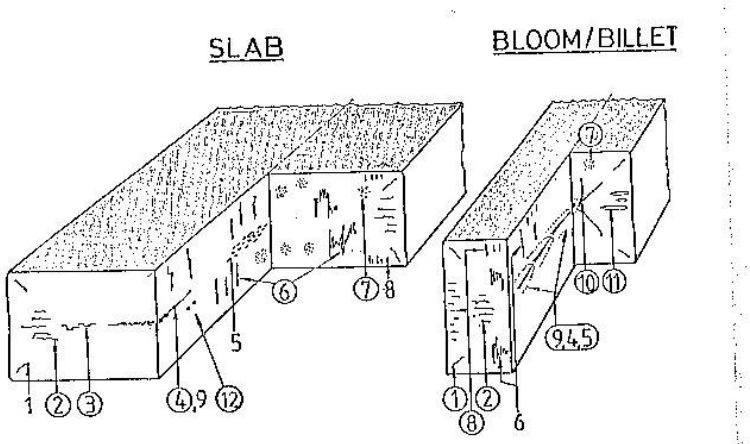

Figure 12 Internal defects in continuous cast steel slab: (1)Internal corner cracks (2)Side halfway cracks (3)Centerline cracks (4)Centerline segregation (5)Porosity (6)Halfway cracks (7)Non metallic inclusion clusters (8)Sub surface ghost lines (9)Shrinkage cavity (10)Star cracks diagonal cracks (11)Pinholes (12)Semi macro-segregation.

Likewise, centerline cracking is due to tensile stresses raised by abrupt change in temperature of the centerline with completion of solidification [98] because of bad machine

conditions at the final solidification area or too low secondary water-cooling [17]. Too high or too low cooling of slab's side surfaces as well as bad equipment conditions can introduce triple point cracks in the slab [17]. Figure 12 is a schematic view of different internal defects on the continuous cast steel slab. Tensile stress raised by a high, different, temperature at surfaces making an obtuse corner creates diagonal cracks at right angle to the strain ([104],[105]). Straightening or bending operations when centre steel is above 1327 °C, forms straightening or bending cracks in the non-ductile region [98]. For the same reason as straightening or bending cracks, high roll pressure at any point of the strand during solidification can generate pinch roll cracks [96].

Researchers have shown that solidification parameters play a role in characterizations of anomalies. Casting speed or tundish temperature controls axial porosity of the steel. The size of the hole in the middle section of the ingot increases with larger amounts of water during secondary cooling [106]. Also in low casting speed, gravity accumulates the inclusions unevenly due to floating of inclusions [107]. Uneven non-metallic inclusion distribution in dendrites and cluster arrangement makes the microstructure dangerous to fracture by decreasing the energy absorbed in the microstructure [85]. Billet dimensions control the effect of corner radius on longitudinal cracks such that more cracks are formed in larger billets [108]. Experiments on tundish temperature show that after a critical temperature, the length of cracks increases as the temperature of the tundish increases ([84], [109]). Different phase transformations during cooling of hot solidified steel can introduce cracks in the microstructure of steel.

2.3.2 Previous work on detecting the defects

The concept of cleanliness and soundness is relevant to the characterization of anomalies. Because of the significance of the presence of anomalies in increasing the defect density in the macrostructure during cooling of the slab, it is important to have an economically feasible and analytically reliable method to detect and recognize the anomalies.

Internal defects in continuously cast slabs can have a strong effect both on the performance of the steel during thermo-mechanical processing and/or the mechanical properties of the final product. Therefore, attempts to find a suitable method to identify, quantify and characterize the defects have been the subject of many studies. The characterization might include the density, distribution, type and location of the anomalies. Several methods exist for detecting the presence of non-metallic inclusions both off-line and online during the steel making process ([110]-[117]). Experimental workers identify non-metallic inclusions by metallographic, chemical and petrographic methods [118]. Zhang and Thomas ([8], [14]) discussed more than 30 methods for detecting the anomalies under two main categories of direct and indirect methods. However, the direct technique measurements are accurate but they are costly compared to indirect ones [8]. On the other hand, the indirect measurements are reliable only to a certain extent and they need more research work to increase their reliability. The evaluation of cleanliness for formability, deep-drawing and/or bending properties of the final sheet product, or fatigue life of test specimens or product samples is, basically, by destructive mechanical tests.

The characterization of defects using destructive tests (DT), i.e. microstructural analysis, is tedious, time consuming and not cost-effective. The use of NDT such as X-ray analysis and ultrasonic signals are practical and economical methods for examining bulk material in different applications. Samples that are examined by NDT can go directly to their next application and no

special changes must be made to a normal production line. There are multiple types of NDTs including ultrasound and x-ray techniques. Debiesme [119] explained the Hydrogen Induced Crack test and Magnetoscopy for sheet tests. Persson et al. [120], detected the strains with a resolution of about 25×10^{-6} using a non-contact laser speckle technique, in a thermal fatigue test performed by cyclic induction heating and internal cooling test rods. Ekerot [121] used X-rays to detect inclusions and the crystalline phases. Ultrasonics is a tool in detecting and measuring different microstructural characterization such as monitoring in real time changes of industrial process material like recrystallization [122]. Conventional Ultra Scanning (CUS) was explained in many papers ([123]-[124][126]). Shtreme [85], used ultrasonic defectoscopy which revealed particles greater than 2 mm to investigate the problem of nonmetallic inclusions in the microstructure. Exogenous inclusions in steel can also be detected by Ultrasonic Scanning, microscopic observation, sulfur prints, slime (electrolysis), X-ray, SEM, slag composition analysis and refractory observation [8]. Furuya et al. [127], described the ultrasonic fatigue test technique for detecting the inclusions. More background about NDT and its applications can be found in many websites, books, and literature ([128]-[129][130]).

However, NDT methods are usually less accurate than DT techniques and they require advanced instruments, precise calibration, detailed response processing and reliable results of analysis to obtain useful information in an acceptable precision range for a given application.

2.3.3 Previous studies on the inclusions

A large body of literature elaborated the interaction of the inclusion in the microstructure with the steel matrix and the effect of the inclusion on the material properties of the steel and, consequently, in the generation of the residual stresses within the microstructure due to internal

and external forces. An investigation of previous research on the effect of inclusions on steel properties describes the role of the inclusion, in the formation or intensification of stress concentration zones.

2.3.3.1 Studies on the effect of inclusions on material properties of the steel

The relationship between non-metallic inclusions and the mechanical properties of the steel product has been discussed in the literature. The effect of non-metallic inclusions on grains influences all processes of fracture, indirectly [85]. Maropoulos and Ridley [135] used electron microscopy and X-ray diffraction to study the microstructures and to relate the microstructural characteristics to the mechanical properties. They stated that the amount and size distribution of MnS inclusions directly affect Charpy upper shelf energy and ductility. Results from the literature show that inclusion distribution affects Charpy upper shelf energy ([136][137] -[139]) directly by the following factors, ([140]-[144]),

- Sulfur level/ inclusion volume fraction
- Non-metallic inclusion number per unit area
- Inclusion shape
- Inclusion size and spacing

Thornton [145] reviewed, extensively, the influence of inclusion parameters, shape, size, quantity, interspacing, distribution, orientation, interfacial strength, and physical properties relative to the matrix, on mechanical parameters such as tensile strength, impact strength, reduction of area, fatigue properties and fracture toughness. Some of these effects determine the function of specific steel products. For example, microstructure studies on rail steel gave some information about the effect of non-metallic inclusion characterization (volume fracture, yield

strength,…) on mechanical properties of material such as tensile, fatigue and fracture toughness. These investigations revealed that tensile properties are independent of inclusion type and volume fraction level present in rail steel while toughness and high cycle fatigue properties are related to inclusion specifications [146] However, toughness of a specific grade of steel can be improved economically by specifying the upper limits of the size, quantity and elongation of inclusions and required toughness, and machinability operating conditions [85]. Studies on high strength steels show that hard and brittle oxide inclusions are the main factors accounting for initiation of fatigue damage [147],[148]). Baker and Charles [149] reported the effect of deformation of inclusions on the fracture properties of steel.

Therefore, scientists introduced different techniques to manipulate the inclusions in order to increase the quality of the steel products. Metallurgists suggest techniques like primarily, melting, oxidation, casting and re-melting procedures to control the quantity, nature, size, shape and distribution of inclusions [85].

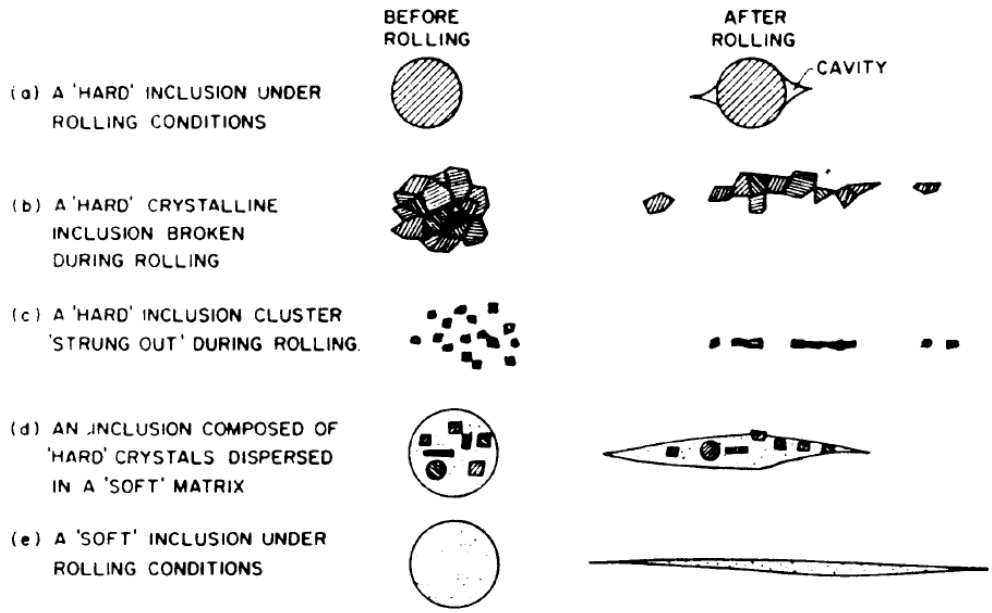

Figure 13: Classification of inclusions based on their behavior in response to applied stresses.

The influences of the non-metallic inclusions on mechanical properties are via their reaction to stress fields introduced to the matrix. Stress concentration around nonmetallic inclusions changes the mechanical properties of steels [150]. Literature on stress concentration close to nonmetallic inclusions ([151]-[153]) and other experimental work ([154], [155]) indicate the effect of the presence of inclusions on stress distribution in the steel matrix around the inclusions. Experimental work on major types of non-metallic inclusions in steel such as oxide inclusion, silicates, sulfides, carbides and Al_2O_3 shows the distribution of stress around the inclusions [156].

These stresses change the shape of the inclusions by applying uneven forces on its contact surfaces with the matrix. Elongation of inclusions degrades the fracture properties [149]. This can be observed especially if the direction of elongation is perpendicular to the principal stresses ([157]-[160]). Other papers in the literature ([161]-[163]), have investigated a number of factors which play roles in the response of inclusions to stresses such as, difference between strength in inclusion and matrix, composition of inclusion and matrix, contact surfaces between inclusion and matrix, temperature at imposed stresses, strain and strain rate of stress configuration, particle size, stress state and state of second phase particles. Based on these factors, different classifications for the inclusions have been considered. Hilty and Kay [164] have seen five different classes of inclusions found in the experiments on the basis of their behavior to the applied stresses on the matrix (Figure 13).

The hardness of the inclusion is temperature dependent. Waudby [162] stated that deformation of steel and its mechanical behavior in both hot and cold working is influenced by the behavior of inclusions. In hot working, this behavior is influenced by several factors including temperature, mainly by plasticity of the inclusion, the relative plasticity of the various

phases within the inclusion, relative plasticity of the inclusion with matrix and friction force at the contact surface between the inclusion and matrix. At low temperature, the inclusion may become a potential source for defects in the final products. He showed that the initial shape of the silicate inclusions at low temperature has an effect on its fracture during hot working and small fragments are chipped off and spread out along the direction of flow of the material. He considered four factors, in addition to temperature, for governing the plasticity of silicates. These factors are;

a) Reduction during hot working

b) Particle Size

c) Composition

d) Second phase particles

Behavior of the silicate during hot working was explained previously in many articles ([73], [162], [165]-[167]). Ekerot [121] found the transition temperature for hard glassy silicate inclusions at which the deformation behavior of the glassy silicate changes and they become very soft and their index of deformability may even reach higher than 2. This transition temperature may be changed depending on the SiO2 content. He also stated that calcium stabilizes the glassy inclusion phase so the deformability of the inclusions can be improved. However, crystalline inclusions such as SiO_2-MnO-Al_2O_3-CaO do not have this transition temperature and remained undeformed at all hot working temperatures.

Klevebring [167] predicted the deformation behavior of an inclusion using the hot hardness data for manganese selenide and manganese telluride inclusions. He proposed that oxygen increases the hardness of MnS and consequently decreases the deformation index of

sulfides. This effect of oxygen content provides a deviation for the modeling of MnS deformation.

Researchers have attempted to predict the behavior of inclusions in the stress fields using continuum bifurcation analysis on a modified Gurson-type constitutive relation for porous media to predict changes of ductility behavior in low carbon steel containing stringered manganese sulfide inclusions [168]. Ekerot [121] approximated the stress-strain relationship of the glassy inclusions by Newtonian flow. Sundstrom [169] used a power law stress-strain relationship in his plane strain model of elliptical inclusions in an infinite plate. He modeled a very soft inclusion behavior by assuming the same strain hardening exponents for the inclusions and the matrix. Zeisloft and Hosford [170] neglected inhomogeneity of the inclusion in the deformation of the specimen the for compressive plane strain of inclusions. Such an approach was found to result in too high a deformation index.

2.3.3.2 Previous studies on the inclusion deformation

Study of the mechanism of deformation and factors involved in determining the deformability of different types of the inclusions have been the subject of much research work. These studies showed that the flow of solidified steel matrix over inclusions is due to either exerted force or because of internal forces such as gravity. This flow of material caused deformation of the inclusion because of friction between matrix and inclusion at the interface of matrix with the inclusion [163]. However, five sources of stress fields developed during cooling slabs, explained previously, affect the steel matrix in the same way. Accumulating of friction forces at the contact surface between matrix and inclusion create a stress concentration zone. This zone is believed to be responsible for changing the shape of the inclusion [171]. Kiessling and Lange [172] believed the main factor in the inclusion deformation is yield stress difference between inclusion phases

and steel matrix. The extent of deformation of the non-metallic inclusion constitutes some volume of the metal deformation [85].A portion of metal deformation is governed by the extension of non-metallic inclusions deformation.

From the deformation point of view, inclusions can be classified to fall into two general groups: of soft and hard [8]. For either type, characteristics of the stress field around the inclusion are generated by distribution, concentration and rate of change of the stress field. Some of the main effective factors in inclusion deformation ([162],[166],[171],[173]), include morphology, strength of inclusion and matrix, composition, inclusion-matrix interface, temperature, strain and strain rate, particle size, stress state, second phase particles and frictional forces at interfaces. Deformation of inclusions slows down as flow is constrained around the inclusion [161]. Higher deformation of MnS inclusions lowers the deformability of the MnS inclusions [171]. Work on silicates gave a qualitative description of their deformation behavior [174], [175]).

Malkiewicz and Rudnik [118] showed that higher deformation of steel decreases the plasticity of the inclusions. They also confirmed that plasticity of inclusions with low deformability, iron-silicates, is size dependent. The results of their experiments also show that deformability of an inclusion is a function of chemical composition and deformation temperature. Inclusions with low melting points, e.g. iron-manganese silicates, have greater deformations than aluminum silicates with high melting points. The relationship between plasticity and rolling temperature has been previously published the literature [176]. Experiments on sulfides show that they have low deformability just above 1200 ^{o}C. As the temperature decreases to 900 ^{o}C, however, their plastic deformation approaches that of a steel matrix ([174], [177], [178]). A significant body of literature on MnS behavior in steel during hot working has

described the high deformability of MnS during processing steel ([118], [165], [166],[168],[172],[173], [176], ,[179]-[180][181]).

Researchers studied the deformability of inclusions in a steel matrix exposed to a local stress field developing around the inclusions by experimental and theoretical means. The effect of stress field of the photoelastic matrix of different objects is an indirect method used in some experiments to show the influence of inclusions on the steel matrix [182]. Results from a direct method of photoelastic coating of a metallographic section with a nonmetallic inclusion are more attractive because of association of indirect results within dislocations at nonmetallic inclusions by different mechanisms ([183],[184]). This technique also illustrates a different relaxation process between photoelastic resins and nonmetallic inclusions. This method has been used in many applications ([185]-[191]). Studies on strain distribution around inclusions using this reported that size and extension of the elastic field generated around the inclusion control plastic deformation near the inclusions by controlling the spread of plastic deformation and formation of the dislocation from inclusions [156].

The Metal Research Image Analyzing Computer provides a tool to compute the mean inclusion dimensions ([192]-[195]). Luo and Ståhlberg have used the mesomechanical approach to theoretically analyze the deformation around MnS inclusions in a steel matrix in the case of hot rolling [196]. They conducted an automatic image processing technique to show the change in orientation as well as aspect ratio in MnS inclusions.

A number of simulations using FEM have been designed to predict the deformation of inclusions in the matrix. Thomas and Hancock [178] presented the results of an axisymmetric analysis of rigid or elastic spherical inclusions in matrix governed by power law hardening with elastic-plastic materials. Gilormini and Germain [196] conducted FEM computations of the

deformable inclusions in an elastic-plastic matrix for a plane or axisymmetric case. They deployed power law viscous materials to simulate the tensile traction deformation of cylindrical and spheroidal inclusions with different hardness, aspect ratio and rate sensitivity**.** Nagayama and his co-workers [198] used a Von Mises yield criterion in their FEM analyses to model the deformation of rigid-plastic inclusions in an inhomogeneous material with different yield stresses. Work on large plastic deformation of an inclusion-matrix system for different inclusion shapes were subsequently published ([199], [200]).

2.3.4 Previous research on the cooling

Parameters affecting the cooling rate include: quenchant type, quenchant temperature, agitation velocity, viscosity, agitation type, aging, polymer foaming, polymer degradation, part material, geometry, part area, part volume, density, specific heat, oxide layer, surface roughness, suspension, carbon content, grain nature, grain size, plastic deformation and number of other issues [201].Therefore, to perceive the goals of the experiments in this research work, it is important to review the previous work on three main subjects involving in the determination of optimum cooling rate of steel from the critical temperature ranges. These experimental topics are quenching, phase transformation and crack formation in steel subjected to thermal gradients.

The subject of optimum cooling rate is mainly related to the quenching topic. Consequently, results of research accomplished in the quenching subject helps to establish the desired cooling rate through the material. Quenching is accelerating cooling with a quenchant such as air, water, oil, salt, natural or vegetable base quenchant, polymers and other chemical compounds [202]. Liquid quenching is more common in industry because it furnishes a quenching process with homogeneous and more controllable heat transfer from the hot body.

Three stages of quenching for a liquid quenchant are: vapor stage, boiling stage and convection stage [202].

Time-Temperature-Transformation diagrams (TTT) for any grade of steel is the outcome of controlled cooling rate using the cooling agents. However, there are two problems with these controlled cooling methods. First, any participation may vary the shape of the TTT diagram and, secondly, as the cooling rate increases, the residual stresses stored in the bulk material increases as well [203]. The first factor makes the final product case dependent on the steel grade with different chemical composition and the second one may result in higher defect density in the microstructure. The other problem is that the TTT curve may not maintain its shape in the presence of different levels of residual stresses. These facts make the prediction of quenching complicated. There are many publications on the quenching topic, which provides the information about different quenchants and the thermodynamic and chemical properties ([201], [202],[204]-[201][207]).

In a more general definition, quenching is a metallurgical process for controlled extraction of heat from material depending on the interfacial chemical properties of the material quenched ([201] [202], ,[205] ,[206]. Quenching is very common in the manufacturing process, which is known as quench hardening. Factors, which are considered in quenching hardening, are residual stresses and distortion, prevention of crack initiation, microstructural evolution necessary to improve properties (wear resistance and toughness), and meeting the desirable hardness [208]. Application of quenching in steel manufacturing is done to obtain the desired mechanical properties such as, hardness, yield strength, and ductility [134]. The material properties are controlled by a quenching process in many industrial applications, e.g., in engine

components for wear and durability, aircraft components for strength and fracture toughness, bicycle frames for strength, lightness and durability [202].

Parameters, which shall be considered in the quenching process of a bulk material, are desired suspension, cooling rate, cooling nature, heat transfer coefficient, residual stress, desired hardness and other material properties, distortion tendency, and cracking potential [201]. For liquid quenchants, heat transfer rate is the most important factor in controlling the heat transfer rate and it decreases exponentially with increasing viscosity [205]. Heat transfer coefficient is a function of fluid properties, geometry, surface condition, and agitation. Heat transfer depends on heat transfer coefficient, time and location within the bulk material [204]. Rewetting process and agitating as well as the variation of chemistry of the quenchant during the cooling process must be monitored and controlled in designing an optimum cooling rate [206].

Cooling steel from the austenite temperature may result in different transformation sequences and the allotriomorphic phase proportions such as ferrite, pearlite, Widmanstatten ferrite, bainite and martensite [71]. The discussion on solid-solid phase transformation has been the subject of many conferences around the world [209]. Many of these studies were devoted to predict the microstructure at room temperature resulting from these transformations. A large body of literature exists in which the subject of solid-solid transformation has been discussed from different aspects ([210], [211]). Griffiths [212] discussed the critical points of phase transformation in solids. Soffa and Laughlin [213] discussed diffusional instabilities by examining data from observations, X-ray, electron diffraction, transmission electron microscopy (TEM) and atom probe field ion microscopy (APFIM). Yeomans [214] used mean field theorems in studying phase diagrams and critical phenomena by implementing it in the calculation of phase diagrams.

Study on precipitation of pro-eutectoid phases in the literature gives the microstructural analysis for different temperature and positions of samples [215]. Two main transformations determined the phases formed from austenite. These mechanisms are reconstructive transformation and displacive transformation. Reconstructive transformation is a slow rate process controlled by diffusion. The main resulting phases of this transformation are ferrite and pearlite ([71], [216]-[219]). It occurs in the high temperature regime by movement of atoms at the γ/α transformation interface. Bhadeshia [220] has suggested some modes to decrease the temperature of solid-solid phase transformations. Driven force for polymorphic austenite to ferrite transformation is greater than grain growth by two orders. Therefore, non-metallic inclusions get involved in the decomposition of austenite rather by original austenite grain size and concentration than mobility of the α/γ boundary [221]. Displacive transformation is a rapid process without any movement of atoms across the γ/α transformation interface. This transformation occurs rather via deforming shape of an invariant plan strain by a large shear component. Austenite phase mainly transforms to Widmanstatten ferrite, bainite and martensite [71].

In γ/α transformation, austenite with an FCC crystal unit cell with slow cooling rate is transformed to the BCC ferrite unit cell. Martensite is a diffusionless process and carbon is left in solid solution, which results in transforming FCC austenite to BCC or BCT lattice under high cooling rate processes [222]. Speich and Miller [223] stated that the amount of martensite in the final microstructure depends not only on carbon content but intercritical phase transformation temperature and given cooling rate. Maropoulos and Ridley [135] studied tempered martensite microstructures and found a relationship between their chemical composition and thermal history with their mechanical properties. Zhuravlev [224] performed tensile tests in quenched samples

and concluded that in the presence of a stress field the martensitic point and the plastic behavior of material not only change the temperature but change in the temperature. Research on the composite materials with fiber or particles embedded in the body led to predict fracture formation due to inhomogeneity of material, as well [135].

Kobasko's [225] experimental results showed that the tendency for crack formation is higher with a range of cooling rates and it decreases for the cooling rate higher or lower than this critical cooling rate range as a function of quenching rate. The factors governing the behavior of material at high temperature are time, temperature, stress, and environment or atmosphere. At low temperature mechanical behavior like fatigue damage, is controlled by the level of the mean stress, amplitude of stress fluctuation and number of cycles [226]. Quasi-cleavage may occur within regions of grains with different orientation in quenched and tempered steels, and they may result in lower resolved normal stress and, consequently, ductile fracture mode [227]. Three major fracture modes in the microstructure are ductile fracture by nucleation and growth of voids, and brittle fracture via trans-granular fracture or inter-granular separation. The trans-granular cleavage is the most common one. In ferrite, it adopts both Griffith (energy) and Orowon (stress) criteria and, according to the Hall Petch equation, grain refinement requires higher debounding fracture stresses [228]. Kametani [229] analyzed the length of longitudinal cracks on the surface of continuously cast steel slabs and gave crack frequency as a function of crack length using fractal distribution methods. Quantitative characteristics of the crack growth are peak load of the force displacement curve, nominal specific energy of the formation of new unit surface, average force, fractal dimension of fracture surface and height of the surface roughness peaks [230]. Cracks initiate or propagate in a different manner depending on the microstructure, composition and properties. Tensile test experiments on tool steel showed that

cracks initiate (or exist) in the carbide band growth straight forward in the matrix and after kink type dislocation in the carbide rich region split in the same direction of the region then jump to the next carbide band and grow in the same manner and so on ([231],[232]).

Computer simulations have been deployed in the last decade to lower the cost of microstructural experiments. Much work on modeling of thermo-mechanical treatments of steel has provided the capability to predict the final microstructure ([233]-[236]).

2.3.5 A review on previous numerical modeling on cooling cast steel

Qualitative information about temperature evolution, cooling rate, residual stresses and distortion, assist the realistic modeling. Smolijan [237] predicted the strain and residual stress evolution within a geometrically complex specimen (e.g. cylinder, cones, spheres, etc) dealing with estimation of microstructure and hardness distribution after quenching using a mathematical method based on the finite volume method and Jominy tests results. He did not consider in his simulations any existence or formation of anomalies or defects before or after quenching. A quenching simulation for more complex geometry such as stepped cylinder and axially symmetric steel workpiece were published by other programmers ([238], [239]). Chen and Meekisho [240] developed the model of a quenching process to study the effect of actual service condition aspects such as the presence of holes or notches using temperature dependent materials properties. Bhadeshia [241] extended Johnson-Mehl-Avrami-Kolmogorov model to study two linearly dependent precipitation isothermal reactions. Reti et al. [242], developed a phenomenological kinetic model flexible for both isothermal and non-isothermal conditions to describe the multiphase diffusional austenite decomposition which occurs during quenching of low alloy hypoeutectoid steel after austenization through pseudo-autonomous differential

equations. Another purpose of their model was to determine the hardness in a bar for a specific composition and diameter. They found a satisfactory agreement between their numerical and experimental results.

The evolution of internal stresses in the microstructure during quenching is influenced by volume variation and transformation plasticity. Many publications are available on the simulation of the phase transitions in steel ([243]-[249]). Different mathematical models were presented to prescribe the eutectoid phase transition ([250],[251]). Some researchers implement the classical nucleation and growth theory to model the microstructure of a given austenite grain size cooling down with different rates to the ferrite- transformation temperature range [236],[252]-[254]). The FEM technique results for stress analysis of $\alpha-\beta$ hydrogen transformation in the Nb-H system were presented in published numerical models [255]. According to the atomistic information reported about FCC and BCC structure, researchers found the cohesive energy of BCC and FCC to be -4.28 eV/atom, -4.25 eV/atom and lattice parameter of 0.2867 nm and 0.3642 nm, respectively [256]. The energy of grain boundaries of γ in Fe was found to be 756 mJ/m2 ([257], [258]). A model of BCC material between two FCC blocks shows that the relaxation of atoms in pure FE blocks are small within both BCC and FCC structures but it is higher among atomic planes adjacent to the inter-phase boundary of a two crystal structure [259]. This may cause larger atomic displacement and atomistic misfit at the boundary of two phases. A microstructure evolution computer model, was developed by programmers using a combination of the stochastic field kinetics theory of phase transformation with the general strain energy formulation for any diffusional or diffusionless coherent transformation [260].

Homberg [261] modeled, mathematically, the phase transformation in eutectoid carbon steel for transition of the diffusive austenite pearlite coupled with non-diffusive austenite martensite. He defined characteristic Heaviside functions for incubation time of the new phase in implementation of Scheil's Additivity rule and the Johnson –Mehl equation to enhance the ability of these methods in prescribing the eutectoid phase transformation. He improved the model to be an irreversible process, which is essential for the growth of the new phase. However, his results fell beneath the experimentally measured ones and he did not guarantee the repeatability of the results or applicability of the method for all types of the steels with different chemical compositions. Gur and Tekkaya [208] combined thermal analysis and microstructural analysis with small strain elastic-plastic analysis to predict the temperature distribution, the progress of phase transformation, the evolution of internal stresses and residual stresses during quenching for axisymmetric steel components. They deployed the Prandtl-Reuss elastic-plastic constitutive equation with Scheil's additivity diffusional transformations method [262] and the Johnson-Mehl-Avrami equation ([263], [264]) and martensitic transformation of Koistinen-Marburger equation [265], in an Ortiz and Popov [266] trapezoidal rule in their finite element code. Umansev [267] used mean field theorems to discuss and simulate its effect on transformation for the mechanism of meta-stable phase production. An FEM process model of quenching of steel 1080 steel cylinder in water demonstrated austenite-pearlite and austenite-martensite transformation and suggested an elastic-plastic stress analysis [268]. Lusk and Jou [269] used four sets of differential equations to predict austenite decomposition to ferrite, pearlite, bainite and martensite with acceptable precision. The crack formation or propagation subject is studied by the classical fracture mechanics analysis.

Clarification of the fracture parameters such as stress intensity factors (SIFs) and fracture behavior (e.g. fracture path) are both necessary for prediction of crack propagation [270]. Different researchers ([271]-[275]) investigated the effect of phase transformation on the residual stresses within quenched bodies. These residual stresses have an important role in changing the soundness of the steel during cooling. Mishnaevsky [230] et al. discussed the crack propagation under dynamic load in real and quasi-real idealized two-phase microstructure of carbide in the steel matrix microstructure model for tool steel material. They use multiphase finite elements (MPFE) in a mesomodel, which have real microstructure of the steel with actual mechanical properties of steel obtained from micro-indentation and SEM-in-situ-micro-bending tests. They considered various carbide distribution in band-like (typical for as cast state), net-like (hot formed state) and random microstructure to investigate three main mechanisms of increasing the fracture toughness of steels (crack deflection by normally oriented carbide layers, crack growth along the carbide network, crack branching). They concluded that increasing the crack resistance of the material may not increase the material's fracture toughness but fracture dimension of the fracture surface enhances the specific energy of fracture. They did not consider any thermal stress in their model and the crack formation is simulated by an elimination technique, which, practically, leads to eliminating material undergoing high stresses at the critical crack tip zone. Another problem of their model was that the behavior of the crack in the microstructure was simulated in the different models. There are some similarities between multiphase microstructure and composite material in the sense of arranging the fracture model set up. Wittmann [276] used the Fictitious Crack Model (FCM), to predict the crack formation in composite material. The composite material in his simulation is concrete but it contains a several types of behavior similar to there of multiphase microstructures since the concrete is a mixture of components with

different material properties and it has crack due to shrinkage as the concrete's moisture is reduced. Suzuki et al. [277], simulated a model of the formation of transverse cracks on continuously cast slabs and confirmed their results by placing rectangular test pieces with either V-notch or semi-circle notch or oscillation marks under a similar temperature gradient to that in the solidified shell in the mold.

Saimoto and Nistani [278] had challenged with a contact problem in addition to ordinary fracture mechanics analyses in their crack propagation under compression biaxial loading. The maximum principal stress criterion can estimate the direction of a crack tip using the ratio of mode I and II stress intensity factors. In the literature [279] a molecular dynamic (MD) technique was deployed to the study of brittle ductile behavior at the crack tip in simulation of crack growth in iron under quasi-static loading in mode-I. The result of MD simulation showed the crack initiation is localized in the vicinity of the crack tip by a shear process but the defects disappear as the crack advances. Some researchers discussed the void initiation from second phase particles using continuum plasticity and dislocation models [280]-[283]). Other researchers modeled the nucleation and propagation of voids under tensile forces [284],[285]). McClintock [286] has modeled the fracture by gradual lining up of the voids by localized shearing in homogenous growth and coalescence of voids. Macro crack propagation simulation with size effect properties in some work [287] was presented to model ship collision, which poses a huge numerical model. Then the results were verified with tensile tests of center notched plates with pre-strains. Some researchers [288] have used a Global Extraction element-by-element (GEBE) to simulate crack propagation to get a faster results compare to other methods.

Nevertheless, many theoretical models were suggested to prescribe the steel quenching by researchers. Most of them, if not all, relied on the simplifications that rendered the unrealistic outcomes [237].

3.0 OBJECTIVES

The major objective of this dissertation is to find the optimum accelerated cooling rate for as-cast continuously cast steel slabs during solid-solid phase transformation without sacrificing the quality of the steel by lowering soundness of the steel grade. The optimum cooling rate is related to increasing the productivity of the steel making process as a result of higher efficiency of the cooling process of the steel slab, which is in the austenite temperature range. The goal is to cool the steel slab as fast as possible in consistent with the industrial practice. However, cooling rate beyond the critical range may generate new voids, microcracks and even cracks depending on the grade of steel and the microstructure. It may also cause the previous defects formed during peritectic transformation and solidification process to grow, deform or propagate. A high heat transfer rate may aggravate the ripple at the surfaces of the prior cracks.

In this work, the target is to demonstrate how the major sources of stresses in cooling as-cast slabs are responsible for increasing the density of voids, flaws, microcracks or large cracks. The sources of stress that will be examined in this work are;

a) Thermal stresses

b) Volumetric stresses

c) Internal stresses

d) Phase transformation stresses

e) Stresses due to interaction of phases existing in the microstructure

The main objective of this work deals with these stresses and demonstrating their influence in determining optimum cooling rate for a specific grade of the steel. Particular attention will be the examination of the residual stresses built in the microstructure because of solid-solid phase transformation. Furthermore, this research work is intended to compare the residual stresses accumulated in the microstructure in cooling hot slab from three different temperature zones known as supercritical, intercritical and subcritical.

The interaction between the anomalies and steel matrix may raise some of the stresses mentioned above during the cooling process of the as-cast slab steel which may result in degrading the soundness of the steel. Therefore, the presence of the inclusions and other types of defects in the as-cast steel influence the critical accelerated cooling rate. To increase the accuracy of the computation of optimum cooling rate, this research work is intended to offer an extension of an ultrasonic, non-destructive technique (NDT) image processing and analysis to characterize the anomalies in the microstructure of the as-cast steel slabs from the ultrasonic NDT images. The major objectives of the NDT work are: 1) to identify the type and location of defects in the slabs; 2) to verify the results from NDT using microstructural analysis; and 3) to use NDT to assess the level of anomalies or defects in the slabs and the distribution of each type of the defect.

Another objective of this dissertation is to study how the presence inclusions in the steel matrix may enhance the degradation of the steel's soundness. One question in this research is to understand how the behavior of the inclusions embedded in the steel microstructure during cooling generates voids and flaws. Another goal of studying the interaction of the inclusion and steel matrix during cooling is the effect of the inclusion-matrix interface on the formation of stress concentration zones in the steel microstructure. To answer the latest question, different

types of the inclusion-matrix interfaces are to be defined in the simulations presented in this research work.

The goal of cooling experiments in this dissertation is to study the effect of the cooling rate in changing the defect density in the microstructure for steel with different chemical composition and cooling history as well as to collect the data for the verification of the analytical results obtained from FEM analysis.

This dissertation is introduced a numerical analysis algorithm using ANSYS, a commercial FEM analysis software package, to achieve the objectives of this dissertation. Included in this work is detection of regions of the microstructure vulnerable to the formation of the defects due to the strains introduced to the microstructure by stresses mentioned before and particularly the phase transformation stresses. The FEM algorithm is to be designed to study the effect of the shape and size of grains, grain boundary properties, the slab geometry and cooling method on the accumulation of the residual stresses in the microstructure.

The ultimate intention of this dissertation work is to provide a guideline on cooling process set up in continuous casting steel production for different steel compositions through NDT tests, cooling experiment tests and FEM numerical analyses. Therefore, this work will help to improve the efficiency of the cooling rate for a specific grade of steel by increasing the productivity of steel and decreasing the inventory period of solidified continuously casting steel strand (slabs, blooms, and billets) in the production line without degrading the quality.

4.0 GOVERNING EQUATIONS AND RELATED FORMULA TO THE OBJECTIVES

4.1 HEAT TRANSFER BACKGROUND

Heat transfer in continuous casting, as in other in process heat exchange, contains both heat transfers in the bulk as well as interfacial heat transfer rate [289]. A basic description of the heat transfer mechanism within the scope of this dissertation is presented to enlighten the link between the sources of the residual stresses and the FEM numerical equations. It is well known that heat transfer from a higher temperature point to a lower temperature point takes place in three modes: convection, conduction and radiation. During transferring heat by conduction, atoms are agitated and heat transfers without any motion of material as a whole. The radiation of the slab also depends on the thermal properties of the steel and the cooling rate is mainly determined by the convection. The heat transfer rate by convection is controlled by properties of the convective agent. To perceive the concept of material properties in the modeling, it is useful to have a brief discussion concerning the basic heat transfer equations for the three types of heat transfer.

The concept of atomic and molecular activities gives the heat flux equation to determine the heat transfer by conduction in solid material and the resultant temperature distribution within

the bulk material. This equation is known as Fourier's law, which is presented as following [290],

$$q = k\frac{\partial T}{\partial x} \qquad \text{(Eq-1)}$$

where k is thermal conductivity of material. Thermal conductivity, (k), is temperature dependent and its dependency is different for different types of material. The shape of the curve of thermal conductivity of steel with respect to temperature can be linear descending or ascending, convex, hump, V-shape etc. An extensive discussion of the conduction equation of the continuous casting process can be found in [289]. At the surface of hot solid, the heat transfer by the motion of the fluid adjacent to the surface with lower temperature compare to the solid body. The heat flux transfer by convection is given by Newton's law,

$$q' = h\,A(T_W - T_\infty) \qquad \text{(Eq-2)}$$

where A is the contact area and h is the convection heat transfer coefficient, T_W and T_∞ are temperature of the wall and fluid, respectively. At very high temperature, radiation has a very effective role in transferring temperature. It is energy transfer by electromagnetic waves transport between two bodies. In the cooling as-cast steel, the first body is the strand of cast steel and the cooling agent with its specified temperature is considered as the second body. The Stefan-Boltzmann equation is used to incorporate the effect of radiation in cooling the hot sample into the mode;

$$q'' = F_\varepsilon F_G \sigma A(T_1^4 - T_2^4) = \varepsilon\sigma A(T_1^4 - T_2^4) \qquad \text{(Eq-3)}$$

where T_1 and T_2 are temperatures of the first and second body and σ is the Stefan-Boltzmann constant, F_ε and F_G are emmissivity and geometrical view factor functions,

respectively. The emmissivity function (ε) is the material characteristics whose value is the combination of emmissivity and geometrical view factor functions.

Radiation is in the range of the infrared region (wavelengths: 1 nm - 750 nm) of the electromagnetic spectrum. The Stefan-Boltzmann constant refers to "blackbody radiation" or "cavity radiation". The emmissivity function is a correction factor depending on the color of the body, which radiates heat to the second body. Planck's law gives the effect of color of the body due to temperature in transferring heat. The changes in the emission power density can be seen in the graph presented in Figure 14.

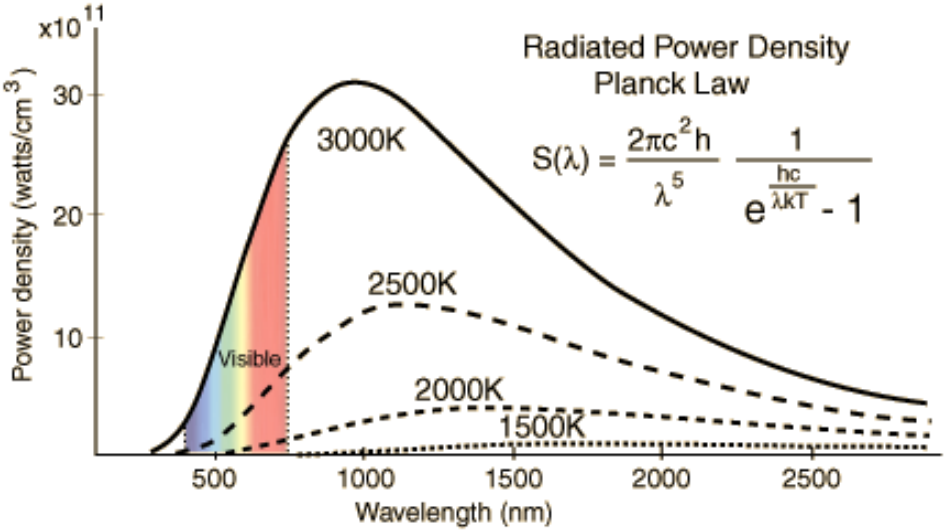

Figure 14 Radiation curve for different wavelength at a given temperature [291].

Steel has a generally dark grey color at room temperature. It can be seen from Figure 14, for a temperature below 1500K that the change in color is not very effective for inducting the amount of heat transfer from the hot body. Therefore, an emmissivity of 0.8 for grey color is considered in the simulation, although the color of the sample is red when is pulled out from the oven in the experiments presented in this dissertation or just solidified in the continuous cast steel production line.

The structural effect of the large changes in the temperature of material is thermal expansion or contraction. Thermal expansion is due to altering the energy that is stored in the intermolecular bonds between atoms. When the stored energy changes, so does the length of the molecular bond in response to heating up or cooling down [292]. The equation of linear expansion coefficient suggested by Incropera and DeWitt [293] is shown in Equation 4

$$\alpha_L = \frac{1}{L_o}\frac{\partial L}{\partial T} \qquad \text{(Eq-4)}$$

The coefficient of thermal expansion, α, in K^{-1} at constant pressure is calculated from measuring of the volume change of the material by Equation 5 [292];

$$\alpha_P = \frac{1}{V}(\frac{\partial V}{\partial T})_P \qquad \text{(Eq-5)}$$

where L_0 is the original length and L is the new length. Then the volumetric expansion coefficient for the isotropic material is $\alpha_V \cong 3\alpha_L$. The linear coefficient of expansion, in general, for steel, is 12 x 10-6/^{o}C or 6.5 x 10-6% F.

The combination of all three types of heat transfer is calculated by a total heat flux technique away from interface as q=q(c) + q(r), where q(c) is heat loss by convection and q(r) is cooling by radiation. Then the effective heat transfer coefficient is obtained by the next equation [289];

$$h_e = q/(T_l - T_s) \qquad \text{(Eq-6)}$$

This coefficient gives the rate of heat flux away from the interface with respect to the temperature difference between the interface temperature and the surrounding temperature.

The temperature variation in the bulk of isotropic material undergoing cooling or heating process can be computed using overall balance of energy for a transient temperature gradient [294];

$$k(T)\nabla T + \dot{q} = -\rho c \dot{T} \qquad \text{(Eq-7)}$$

Constants ρ and c are density and specific heat of material, respectively. The thermal conductivity of the body (k) depends only on temperature and therefore it can be moved out of the spatial derivative. The possible energy generated in the material is stored in $\dot{q}$. The negative sign is for reduction in the thermal energy.

4.2 STRESSES INTRODUCED DURING COOLING THE AS-CAST SLAB

The concepts in heat transfer have strong influences on the generating of stresses in the microstructure during cooling and limitations on optimum cooling rate for specific steel from a given temperature to ambient temperature. The solidification of molten steel for each section of a slab ends in the secondary cooling zone at the so-called triple point in which the segregation from the side surfaces reaches the upper and lower surfaces' segregation.

The extension of the triple point in the cooling symmetrical plane defines the centerline segregation in the slab. The steel slab cast from steel strand can be at the austenite temperature or supercritical, intercritical or even subcritical temperature range. The as-cast steel loses its thermal energy by all three types of heat transfer. The slab must be cooled down to room temperature for stocking, delivery or further machining. The starting temperature in the cooling process of the slab categorizes the cooling process as supercritical, intercritical and subcritical regions in the Fe-FeC phase diagram.

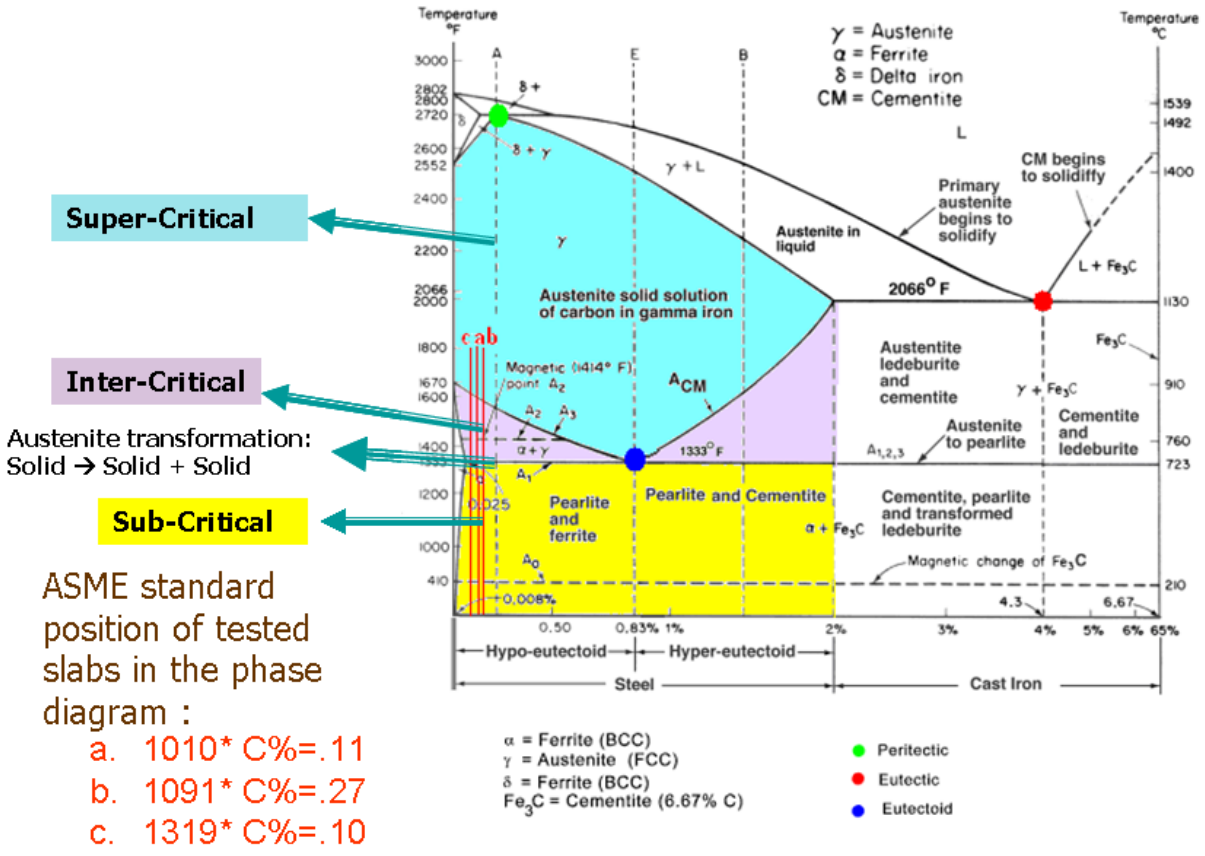

Figure 15 Three classes of cooling processes according to the starting temperature for the cooling process.

These regions shown in Figure 15 by blue, violet and yellow color, are for solid steel at temperature ranges T>T [A_3] (T [A_{c3}]), T [A_1] < T <T [A_3] (T [A_{c3}]) and T<T [A_1], respectively. Figure 15 shows that among three phase transformations, only solid-solid phase transformations are involved in the stresses introduced during cooling the slab if the starting temperature of the cooling process is at the supercritical or the intercritical region in the phase diagram.

This phase transformation is the eutectoid point in the Fe-C diagram. The cooling curves for the steel grade of the tested slabs in this research work are marked by red lines a, b and c for grade steel 1010*, 1319* and 1091*, correspondingly. The chemical composition of the steels used in this investigation is presented in Table 2.

Table 2 Chemical composition of steels (wt %) used in the experimental procedures in this dissertation.

Element	Heat-160530 1010* Grade	Heat-210191 1319* Grade	Heat-554754 1091* Grade
C	0.114	0.103	0.273
Mn	0.489	1.592	1.340
P	0.009	0.0144	0.0127
S	0.0039	0.0025	0.0031
Si	0.041	0.334	0.199
Cu	0.005	0.004	0.026
Ni	0.003	0.003	0.015
Cr	0.005	0.137	0.023
V	0.001	0.059	0.003
Mo	0.001	0.001	0.013
Nb	0.001	0.061	0.002
Sn	0.001	0.001	0.002
Al-total	0.0329	0.0282	0.0397
Al-soluble	0.0303	0.0262	-
Ca	0.0025	0.0027	0.0019
N	0.0042	0.0056	0.0042
As	5 e-4	8 e-4	3 e-4
Ti	0.0007	0.0154	0.0004
B	1e-4	2 e-4	1 e-4

As it can be seen the chemical composition of each the slab is not exactly the same as its designation therefore an star (*) were placed next to the designation number for the rest of the dissertation to show these differences. It was reported that the density of cracks and distortion is higher as the carbon equivalent (CE) increases. The formula to calculate the value of CE is obtained from experimental results and it has been reported in the literature according to the alloying elements in the steel [289], [204]). The more common CE formula is as follows [295];

$$C_{eq} = \%C + \left(\frac{\%Mn + \%Si}{6}\right) + \left(\frac{\%Cr + \%Mo + \%V}{5}\right) + \left(\frac{\%Cu + \%Ni}{15}\right) \quad \text{(Eq-8)}$$

The review on the study of continuous cast steel's microstructure elaborates the reason for the presence of anomalies in the cut slab. These anomalies are also play a role in determining efficient cooling up to a certain level because of nucleation of stress concentration zones around the inclusions due to misfit contraction of two phase's material.

The efficient cooling rate for the slab is fundamentally controlled by the stresses generated in the microstructure during cooling. These stresses may develop to create voids or cause void growth. They may also form or propagate microcracks or cracks. In all cases, the stress level should reach the yield stress to plastically deform the slab surface or within the microstructure. The developed stresses due to cooling process should overcome the resistance of the material to plastic deformation, given by the Hall-Petch yield stress expression. This strength, in expanded form, is given as follows [296];

$$\sigma = \sigma_o + \Delta\sigma_S + \Delta\sigma_T + \Delta\sigma_P + \Delta\sigma_D + \kappa_y d_F^{-1/2} \quad \text{(Eq-9)}$$

where σ is the Hall-Patch yield stress, σ_o is the lattice friction stress and $\Delta\sigma_S$ [297], $\Delta\sigma_T$ ([298], [299]), $\Delta\sigma_P$ [298], $\Delta\sigma_D$ [300] are the stresses corresponding to solid solution, texture, precipitation and dislocation effects, respectively. The last term in Equation 9, $\kappa_y d_F^{-1/2}$

[299], is related to the ferrite grain size where, κ_y is the Hall-Patch constant and d_F is the ferrite grain diameter. However, the slabs have solidification (dendritic) structure hence the last term in the Hall-Petch expression does not apply to the as-cast slabs. Consequently, it is important to discuss in detail the stresses produced in the microstructure as a result of cooling the slab. The stresses developed due to thermal, mechanical or transformation strains during the cooling stage of the as-cast steel are as follows;

f) Thermal stresses

g) Volumetric stress

h) Internal stresses

i) Phase transformation stresses

j) Post phase transformation stresses (interaction of phases)

Table 3 Relationship between cooling process and stress field developed during cooling of the slab.

Imposed Stress	Super critical	Inter critical	Sub critical
Thermal stress (thermal gradient)	Yes	yes	Yes
(different in volume contraction between steel matrix and anomalies)	Yes	yes	Yes
Internal stress (e.g. dislocation)	Yes	yes	Yes
Phase Transformation stress (geometrical modification)	Yes	yes	No
Post phase transformation stresses (interaction of phases)	Yes	yes	Yes

Any of these stresses, individually or in combination, beyond the inherent material strength can change the soundness of the final cast steel product during cooling process. At the interface of two phases formed by austenite phase transformation within the microstructure or

inclusions and steel matrix, these forces must overcome the adhesion forces between interfaces to separate the contact surfaces. Table 3 resents stresses involved for each class of the cooling process of the slab. Knowledge about the sources of these stress fields helps to understand the relationship between the cooling process and stress field in Table 3 Thermal stresses developed during the cooling process are explained below.

4.2.1 Thermal stresses

Thermal stresses are generated from the poor thermal conductivity of the steel. This divides the slab into different temperature zones and, consequently, defines a thermal gradient through the thickness. Linear thermal strain for the thickness of each thermal zone is given by Equation 10:

$$\delta_h = \alpha(\Delta T)L \qquad \text{(Eq-10)}$$

where α is the thermal linear expansion (contraction) and is different for each grade of steel. Onink et al. [301] measured the thermal expansion coefficient of ferrite (β_α) for the temperature range 800-1200 K to be $1.75\text{x}10^{-5}$ (K^{-1}). However, the volumetric thermal expansion coefficient for each phase is not constant during cooling and it is temperature dependent. Metallurgists deployed the dilatometric method to calculate the thermal expansion coefficient for austenite [301] and martensite [302] as a function of temperature and atomic percent of carbon as follows;

$$\beta_\gamma = (24.9 - 0.5 \times C_\gamma) \times 10^{-6} \qquad \text{(Eq-11)}$$

$$\beta_M = (14.9 - 1.9 \times C_M) \times 10^{-6} \qquad \text{(Eq-12)}$$

where β_γ is the austenite thermal expansion coefficient and β_M is the martensite thermal expansion coefficient. The unit of both austenite and martensite thermal expansions are in K^{-1}.

C_γ and C_M are atomic percent of carbon content in austenite and martensite, respectively, and they can be calculated from the weight percentage of carbon content in austenite and martensite which can be extracted from phase diagrams for each grade of steel. The conversion of weight percent to atomic percentage can be calculated using the next equation;

$$C_{A\%} = \frac{C_{AW} \times Fe_{W\%}}{C_{AW} \times Fe_{W\%} + Fe_{AW} \times C_{W\%}} \times 100 \qquad \text{(Eq-13)}$$

Subscripts (W%), (A%) and (AW) stand for weight percentage, atomic percentage and (AW) indicates the atomic weight of carbon and iron, respectively. In using Equation 13, iron carbon microstructure has been considered because the summation of percentages should be 100 and other minor contamination can be neglected.

Therefore, a stress field is distributed at the interface of the thermal zone, which in turn creates a region with compression stresses. These stresses increase the bending moment and, if it exceeds the yield strength of the slab steel, it may cause separation of the surfaces at the border of the thermal zone due to different thermal contraction in depth for each zone or microcrack or crack depending on the thermal gradient at the zone surfaces. Morris [228] explained how change in the temperature affects the Hall-Petch equation and also ductile to brittle transition temperature, which alters the critical yield stress, and the behavior of the trans-granular crack. On the other hand, in the case of very high cooling rates, reheating of the middle section by the hot central section will develop tensile stresses arising from the expansion of this section compared to a cooler layer above it, which is in the stage of shrinking. If the level of tensile stresses developed in a region gets higher than the tensile properties of the slab steel, rupture in the texture may develop. As the temperature of the slab increases, the built-in thermal gradient in the microstructure is bigger, so this type of stress distribution appears to be more effective in the supercritical region than in the subcritical region. Aketa and Ushijame [303] used the same logic

for explaining crack formation due to thermal gradients during solidification process of the steel which has much higher temperature than just the torched off slab and, consequently, the thermal stresses are more pronounced in that temperature range.

4.2.2 Volumetric stress

Volumetric stress fields are generated during cooling since the material properties including volumetric thermal expansion (contraction) of the microstructure are different for different steel's phase crystals as well as inclusions, voids and cracks. The relation between thermal stress and displacement between atoms due to changes in temperature is maintained by the thermal expansion coefficient in the stress-strain relationship. Equation 14 gives the coefficient of compressibility, β, in atm^{-1} whose value determines volumetric thermal expansion of the substance while the temperature is held constant [304];

$$\beta = \frac{1}{V}(\frac{\partial V}{\partial P})_T = \frac{\rho}{m}(\frac{\partial V}{\partial \rho})_T(\frac{\partial \rho}{\partial P})_T = -\frac{\rho}{m}\frac{m}{\rho^2}(\frac{\partial \rho}{\partial T})_T = -\frac{1}{\rho}(\frac{\partial \rho}{\partial P})_T \qquad \text{(Eq-14)}$$

where m is the atomic mass of the component. Equation 14 gives the relation between density, which is a material characteristic in a given boundary condition, and the rate of the temperature rise. Hence, different materials in a composite structure exposed to the same forces, can be compressed at a different rate during cooling and this may cause separation between intermediate contact surfaces of two phases in contact or growing of the void or propagating the microcracks in the cooling process. Derivation with respect to temperature in Equation 14 shows that for lower temperature range cooling process, volumetric stresses become less effective. This fact can be tracked from Equation 4 as well.

The influence of the presence of volumetric stresses in non-metallic inclusions in ductile fracture has been introduced by researchers via inclusion parameters: total inclusion length per unit area or projected length (P) [144], inclusion mean free path (Λ) and nearest neighbor distance (Δ) [286] with equations 15, 16 and 17 respectively,

$$P = NA \times d \quad \text{(Eq-15)}$$

$$\Lambda = \frac{2\sqrt{2}}{\pi}(1 - \frac{V_V}{P}) \quad \text{(Eq-16)}$$

$$\Delta = 0.349(\Lambda \bar{S})^{1/3} \quad \text{(Eq-17)}$$

where, V_V is the inclusion volume fraction and $\bar{S}$ is the mean surface area of the particles.

4.2.3 Internal stresses

Any arrangement of iron and carbon atoms other than perfect reference crystals may change certain steel properties such as thermodynamic, structural, scattering and chemical properties. The dislocations of the atoms form residual elastic stresses in the crystal. Therefore, dislocation density of the steel microstructure is a key point of the effect of existing internal stresses in selecting the proper cooling process. The disarrangement of atoms is studied in the course of the defects and is classified on the basis of the dimension of misalignment of atoms compared to their otherwise perfect position. The defects may fall in zero (point), one (line), two (area) or three (volume) dimension. As the dimension of the defect increases, its thermodynamic influence in the microstructure becomes more important. Generally, the defects by themselves are not very effective in the cooling process of the slab but the stress field around them can move by the dislocations and combine with other types of stresses embedded in the microstructure or

generated during cooling. This may result in intensifying influences of the more effective stress fields in the cooling slab. In addition, the dislocation density is increasing as a function of stress field according to the following equation [228];

$$n = \frac{q\,\pi\,L\,\tau_e}{G\,b} \qquad \text{(Eq-18)}$$

where G is the shear modulus, q is a geometric factor order unity and pile up length of the dislocation. The residual stresses are embedded in the effective shear stress (τ_e) and it increases as the number of dislocations increase. Then the dislocation density for mean grain size (d), can be calculated from a constant mean real boundary condition, cd^2, as shown next [228];

$$\rho = \frac{N}{V} = \frac{cd^2}{d^3} = \frac{c}{d} \qquad \text{(Eq-19)}$$

where N and V are the number of dislocations within the grain and the volume of the grain respectively. C is a constant that depends on the shape of the grain. Consequently, the stored residual stress is related to the grain boundaries' density and properties. This fact can be deduced from the Hall-Petch equation as well and leads to one of the general errors in the numerical simulations of the localized behavior of the microstructure including crack behavior especially for irregular grain shapes like martensitic steels. It is obvious that modeling with the real size of the grains with their actual distribution is a tedious job but it increases the precision of the numerical simulation. Considering maximum grain size could optimize the simulation by avoiding the risk of neglecting a potential formation of the crack in the microstructure and reducing the difficulties and time of the modeling.

4.2.4 Phase transformation stresses

This is the most severe type of stress during the cooling process and that is why dealing with this type of stresses is the main objective of this research work. When the cooling curve passes the A3 line in the phase diagram, it experiences a solid-solid phase transformation and it is completed with an isothermal process as the steel continue to cool below A1. The start and end temperature of the transformation is determined using cooling curves such that the portion of curve where the transformation is occurring has a smaller slope and is characterized by an isothermal section in the curve, except for steel with eutectoid carbon content whose start and end transformation temperature is the same. During this transformation, the austenite phase with FCC structure transforms mainly to ferrite with the BCC unit cell structure in equilibrium cooling conditions, according to Equation 20;

Austenite [FCC] (0.8 % C)→ ferrite [BCC] (0.02 % C) + Fe_3C [orthorhombic](6.67 % C)

(Eq -20)

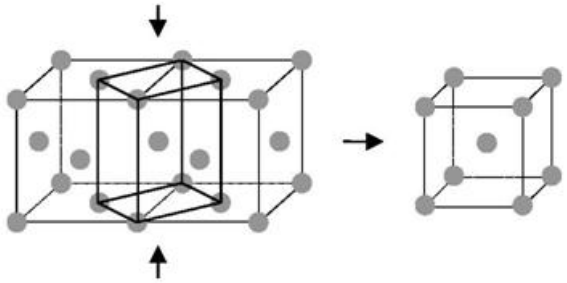

Figure 16 Transformation of FCC unit cell to BCC unit cell.

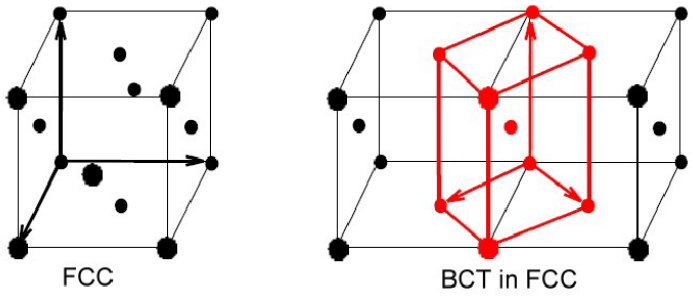

Figure 17 Depiction of diffusionless transformation from FCC to BCT during martensite formation.

Figure 16 shows the transformation of two unit cells of FCC to one unit cell of BCC. During this transformation, a homogeneous compression stress is applied in the direction of the arrows on the unit cells and an expansion stress is exerted in the plane normal to the compression stress. However, under non-equilibrium cooling conditions, austenite may transform to other phases such as martensite, acicular ferrite, bainite and other non-phase structures with special grain boundary structure. This transformation occurs with macroscopic distortion at invariant plane strain by a shear mechanism, which is called shape deformation or shape strain [305]. Figure 17 shows the transformation of the austenite unit cell with FCC structure to the BCT martensite unit cell. This changes the lattice parameter and volume as well as the shape of the unit cell. The transformation is martensitic and the distortion is known as Bain distortion [305]. Application of small steps of Boger and Burgers types of homogeneous "shear" (B&B shear) shows that the Bain transformation is due to minimum energy path for homogenous deformation [306]. The interested readers in martensitic transformation can find more information in [307]. The rate of phase transformation is given by well known Avrami equation [263] as follows:

$$X_F = 1 - \exp(-ct^n) \qquad \text{(Eq-21)}$$

where c and t are constants depending on temperature and are related to constant growth rate, nucleation frequency and shape factor. Rath [308] expanded the Avrami equation to a more general form of constant growth rate of the phase transformation as follows;

$$K_s G_o\,[t-t_o] = \alpha[(X_V)^{1-n}\{\frac{1}{1-n}+\sum_{K=1}^{\infty}\frac{B}{1+K-n}(X_V)^K\}]+ \beta[-(1-X_V)^{1-m}\{\frac{1}{1-m}+\sum_{K=1}^{\infty}\frac{B'}{1+K-m}(X_V)^K\}+\gamma]$$

(Eq-22)

where a=1 and b =0 for $0 \le X_V \le 0.5$ and a=0 and b=1 for $0.5 \le X_V \le 1.0$. K is an index integer and *m* and *n* do not have simple shape and their values are presented in several papers.

Recently, some of the researchers [302] suggested a conversional model based on the relative atomic volume change occurring during the phase transformations and change in solute atoms in the matrix to predict the volume fraction in low alloy steels. They claimed that this method could be used for estimating the volume fraction of ferrite, pearlite, bainite and martensite at room temperature using the lattice parameter of each phase as a function of temperature and solute content. The geometry of a unit cell, and consequently the crystal built by these unit cells change during the cooling process either under equilibrium or non-equilibrium conditions indicated on the iron-carbon phase diagram. Therefore, this type of stress can be called geometrical stress, which is the consequence of a dilatational strain introduced to the matrix by the transformation process. Some inequalities [302] suggested dilatometric tests in determining the start and end temperature of phase transformation and constant monitoring of dimensional change during a heat treatment process. However, since the lattice parameter and, as a result, the volume of the unit cell, changes, during the transformation, it also produces the volumetric stresses in the microstructure. This combination of geometrical stresses and volumetric stresses creates a strong stress distribution at the grain boundaries, which may result

in the cracks along the grain boundaries at the softer phase region. Researchers have also reported the segregation of ferrite network at weak prior austenite grain boundaries (AGB) [34] and oscillation marks ([309],[310]) as a source of crack formation during eutectoid transformation. Tsai and his coworkers [34] were able to take photos of the cracks due to the eutectoid transformation. Figure 18 shows these photos indicating the cracks along the prior austenite grain boundaries in a ferrite film.

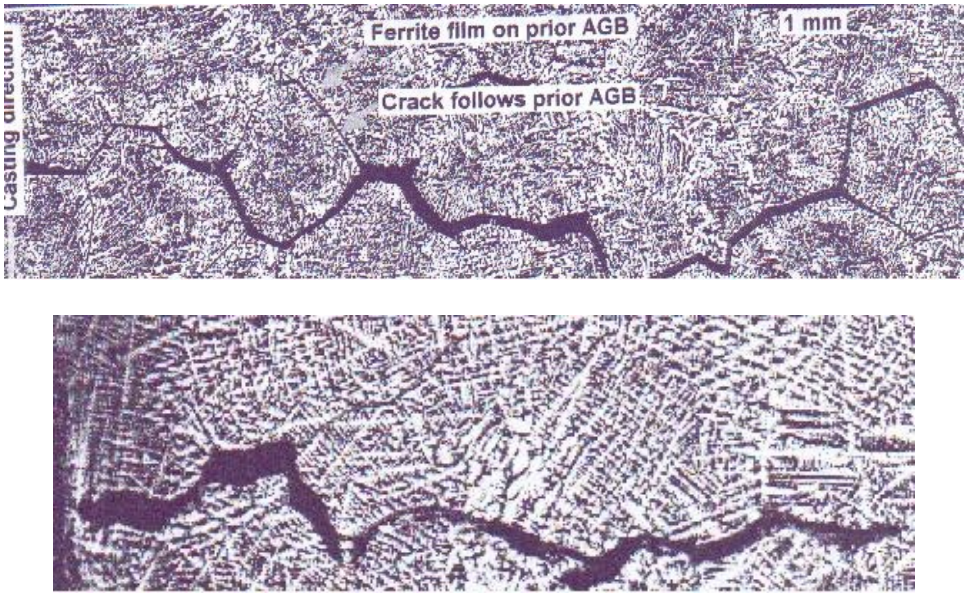

Figure 18 Crack propagation along a ferrite film on prior austenite grain boundaries.

4.2.5 Phases interaction induces stresses

In the discussion of phases, it was mentioned that each phase has its own material properties including thermal properties. It can be observed in the phase diagram that the supercritical region has only austenite phase microstructure and the microstructure of the intercritical region two phases of ferrite and austenite exists. Therefore, the subcritical region can have a steel structure with more than two-phases depending on the cooling rate and cooling process. The type and fraction of the phases at each temperature within the subcritical temperature region can be

deduced from TTT and CCT diagrams. These phases create an inhomogeneity in the microstructure from the material property point of view. The lattice parameter of each phase changes differently with temperature drop during cooling. Researchers have implemented the dilatometric method and calculated the changes in the lattice parameter as a function of temperature and thermal expansion. The equation to calculate the lattice parameter during cooling or heating ferrite is [301];

$$\alpha_\alpha = 0.28863\{1+\beta_\alpha\ (T-800)\} \quad \text{(Eq-23)}$$

and for austenite is [301];

$$a_\gamma = (0.36306+7.83\times10^{-4}\times C_\gamma)\{1+\beta_\gamma\ (T-100)\} \quad \text{(Eq-24)}$$

and for martensite is [302];

$$a_m = (0.28610-0.0002898\times C_M)\{1+\beta_M\ (T-273)\} \quad \text{(Eq-25)}$$

$$c_M = (0.28610-0.00028558\times C_M)\{1+\beta_M\ (T-273)\} \quad \text{(Eq-26)}$$

β_α is 1.75 x 10^{-5} K^{-1} and β_γ and β_M are defined by Equations 11 and 12, respectively. The constant C_γ and C_M are given by Equation 13. C_γ varies by temperature and C_M depends on the quenching process. The lattice parameter of cementite is only temperature dependent and is given by the next formula [311];

$$a_{Fe_3C} = 0.45234\{1+(5.311\times10^{-6}-1.942\times\times10^{-6}\ T+9.655\times\times10^{-12}\ T^2)(T-293)\} \quad \text{(Eq-27)}$$

$$b_{Fe_3C} = 0.50883\{1+(5.311\times10^{-6}-1.942\times\times10^{-6}\ T+9.655\times\times10^{-12}\ T^2)(T-293)\} \quad \text{(Eq-28)}$$

$$c_{Fe_3C} = 0.67426\{1+(5.311\times10^{-6}-1.942\times\times10^{-6}\ T+9.655\times\times10^{-12}\ T^2)(T-293)\} \quad \text{(Eq-29)}$$

The units of all lattice parameters in the above equation, are in nanometers and the equations were verified by researchers' results. This produces a volumetric stress field during

cooling of the slab and, consequently, can introduce new microcracks in the microstructure or propagate existing cracks.

4.3 NUMERICAL METHOD FOR COOLING SIMULATION

A wide range of cooling process analyses is based on the FEM and finite volume method (FVM) computer simulations. However, researchers [316] focused mainly on the following four basic analyses in their simulations: (a) heat transfer analysis during the cooling process (b) microstructural composition analysis via material properties, which mainly refer to thermal and mechanical properties (c) thermoplastic stress-strain analysis (d) fracture and debonding as well as void nucleation or growth analysis for computation of damage tolerance.

A mathematical model requires three types of formulation to simulate the cooling process of the as-cast steel with austenitic microstructure: the transformation process, cooling rate and elastic-plastic deformation within the microstructure.

The simulation of a cooling process is formulated by the heat transfer governing equations. All the heat transfer mathematical models follow two main steps: first, establish a stress strain relationship based on thermodynamic constitutive laws, and, second, develop a proper method to demonstrate real heat data evolution [237].

A quasi real ANSYS program is developed to simulate the cooling rate through thickness of the sample with boundary conditions the same as those imposed in the experimental process in an ideal case. The level of complexity of the effective factor on cooling rate depends on the number of different phenomena contributing to modifying the microstructure of the steel during cooling from the austenite temperature. Because of these phenomena, such as, phase

transformation, diffusion and impurity segregation, modifying the unit cell and atoms arrangement during phase transformation, localized stresses due to thermal volume changes and many other factors, it is very complicated and costly to have a model for any steel's cooling rate that includes all these effects. Therefore, certain simplifications and assumptions are made to develop an optimum model on the basis of the objective of the simulation.

The FEM model programmed to simulate the cooling rate in this work, computes the thermal gradient of the material and thermal structural contraction caused by temperature drop in the cooling process within acceptable precision with given thermal and mechanical properties. Unlike most of the computer work which calculates the change of phase fraction during simulation, as will be described here, in the present model, the cooling curve-phase transformation data are based on the experimental results from CCT diagrams. Therefore, the numerical model introduced in this dissertation is quasi-real since not only the material properties, geometrical information and boundary conditions are based on the experimental model but also the decomposition of austenite is read from a database provided to the program by the user.

The three types of the controls, transformation control, cooling rate control and thermodynamic strain induced control, are introduced in the next sub-sections, respectively. In the numerical model presented in this work, the inter-granular cracks are simulated by including the properties defined for the grain boundary of the microstructure. This increases the precision of the simulation. However, it causes discontinuity and convergence problems in the mathematical calculation in the code.

4.3.1 Phase transformation control

The fraction of transformation of austenite decomposition to the other phases follows the unity percentage rule;

(%ferrite+ %pearlite+ %bainite+ %martensite+ %austenite+ %other phase)/100=1

(Eq-30)

The incubation time for completion of the decomposition estimated by Scheil's additivity method [262] is shown in Equation 29 below;

$$S = \int_0^t \frac{dt}{\tau_i} \approx \sum_{i=1}^{n} \frac{\Delta t_i}{\tau_i} = 1 \qquad \text{(Eq-31)}$$

Here, Δt_i is the length of ith time step, τ_i is the time for beginning the isothermal transformation at temperature T_i.

The fraction of pearlite transformed from austenite , p(t), at time t, for constant rate of nucleation and growth of the nuclei of the new phase formed from prior austenite, Johnson and Mehl [264] suggested the next relationship in case of the spherical growth of the nuclei;

$$p(t) = 1 - e^{-\pi/3 \dot{N} G^3 t^4} \qquad \text{(Eq-32)}$$

where, dN/dt and G are rate of the nucleation and growth of the nuclei respectively. Borger [261] exploited the additivity rules in Johnson-Mehl relationship through a function $f(t, p(t), T)$ and introduced a Heaviside function to impose the irreversibility of the transformation in the mathematical model for the complete transformation of pearlite and martensite as follows:

For pearlite transformation,

$$p(0) = p_O \qquad \text{(Eq-33)}$$

$$\dot{p}(t) = \begin{cases} 0 \\ f(t, p(t), T)\, H(x) \end{cases} \quad \text{(Eq-34)}$$

For martensite transformation,

$$m(0) = 0 \quad \text{(Eq-35)}$$

$$\dot{m}(t) = f(t, p(t), T)\, H(x) \quad \text{(Eq-36)}$$

where the transformation is prevented above the critical temperature by the next Heaviside function;

$$H(x) = \begin{cases} 1 & x \geq 0 \\ 0 & x \leq 0 \end{cases} \quad \text{(Eq-37)}$$

Then the experimental kinetics of the isothermal phase transformation for ferrite, pearlite, and bainite is given by Johnson-Mehl-Avrami governing equation as ([243]- [245]);

$$V_k = V_y (1 - e^{-b\, t^n}) \quad \text{(Eq-38)}$$

where V_k and V_y are the volume fraction before and after transformation. t is the quenching time, b and n are temperature dependent phase constants. Then Koistimen and Marburger [265] deployed the same method to define the relationship between volume fraction before (V_m) and after (V_n) the martensite transformation as shown in Equation 39;

$$V_m = V_n (1 - e^{-c(M_S - T(t)}) \quad \text{(Eq-39)}$$

where M_S is the martensite start temperature in the CCT diagram and T(t) is the temperature of the material at given time, t. The value of the constant, *c,* is given in the literature as 0.011 [208].

In the models presented in this dissertation, the solid-solid transformation behavior of the unit cell and grain boundaries is formulated in the material properties by Heaviside function. In

the model, the deformation in the elements of the meshing mimics the behavior of the unite cells in the solid-solid phase transformation and the dynamic changes in the structural bodies is consider as representative of the transformation of the grain phases as a result of diffusion and diffusionless atomistic movements in the steel microstructure. The Heaviside function is defined in the definition of the heat expansion coefficient. The definition of the heat expansion coefficient for each phase is based on the experimental data of the CCT diagram for a given steel composition. An approximation of CCT composition for a given steel grade is given with commercial software called JMATPRO. The Heaviside function can be defined by the both instantaneous coefficient of thermal expansion and the secant mean coefficient of thermal expansion depending on the whether the slope of the thermal induced strain versus temperature is defined with respect to a reference temperature or instantaneous temperature. The relation between the instantaneous and secant coefficient of the thermal expansion is given by following expression [312];

$$\alpha^{Sec}(T_n) = \frac{\int_{T_O}^{T_n} \alpha^{ins}(T)dT}{(T_n - T_{\mathrm{Re}f})} \qquad \text{(Eq-40)}$$

Where T_O and T_n are temperatures at which α^{Sec} is evaluated and defined, respectively. $T_{\mathrm{Re}f}$ is the zero thermal strain temperature which in most cases in the calculation is equal to T_O. This variation in the coefficient of thermal expansion is defined by defined temperature at critical points of the Heaviside function. ANSYS defined the values between the defined temperature by a linear function and constant for the temperature below and above the defined temperature range in the table by extreme points of minimum and maximum temperature in the data table,

respectively. A general definition for Heaviside type thermal expansion coefficient function as a function of temperature is given in Figure 19.

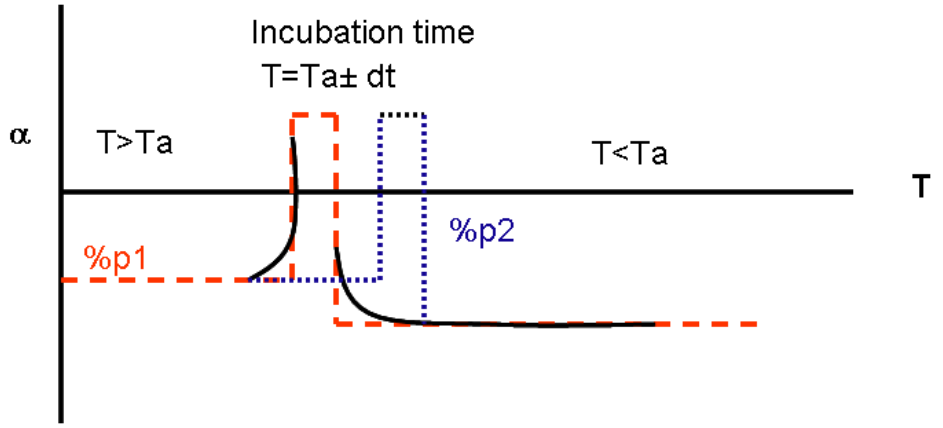

Figure 19 Heaviside function introduced in the definition of the thermal expansion coefficient for specific steel grade to simulate the phase transformation numerically.

The thermodynamic changes and Heaviside function during transformation of the austenite phase to the product of solid-solid phase transformation were embedded in the algorithm of the program via transient phase corresponding for each type of the austenite phase transformation. The transient phase performs the changes in the size of the unit cells in the isothermal condition. The cooling curve in the quasi-real mathematical models given in this dissertation is calculated by a linear function defined between the range of the temperatures known for a given phase fraction. Therefore, instead of estimating the phase fractions with Equations 38 and 39, the actual volume fracture for the phases are embedded in the program as a function of the thermal expansion coefficient. It reduces the estimation error in the calculation. It can also be noticed in Figure 19 that the isothermal solid-solid transformation is considered over a small temperature range rather than at critical temperature. This is required for the convergence condition of the program which results in an ill-function of the equation and it also is a requirement for the incubation time of the transformation.

4.3.2 Cooling rate control

Unfortunately, ANSYS 11.0 does not have a calculation feature for the rate of a parameter. Therefore, the specification of the cooling rate demands special formulation within the simulation. One way to control cooling rate is by imposing boundary conditions in the small time steps and determining the cooling rate of each grain in a post processing calculation. Then the decision for the next step is a function of the temperature and cooling rate computed for the grain. Figure 20 illustrates this method in detail.

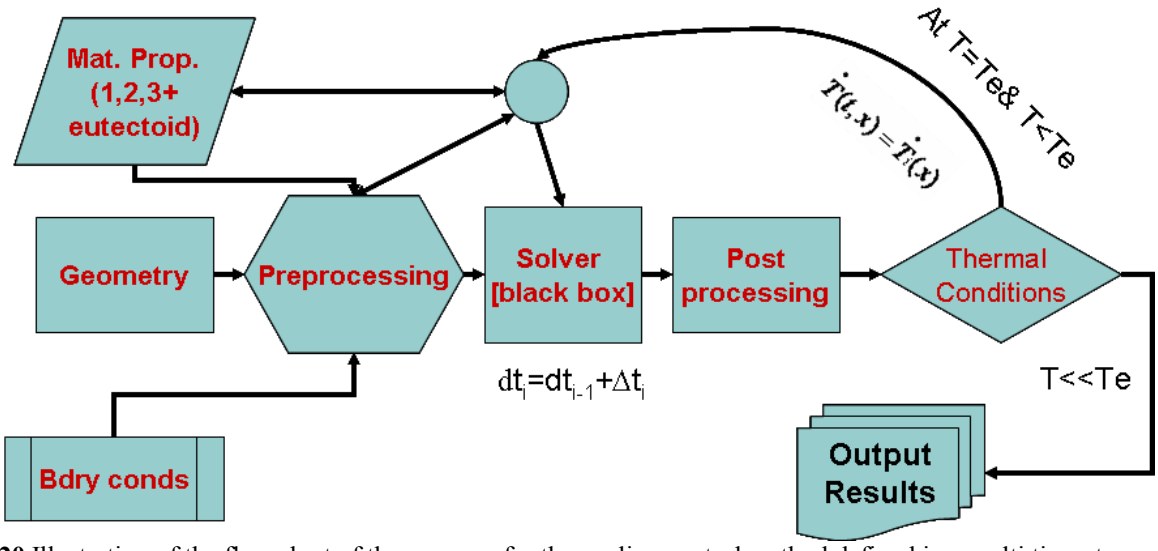

Figure 20 Illustration of the flow chart of the program for the cooling control method defined in a multi time steps.

Preprocessing contains a data base for material properties, a processor to define geometry of the microstructure and predefined process for the boundary conditions. Solver module solves the problem for time step *i*. Post-processing is a decision box which determines the temperature of the grain and the cooling rate. If the cooling rate does not satisfy the simulation requirements, the solution data should be manipulated to fulfill the cooling rate requirements. If the temperature is at the solid-solid phase transformation range, the feedback process changes the

material properties to the corresponding austenite phase transformation products based on the method illustrated in Figure 20. If the temperature is below or above the eutectoid temperature range the program solves the next time step with the material properties defined for the temperature in subcritical, supercritical or intercritical temperature range. The final results are saved in output files for future analysis.

The multi time step process is very cumbersome because of the difficulties to program the feedback bridge and defining suitable solution parameters. It also requires a large amount of the memory of the computer which may cause the program to crash for big size problems. A more efficient solution of controlling the cooling rate is to introduce the cooling rate via the behavior of the thermal properties of the material. A material control rate of heat flux is proposed in the algorithm based on the conductivity equation. The energy generating term in Equation 7 can be ignored in the cooling slab process since no heat is generated because of chemical reactions or internal friction raised by external forces. Therefore, the heat conductivity governing equation is simplified to [226];

$$\nabla^2 T = \frac{1}{\alpha_d} \frac{\partial T}{\partial t} \qquad \text{(Eq-41)}$$

where α_d is thermal diffusivity and equals κ/ρc. above equation can be extended to obtain an exact solution for the heat distribution within the body for heat flux by conduction and convection by deploying a non-dimensionalizing integration method. The variation of density is small because atoms in the solid solution have short range diffusion. Because of the poor heat conductivity of steel, the temperature changes make little deviation in the value of the heat conductivity coefficient. Therefore, density and heat conductivity are considered at two extreme points of the temperature range of the phase appearance during the cooling process. The specific

heat capacity, C, at constant pressure, in J/(mole.K) for molar mass is defined by the next equation [304];

$$C_P = \frac{\delta Q_{rev,P}}{dT_P} \qquad \text{(Eq-42)}$$

The variation of reverse heat transfer, $\delta Q_{rev,P}$, with the temperature gradient is temperature dependent. This can be concluded from the next empirical expression for specific heat capacity [313];

$$C_P(T) = a + bT + cT^{-2} \qquad \text{(Eq-43)}$$

The coefficients a, b and c are material dependent constants measured experimentally at constant pressure condition. Table 4 gives the measured values for a, b and c at one atmosphere pressure and above room temperature for some components in the steel microstructure [313].

Table 4 The coefficient of empirical expression of the specific heat capacity defined for substances in the steel microstructure.

Material	a	b x 10e3	c x 10e-5
Carbon	17.2	4.3	-
Copper	22.6	6.3	-
Iron	14.1	30	-
Alumina	21.9	3.7	-
Silica	15.6	11.4	-

Equations 42 and 43 can be measured for the specific heat capacity at constant volume as well but the value of the specific heat would be less than the one calculated by Equation 42 at constant pressure. ANSYS evaluates with the same method described for the thermal expansion

coefficient for the whole range of the temperature in the simulation. If the divergence of the gradient of temperature (Laplacian of T) between adjacent points is small enough in which in the computation can be assumed to be constant, then the value of the specific heat capacity has a direct relationship to the rate of the changes in the temperature or, in other words, the cooling rate. This is the case where the thermal conductivity of material is high enough to establish such a low thermal gradient within the material. Figure 21 shows the relationship between the thermal expansion coefficient and the cooling rate.

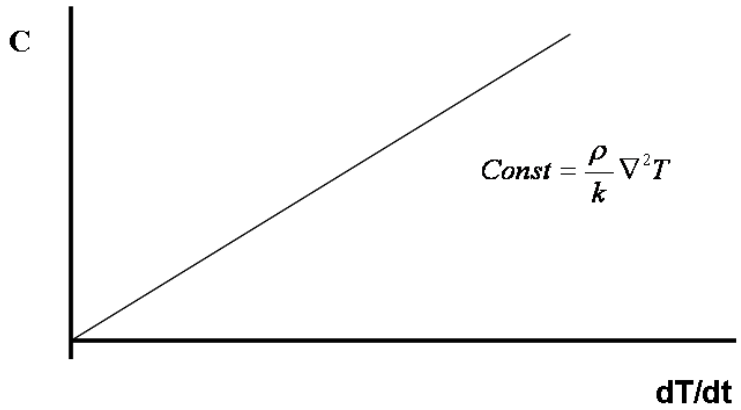

Figure 21 The specific heat capacity of the steel can determine the value of the cooling rate through a direct relationship in the numerical calculation.

Although another table can be managed for each of material properties as well, in many cases constant value can be considered for the density and the thermal conductivity coefficient of the steel except where increased accuracy of the computation is required. The general case is to consider the convection heat coefficient of the film of the cooling agent at the vicinity of the surfaces where the heat flux leaves the bulk material. This case is more realistic since the cooling rate in the laboratory experiments and industrial applications is controlled by the material properties of the cooling agent. The trigger of heat flux is the temperature difference between the cooling agent and the hot steel. Although thermal conduction processes such as formation of gas

and vacuum at the surface of solid with fluid may affect the transient condition of the heat transfer [294]. The governing equation for general heat transfer can be derived by plugging Equations 1, 2, 3 and 7 into the equation of balance of volumetric energy. This gives the following nonlinear, first order, non-homogenous, ordinary differential equation [294];

$$[h(T_W - T_\infty) - \varepsilon\sigma\,(T_1^4 - T_2^4)]A + \dot{q} = -\rho V c\dot{T} \qquad \text{(Eq-44)}$$

Parameters A, V are the surface and volume of the body. The exact solution for the above equation does not exist unless some simplifications are applied on the equation. But the FEM solution can approximate the solution with acceptable accuracy. Note that in the as-cast slab cooling the term heat generating is zero. The cooling rate is defined in the equation by defining parameters h, ε, ρ, and c. To increase the accuracy of the FEM approximation, the volume and surface of the as-cast steel are calculated as a function of temperature using Equations 5 and 6, respectively. Equation 43 gives the temperature dependent value of heat capacity. Hence the effect of cooling agent on cooling rate is controlled by the film convection coefficient, h, whose value can be constant or a function of non-steady process (e.g. bubble formation for different temperature gradient at convection surface).

4.3.3 Thermodynamic strain induced control

Cooling steel slabs from the austenite temperature creates both strain induced due to thermodynamic effects on the microstructure and solid to solid phase transformation phenomena resulting from formation of other phases (ferrite, bainite, martensite,….) from the austenite phase. The strain developed in the microstructure may result in increasing the density of cracks and flaws in which they are modeled by fracture constitutive laws.

The thermal induced strain exists because of the heat flux out of the body and calculated as a function of secant coefficient of the thermal expansion, as below [312];

$$\varepsilon^{TH}(T) = \alpha^{\sec}(T)(T - T_{REF}) \quad \text{(Eq-45)}$$

By replacing the equivalent value for $\alpha^{\sec}$ with α^{ins}, the thermal strain can be calculated from the instantaneous coefficient of the thermal expansion, as well. The isothermal phase transformation imposes dynamic induced strain due to displacement of the atoms in the modification of unit cell arrangement and volume from FCC to BCC or BCT structure, described in Figure 16 and Figure 17. The dynamic for small displacement is defined by Lagrangian strain [314];

$$\varepsilon_{ij} = u_{i,j} + u_{j,i} \quad \text{(Eq-46)}$$

where *i* and j=1,2,3 and show the direction in the x, y or z in the Cartesian coordinate system, respectively. Then the stress strain relationship is [314];

$$\sigma_{ij} = C_{ijkl}\varepsilon_{kl} \quad \text{(Eq-47)}$$

where the value for C_{ijkl} (i, j, k, l=1, 2, 3) for the isotropic material is given by [315];

$$C_{ijkl} = \lambda\delta_{ij}\delta_{kl} + 2\mu\delta_{ik}\delta_{jl} \quad \text{(Eq-48)}$$

δ is a symbol for Kronecker delta function and defined as;

$$\delta_{ij} = \begin{cases} 1, & if\ i = j \\ 0, & if\ i \neq j \end{cases} \quad \text{(Eq-49)}$$

λ and μ are known as Lame constants and are given by following equations, respectively [314],[315]);

$$\lambda = \frac{\nu E}{(1+\nu)(1-2\nu)} \quad \text{(Eq-50)}$$

$$\mu = \frac{E}{2(1+\nu)} \tag{Eq-51}$$

Here E and ν are Young's modulus and poisson's ratio of the material, respectively. The plastic deformation stress and strain are given by the equivalent Von Mises stress. The Von Mises stress and yielding relationship is [314];

$$Y = \sqrt{\frac{3}{2} S_{ij} S_{ij}} \tag{Eq-52}$$

where S_{ij} is deviatoric stress and is equal to;

$$S_{ij} = \sigma_{ij} - \frac{\sigma_{kk}}{3} \delta_{ij} \tag{Eq-53}$$

ANSYS provides the output Von Mises or equivalent and strain of Equations 47 and 53 by the next relationship [312];

$$\varepsilon_e = \frac{1}{1+\upsilon'} (\frac{1}{2}[(\varepsilon_x - \varepsilon_y)^2 + (\varepsilon_y - \varepsilon_z)^2 + (\varepsilon_z - \varepsilon_x)^2])^{1/2} \tag{Eq-54}$$

where ν'is material poisson's ratio for elastic and thermal strain and 0.5 for plastic and creep strains. Equivalent Von Misses stress is [312];

$$\sigma_e = (\frac{1}{2}[(\sigma_x - \sigma_y)^2 + (\sigma_y - \sigma_z)^2 + (\sigma_z - \sigma_x)^2 + 6(\sigma_{xy}^2 + \sigma_{yz}^2 + \sigma_{xz}^2])^{1/2} \tag{Eq-55}$$

The Heaviside thermal expansion coefficient method imposes the dynamic isothermal strain by defining the thermal expansion coefficient deploying the method described in Figure 19. Therefore, the displacement defined in Equation 54 is not only a function of position but also depends on the temperature. The thermal and elastic dynamic strains are coupled as next [317]:

$$\varepsilon_{ij} = D_{ij}^{-1} \sigma_{ij} - \alpha \Delta T \tag{Eq-56}$$

The FEM matrix equation is calculated by applying variation principal to stress equation of motion obtained from Eq. 56 and to heat flow conservation equation coupled by the thermoelastic constitutive equations. Therefore the FEM matrix equation has a form of following:

$$\begin{bmatrix} [M] & [0] \\ [0] & [0] \end{bmatrix} \begin{Bmatrix} \{\ddot{u}\} \\ \{\ddot{T}\} \end{Bmatrix} + \begin{bmatrix} [C] & [0] \\ [C^{tu}] & [C^{t}] \end{bmatrix} \begin{Bmatrix} \{\dot{u}\} \\ \{\dot{T}\} \end{Bmatrix} + \begin{bmatrix} [K] & [K^{tu}] \\ [0] & [K^{t}] \end{bmatrix} \begin{Bmatrix} \{u\} \\ \{T\} \end{Bmatrix} = \begin{Bmatrix} \{F\} \\ \{Q\} \end{Bmatrix} \qquad \text{(Eq-57)}$$

Where:

[M] = element mass matrix= $\rho \int_V [N]^T [N] dV$

[C] = element structural damping matrix= 0

[K] = element stiffness matrix= $\int_V [B]^T [D] [B] dV$

{u} = displacement vector

{F} = sum of the element nodal force

[C^t] = element specific heat matrix= $\rho \int_V c\, [N]^T [N] dV$

[K^t] = element diffusion conductivity matrix= $\int_V [B]^T [D] [B] dV$

{T} = temperature vector

{Q} = element convection surface heat flow vectors

$$= \rho \int_{S_M} T_B h_f \, [N]^T [N] \, dS_{msurface\ of\ the\ \mathrm{model}}$$

[B] = strain-displacement matrix

[C^{tu}] = element thermoelastic damping matrix = $-T_0[K^{ut}]^T$

[K^{tu}] =element thermoelastic stiffness matrix = $\int_V [B]^T \{\beta\} \left(\nabla \{N\}^T\right) dV$

h_f = film coefficient

T_S = temperature at surface of model

T_B = bulk temperature of the adjacent fluid

N is the shape function, β and c are given by Eq. 14 and Eq. 43, respectively. The radiation is superimposed to the solution by radiation of the surface to a point defined by Eq.3.

5.0 SPECIFYING ANOMALIES CHARACTERIZATION USING THE ULTRASONIC NDT METHOD

5.1 EXPERIMENTAL PROCEDURE

The ultrasonic NDT image can be processed and analyzed to give qualitative characterization of the anomalies in the continuously cast steel. The ultrasonic sensor and its compatible software provide information regarding the anomalies' distribution, location and density. The defects' information provided by NDT assists to promote the analysis of experimental cooling tests results and numerical cooling simulations. In this research work, an extension of ultrasonic NDT image processing and analysis is introduced to identify the type and location of the anomalies in the ultrasonic NDT image. An image processor processed the ultrasonic images and the collected data were analyzed using the Excel macro program. A classification criterion was defined on the basis of size and shape of images of anomalies captured by ultrasonic NDT at zero degrees with respect to the top surface. DT methods were implemented on samples of all different combinations of steel grade with its original location in the cast slab and cooling method to correlate between analyzed NDT images of the defects and type of the anomaly.

In this project, ultrasonic NDT and direct microstructural analysis based on the NDT results were conducted on 24 samples of the three grades of steel 1010*, 1091* and 1319*. Appendix A shows the geometrical and casting information of the sample slabs used in this

dissertation. The samples were cut from four different locations from the as-received steel slabs. The slabs having thicknesses of 175 mm to 230 mm were grouped in two sets based on their cooling conditions provided by the steel company supporting this work. The slab samples were either air cooled or cooled in a cooling chamber to room temperature. The temperature at which the slabs were introduced in the chamber was between 570 ^{o}C and 550 ^{o}C. Therefore, the slabs entered the cooling chamber at subcritical temperatures after the decomposition of austenite to either high or low temperature products.

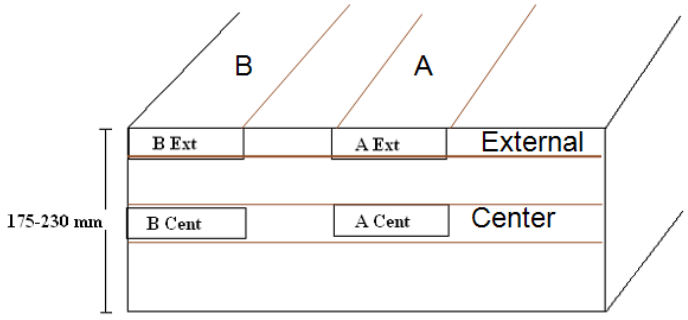

Figure 22 The schematic location of the slab samples.

Figure 22 shows a schematic of the location of the four (4) samples per each steel composition and cooling condition available for this research work. The sample slabs were cut from cast slab in 178 mm wide 254 mm long 51 mm thick. After each sample was cut, it was labeled with a nine-digit number and a series of four to five letters in the upper right hand corner (See Figure 23). The first six numbers identified the cast number of the steel and the actual steel grade. The next three numbers identified the cooling rate applied to the original cast slab. The first letter of the series identified the column the sample was taken from and the last three or four letters identified the row the sample was taken from.

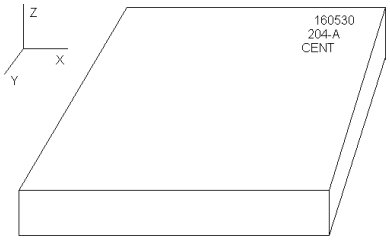

Figure 23 Schematic representation of the position of the samples designation number.

In ultrasonic NDT test techniques, ultrasonic signal waves are emitted from a sensor made up of a transducer, which are mainly piezoelectric, and a receiver. Parts of the emitted waves are reflected off the samples by surfaces of anomalies to the transducer or other electronic receivers and other portions of waves are scattered and damped into the texture. The schematic view of the ultrasonic mechanism can be seen in Figure 24.

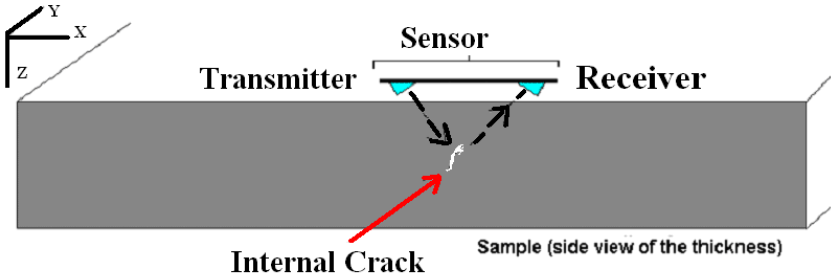

Figure 24 Function of sensor in indicating defects in the slab.

The magnitude of the initial input pulse and captured reflected signals are compared by an oscilloscope, or a collecting and compiling signal software. The ultrasonic tests were carried on in a bath filled with 160 liters of water to minimize the undesired sound waves from environments and working place or testing tools and equipment that may change the image of the results. An image of the ultrasonic machine is shown in Figure 25. Sonics is a DOS software package used for this purpose in these tests.

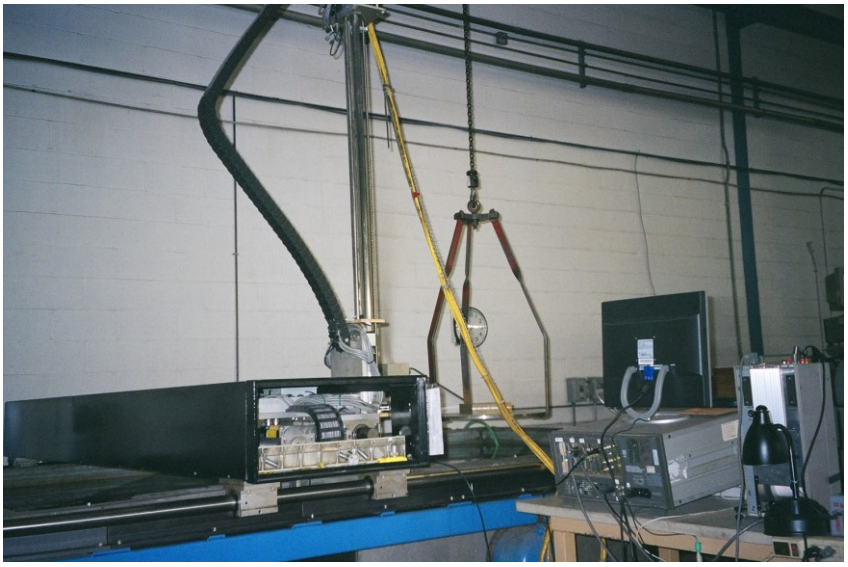

Figure 25 Set up of the ultrasonic machine.

Table 5 Sensor specification detail.

Specification	Model	Specification	Model
Water Gap	160 mm	Working Range	2.5-100 mm
Sensor Type	Focused	Near Surface Resolution	2.5 mm using .25 F.B.H.
Nominal Diameter	19 mm	Test Beam Diameter	23 mm using .25 F>B>H
Nominal Frequency	5 MHz	Max Scanning Speed	457 mmn/sec using 400 prf
Voltage	High	Material Velocity/Material Cal	5.87 mm/sec
Damping	50 Ω	Beam Width	2.5 mm
Frequency	5 MHz	Beam Overlap	1 mm
Filter	Off	Measured Frequency	50 MHz
“N” Distance	160 mm	“Nh” Distance	7.5 mm

Scattering in the energy of the waves traveled through the sample because of the obstacles in waves' path, gives information about the anomalies. The sensor was moving with a constant speed and scanning the surface of the sample. An overlapping of scanning was considered to remove the uncertainty of the signals received from the edges of the width of the scanning beam band. Accuracy of the images and speed of scanning depends on the sensitivity of the sensor.

In this work, the sensor was fixed 152.4 mm above the sample at 90 degree with respect to the parallel sample surface with the x-y plane of the scanning coordinate system. A cylindrical probe was attached to the stamped side of the slab to ease tracing of the position of defects over the sample. The sensor was a focused type TLC model with nominal frequency of 5 MHz. The resolution of the sensor for the near surface is 2.54 mm with overlapping of 1 mm. Of course, higher resolution and overlapping may result in higher accuracy and sharper edges. Table 5 is the specification of the sensor used in the ultrasonic tests.

Figure 26 Standard gages to calibrate the sensor for the bottom surface of the tested sample.

The sensor was calibrated for the thickness of the sample before test to detect the bottom surface of the tested sample and to filter returned waves from sources deeper than the bottom

surface. Figure 26 gives the picture of the standard gages used to calibrate the sensor. The signals received to the specific point of the transmitter of the sensor correspond to a point in the surface of the sample. The amplitude of these signals is the strongest reflected signal through the thickness for a point on the x-y plane. The sensor used in these tests was calibrated for 10 percent background noise. As the thickness of the test sample increases, there is a possibility of interference between returned waves from a point within the sample to the sensor's receiver and waves reflected from odd angles of other anomalies located in other points in the slab. These interactions of sound waves could result in resonance phenomena, amplifying the reflected waves, and raising the analyzing error. To minimize these errors, the control software was set to generate imaginary sections through the thickness by arranging a decibel range filter through the slab's thickness. Each of these imaginary sections is called a gate. In fact, Sonics filtered the entire signals out of the range of the gate with inverse functions between the gate number and decibel energy of the sound wave to be filtered such that the deeper gate has a smaller decibel range sound wave. The data captured for each point by the receiver is collective data for the total thickness of the gate.

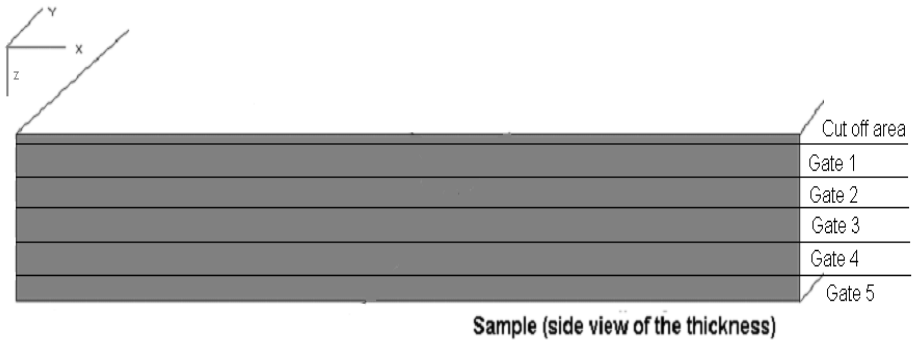

Figure 27 Illustration of the gates in the ultrasonic test.

The software collects the amplitude signal within the gate range thickness for each point of the sample's surface. The number of gates used in the ultrasonic test depends on the material and thickness of the sample, purpose of the test, estimated density and properties of the object to be detected in the sample and budget parameters with obvious relationship as more gates make the tests more expensive but more accurate, as well. Sonics can generate up to eight sections, however, five gates were considered for the tests. To avoid losing any information of defects through entire thickness of the slab, an overlap range between adjacent gates was considered. Figure 27 illustrates the gates in the ultrasonic test. Sonics discarded the signals returned from an interface layer of the top surface to eliminate the effect of the surface roughness in the processed results. The thickness of the interface layer depends on the surface roughness of the top surface of the test sample. The receiver collects the amplitude of signals from each point of the surface according to its resolution and overlapping portion of band. Sonics compiled these signals and construct the image of the reflected amplitude (RA) on an absorbed energy map of the surface within the range of the gate's thickness. A feedback between transmitter and receiver gives the travel duration for the signal from emitting moment until the receiver captures its reflected portion. This time is called time of flight (TOF) and is converted to an image map of the surface for each gate. TOF technique has been used in other application as well [131].

The Sonic software provides the numerical percentage value for RA and TOF in color spectrum maps. The standard gage calibrates the color spectrum to present the lowest energy absorbed region in the RA map or longest TOF for the signals reflected from the bottom surface of each gate in the TOF map by blue. The regions colored other than blue are locations in the slab with possible existence of defects. The x-y coordinates of the areas flagged as the defects are given by image processing software with the commercial name of Scion. An Excel database

with embedded macro is designed to process the data extracted from Scion. DT methods were implemented on small samples cut from regions in the test slab suspected of having a defect type of slab sample for further investigation leading to information about the type of the defect.

A portion of the slab containing a defect was cut by a band saw and a circular saw. The cut portion was selected on the basis of computational and image analysis prior to microstructural analysis. The area of the cut that would expose the defect or anomaly was always moved ahead of the center of the anomaly by 5 mm. This was done to compensate for material lost by the saw blade (<1.5 mm) and to add room for area lost during the grinding and polishing stages. After a sample containing the anomaly was cut out of a slab, it was mounted in a thermosetting polymer to be ground and polished. Each sample was ground starting with 180, then to 240, to 320, to 400, and finally at 600 grit sandpaper. Special care is taken to avoid corrosion over the surface of these samples before examining the sample using standard optical microscopy (OM) and scanning electron microscopy (SEM)

5.2 LOCATING THE 3-D POSITION OF THE DEFECT

The colored regions were classified on the basis of their size and shape by an Excel macro, the criteria used in this classification is summarized in Table 6. The Excel macro properly sorted and grouped the anomalies based on location, shape and size. The macro counts the number of anomalies for each sample and gives them an ID built by combination of two characters. The first character referred to their size and the second corresponded to their shape. The criteria used in this classification are summarized in Table 6. The Excel macro properly sorted and grouped the anomalies based on location, shape and size.

The Excel macro also estimates the possible relationship between anomalies in different gates. The macro counts the number of anomalies for each sample and gives them an identification (ID) number built by combination of two characters. The first character referred to their size and the second corresponded to round (R) and elongated (L) shapes.

Table 6 Classification criteria for anomalies recognized in the TOF image map.

size ID	mm^2	size ID	mm^2
1	small, only a point	5	<96.8
2	<4.5	6	<161.3
3	<10.0	7	<322.6
4	<40.3		

The definition of a defect or anomaly in NDT tests is based on two criteria. The first criterion is the percentage of return amplitude in the TOF map induced from the fact that signals returned faster than those from the bottom of the gate must be reflected from a surface above the bottom surface, such as the edges of a void and cracks or surface of an obstacle (e. g. inclusions). TOF signals with 20% less than signals received from the bottom of the gate were considered as possible regions with an anomaly. This TOF limit was set according to the sensitivity of the sensor, possible effect of background noises, and rigidity of the ultrasonic. The second criterion for a region with the anomalies in TOF map is any region with size class equal or greater than size four, which is a region larger than 40 mm^2. It was set based on the scanning resolution limitation of the sensor and edge effect in scanning of an anomaly.

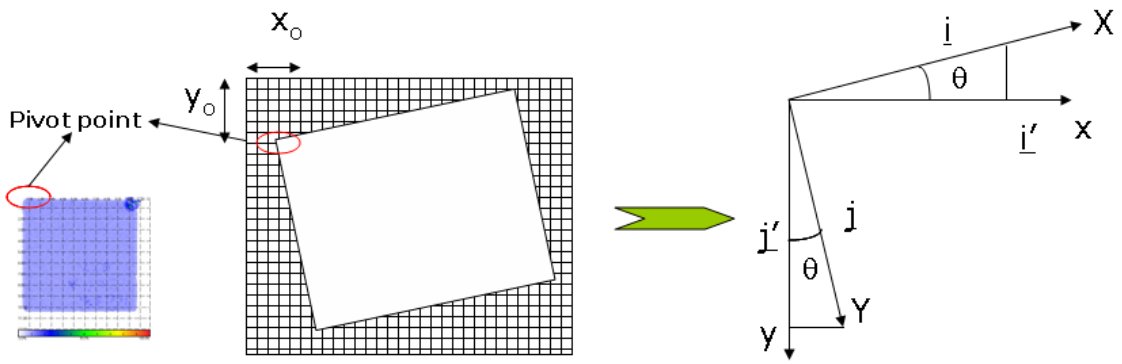

Figure 28 Screen rotation of Scion axis in direction of Sonics axis

Since the images of the slabs did not exactly match, the image plane of the Scion screen should be rotated toward the Sonics screen to find the real position of the anomaly on the slab. Figure 28 demonstrates the screen transformation between image of the TOF map and Scion coordinate system. The vector rotation of the axis were calculated using the following equations,

$$\begin{aligned} i' &= i\cos\theta; \quad & j' &= -i\sin\theta \\ i' &= j\sin\theta; \quad & j' &= j\cos\theta \end{aligned} \qquad \text{(Eq-58)}$$

Then the position of a point in the slab using Sonics coordinate system can be computed by transformation and translation of the Scion axis by the following equations:

$$X = {}^{CF}\!/_{SF}\left[x\times\cos(\theta) - y\times\sin(\theta) - x_o\right] \qquad \text{(Eq-59)}$$

$$Y = {}^{CF}\!/_{SF}\left[x\times\cos(\theta) + y\times\sin(\theta) - y_o\right] \qquad \text{(Eq-60)}$$

in which X and Y are image coordinates in the slab and x and y are image coordinates in Scion. Correction factor (CF) is for deviation between real position and image of the maps due to limitations in sensitivities of the sensor. SF is Scaling factor (=|x|/|X|) which has units of pixel per unit length and Θ is the angle between object and image coordinate systems. x_o and y_o are translation distances between two coordinate systems after rotation in the X and Y directions, respectively. To cut the portion of the sample that contains the anomaly, in addition to the plane

coordinate of the anomaly on the x-y axis, the height of the top surface of the anomaly from the top surface of slab should also be determined. This gives the z coordinate of the anomaly in a 3-dimensional Cartesian coordinate system. The origin of the coordinate system is at the top surface corner side of the slab and the z-coordinate refers to the distance of the anomaly's location from the top surface. The Excel macro uses the next computation to locate the z-coordinate of each anomaly both for the z-coordinate of each gate and z-coordinate for the slab;

$$t_g^i = v_s \times \Delta t_i^g \quad \text{(Eq-61)}$$

$$t_i^g = \Delta t_i^g \times \frac{\%TOF}{100} \quad \text{(Eq-62)}$$

$$z' = v_s \times t_i^g / 2 \quad \text{(Eq-63)}$$

$$z_i = z_i' + t_{total}^i \quad \text{(Eq-64)}$$

in which v_s is the average speed of the sound in the steel media and Δt_i^g is the time range defining the signals filtered for a specific gate. %TOF is the time of the flight in percentage. z_i' and t_g^i are distances of the anomaly from the top surface and the thickness of the i-th gate, respectively. t_{total}^i is the total thickness of the slab between the top surface of the i-th gate and top surface of the slab. z_i is the distance of the anomaly in the i-th gate from top surface of the slab.

5.3 INVESTIGATION OF DEFECT TYPE

Using the image coordinate system, the matching point for the TOF map in the RA map can be found. The color intensity function was used again to find the energy lost/absorption over the anomaly. The following equations are used to characterize the anomalies based on RA;

$$\%A = \frac{A_S}{220} \times 100 \quad \text{(Eq-65)}$$

$$A = \%A \times \left(\frac{80}{100} \right) \quad \text{(Eq-66)}$$

$$A_A = -20 \times \log\left(\frac{A}{80} \right) \quad \text{(Eq-67)}$$

Where A and %A are the amplitude factor and the returned amplitude percent, and A_S and A_A are returned amplitude on image processing software and absorbed amplitude, respectively. Since 20% of RA was filtered, 80%RA had 100% value in the RA map and Eq. 66 correlated the RA values to find the actual amplitude factor. These computational values along with RA and TOF maps provide analytical techniques to locate the approximate location and size of the anomaly. Figure 29 is an example of RA and TOF maps of the gate of a scanned sample.

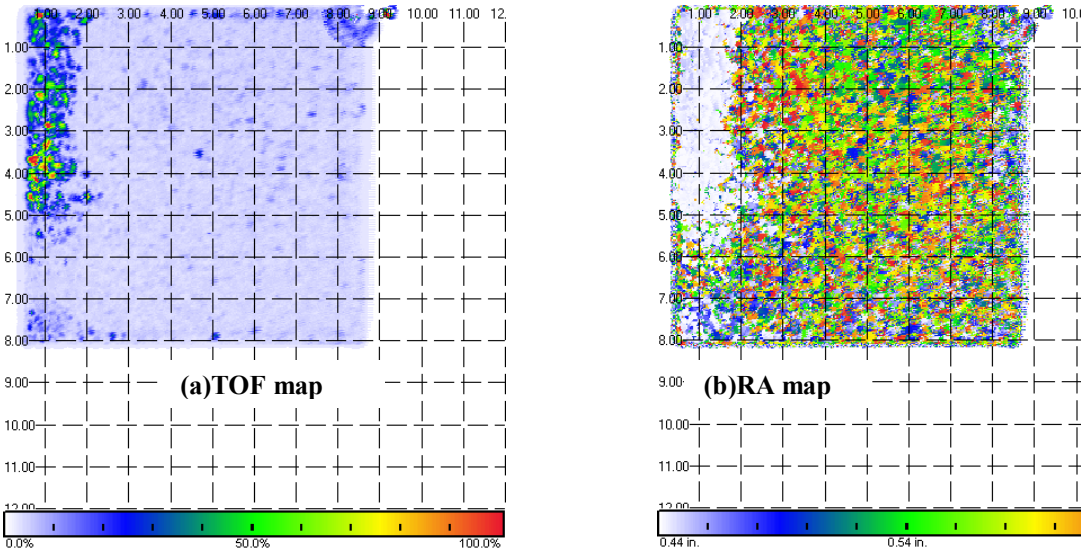

Figure 29 RA and TOF maps constructed by the ultrasonic test, (a)TOF map (b)RA map.

It can be noticed that RA looks like the negative image of the TOF map. The scattering of different colors on the RA map shows the sensitivity of the absorption of energy by different factors. This scattering may result from different levels of absorption or diffraction of sound

energy by grain and grain boundary of different phases. The RA map is also more sensitive to image overlapping through thickness. These facts prevent extraction of useful results from the RA map. Therefore, further analysis or characterization of the anomalies was based only on the TOF map. One to one correspondence between the TOF percentage and type of anomaly is accomplished by direct observation of the anomaly's type and comparison with TOF percentage and defect area on the map. The correction factors used in the equations that provided the location of anomalies were calibrated after several samples were cut from the test slabs by precise measurement on the actual coordinate system on the slabs and careful and systematic measurements of the material removal during the sample preparation for microstructural analysis.

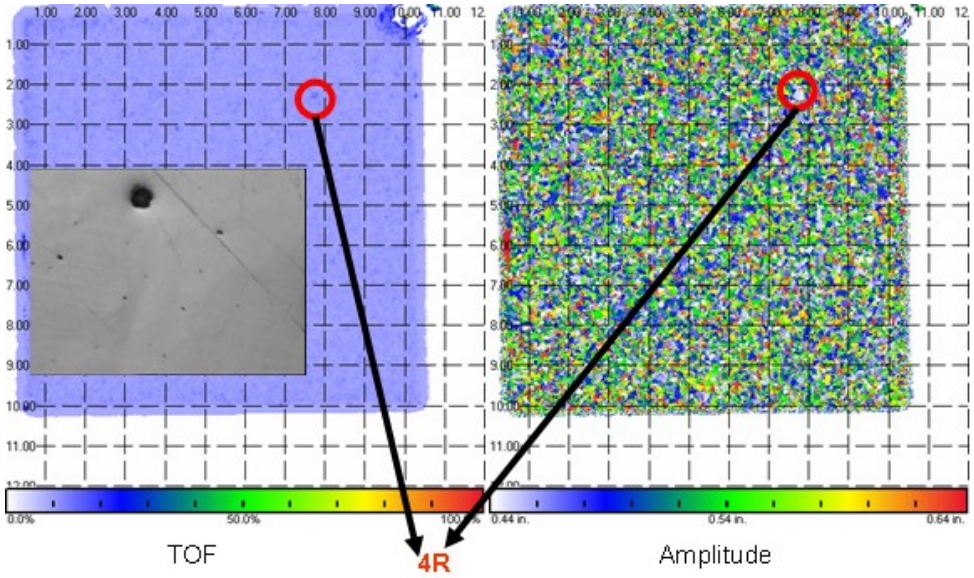

Figure 30 Analyzing RA and TOF maps using a microscopic image of an anomaly in 160530-204-B-EX.

The experimental and analysis procedures were applied on several samples from slabs of different grades and both cooling conditions. The regions of the NDT samples were chosen based on the information furnished by Excel macro and TOF maps. This information indicated

the samples containing defects with different shape, size and, more importantly, TOF percentage value. These series of tests provide a correlation between the type of an anomaly and TOF percentage range. Figure 30 is an example of the correlation between the picture taken from an anomaly and its RA and TOF result.

Investigation information of these tests for each grade of steels, are given in Figure 31, Figure 32 and Figure 33. These are examples for identification of grades 1319*, 1091* and 1010* for cracks, voids and inclusions, respectively.

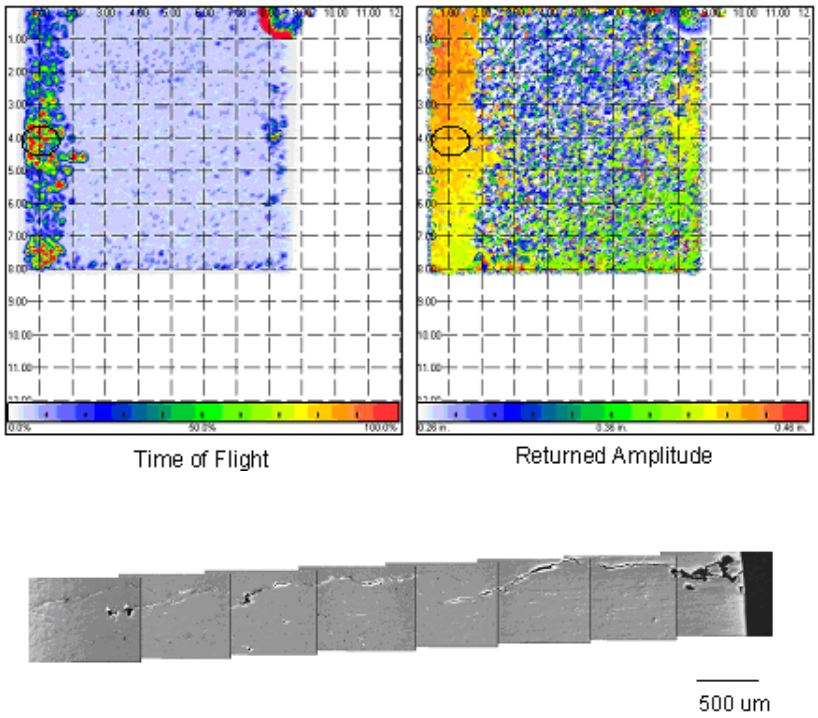

Figure 31 Image processing data related to anomaly 260191-502B-CENT-G2-1 within air-cooled slab sample of 1319* grade steel: TOF%=95.5; RA%=66.8; anomaly type: 8L, defect type: Crack.

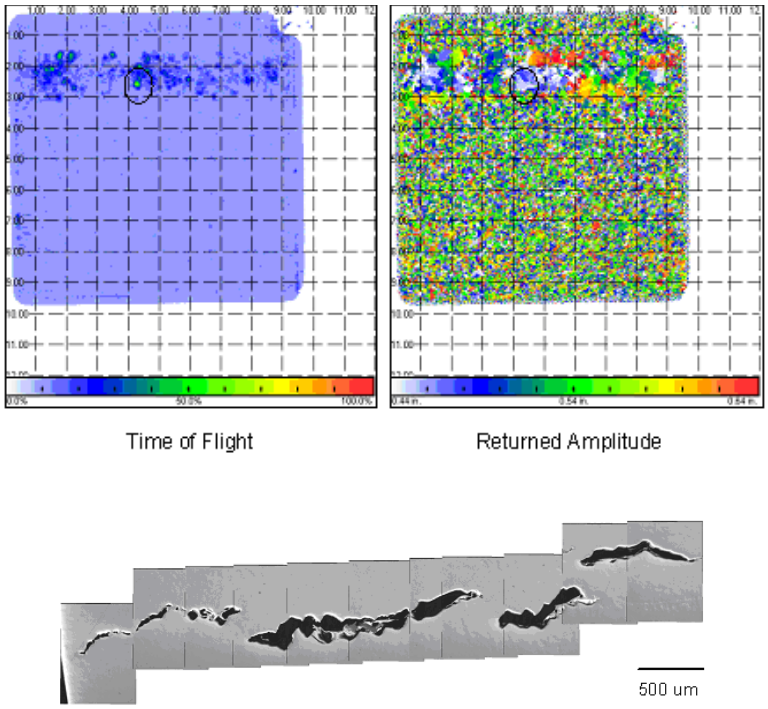

Figure 32 Image processing data related to anomaly 554754-103A-CENT-G3-7 within air-cooled slab sample of 1091* grade steel: TOF%=59.1; RA%=19.55, anomaly type: 6R, defect type: Elongated Void.

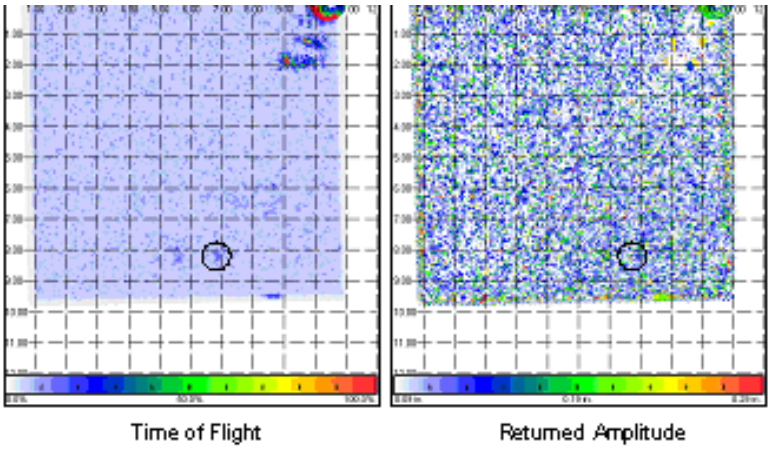

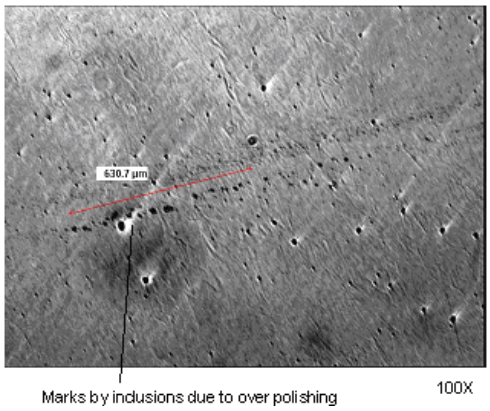

Figure 33 Image processing data related to anomaly 160530-204B-Ext-G1-24 within air-cooled slab sample of 1091* grade steel: TOF%=30; RA%=40, anomaly type: 5L, defect type: Chain of MnS inclusions.

As it can be seen in the examples presented in the Figure 31, Figure 32 and Figure 33, each particular defect in the samples has a specific TOF range value. Based on systematic microstructural analysis, defects with a TOF value between 20% and 60% were observed to be related to voids or inclusions (or a combination of the two). Cracks had a larger TOF, ranging from 60% to 100%. It is important to note that voids also had a wider TOF range from 40% to 95%, than the other defects observed. Hence, there is an overlapping of the ranges of both inclusions and cracks. Due to this, an additional size correlation parameter was added to help distinguish between the three possible defects. Inclusions size in the NDT images were small and did not range above 9 mm^2. Voids had a larger size, with a range of 4 to 96 mm^2 for single voids and larger than 324 mm^2 for multiple or collections of voids. Cracks were always the largest anomalies in the NDT tests, a single crack being 36 mm^2 or larger and collections of cracks being larger than 324 mm^2 (second criteria of anomaly's definition for these tests).

The DT tests were used as decoding tool to find the range of TOF map for identifying the type of defect. Figure 34 is the result of these tests in order to develop a relationship between the range of TOF map and type of defect. From Figure 34 it can be concluded that cracks have a higher TOF which is possibly because of space formation between two faces of the cracks.

Inclusions generally provide a denser and tougher media compared to the steel surface for the sound waves and so it decreases the travel time of the waves inside the slab. It is found that voids can have any TOF percentage since voids have different shape, size, formation sources and density per unit volume and accumulated structure in the slab. Despite that, waves reflected from the upper surface of the voids can result in confusion between voids and inclusions. However, voids can almost be distinguished from the cracks by their shape in the TOF map. All these make TOF related to the voids dominant over almost the entire range of the defect's TOF range.

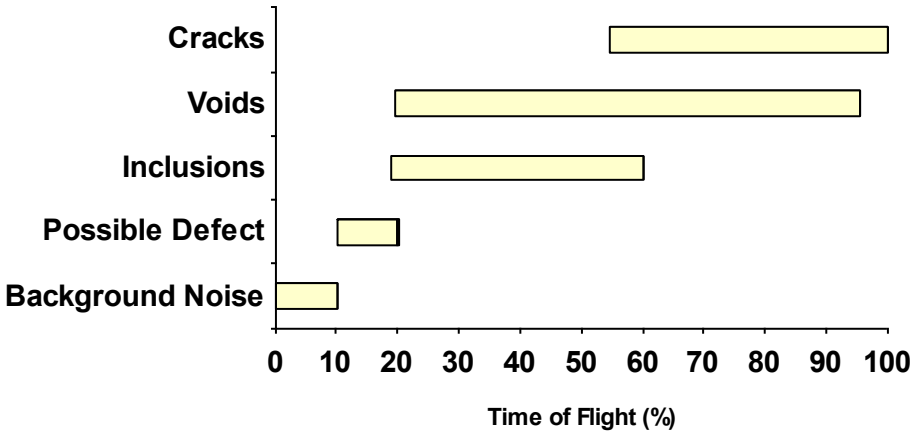

Figure 34: Identification TOF percentages range for the type of the defect in the slabs.

5.4 INVESTIGATION OF DEFECT TYPE

Figure 35 helps to determine the anomalies in the tested slabs based on their cut location from the slab quantitatively and qualitatively. This gives information about spatial distribution of voids, cracks and inclusions in the cast slab. These re-examining of the TOF maps of all sample slabs are summarized in Figure 35. The re-examinations are performed automatically by the

Excel macro. The location of the inclusions was in agreement with their formation mechanism. Typical examples of causes for microstructure anomalies were found to be large groups of closely packed non-metallic inclusions (Al_2O_3, or MnS), abnormally large non-metallic inclusions, and microstructural voids.

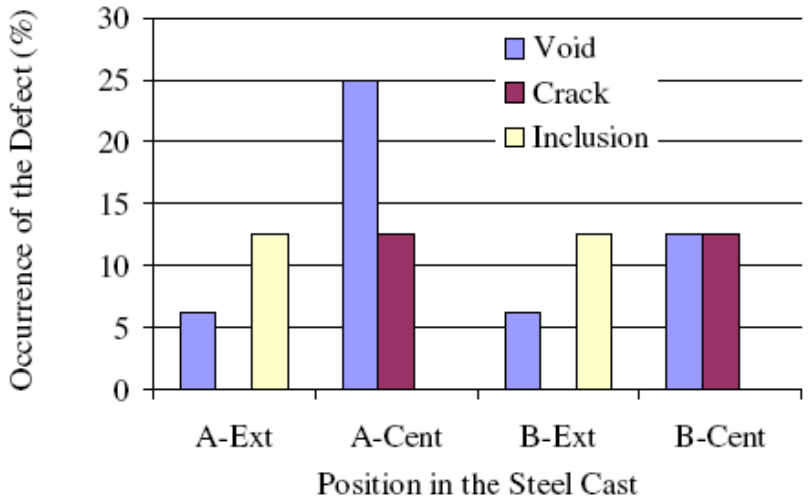

Figure 35 Spatial distribution of defects in cast slab.

The location of the occurrence of inclusions shown in Figure 35 was found to be near and away from the surface of the slabs. A recurring trend in all the steel grades was that the A-Cent sample contained more defects than the other three slabs from each cast. Another trend was that while the A-Cent samples contained the highest number of defects, the B-Cent samples contained the largest defects of the slabs. These observations are most likely the cause of the interactions between the thermal gradients associated with the cooling zones in the slabs themselves. Excel macro also can be used to re-analyze all images of TOF maps for type and density of the defects on the basis of grade of steels.

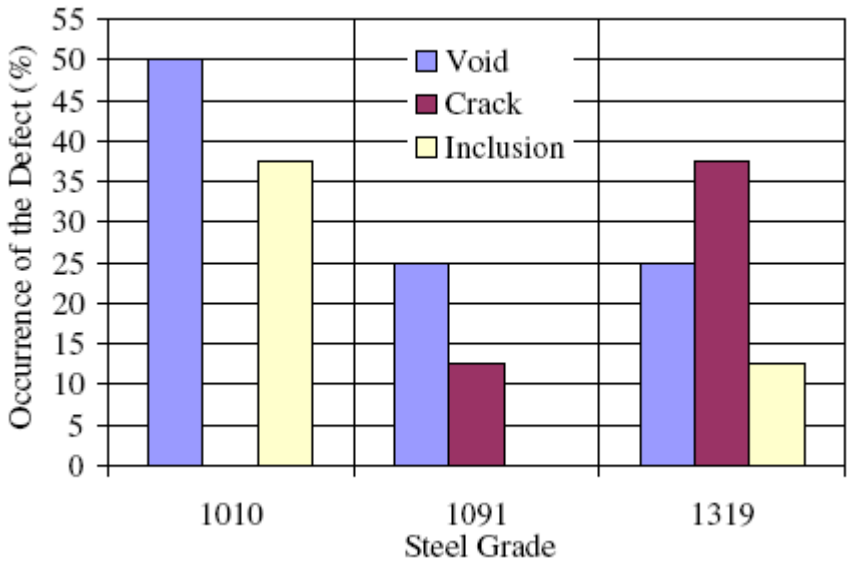

Figure 36 The density of different type of anomaly in the sample slabs on the base of their grade.

Figure 36 presents the results of this re-analysis. It can be concluded from this figure that cracks seem to occur in the higher alloyed steels, i.e. 1091* and 1319*. Figure 36 also shows that 1010* steel has a larger number of voids and inclusions than the other steel grades studied in this investigation.

6.0 EFFECT OF INCLUSIONS IN CONTINUOUSLY CAST STEEL MICROSTRUCTURE DURING COOLING

6.1 CRACK FORMATION AROUND AN INCLUSION

Hot solidified steel continues to move forward by rollers in the direction of the continuous casting as it is cooling with a specific cooling rate. The rollers exert compression forces over the upper and lower surfaces of the strand by dragging the slab in the casting direction. On the other hand, the cooling of hot steel sets up thermal gradients through the thickness of each section and along the cast direction of the strand. The thermal difference along the length of the strand is usually small compared to the thermal gradient through the thickness. The external mechanical forces and internal thermal forces introduce residual forces within the microstructure. How the nonmetallic inclusions react in response to these residual stresses depends on steel chemical compositions, type, size, density, volume fracture, morphology and distribution of the inclusions in the texture [318]. Concentration of thermodynamic forces around inclusions causes deformation of inclusions and/or microcracks in the texture around the inclusion. Interaction between non-metallic inclusions and matrix material located in a stress field may result in the formation of microcracks or voids. Some non-metallic inclusions such as TiN, Al_2O_3, SiO_2, (Fe, Mn) S and CaO increase the stress concentration by decreasing the modulus of elasticity of the

inclusions [319]. Faceting of non-metallic inclusions affects the stress concentration. For example, sharp edges raise the stress concentration compared to spherical inclusions [320].

Non-metallic inclusions respond to a stress field around themselves depending on their composition, mechanical properties, structure and temperature of the field [171]. The inclusions can be categorized on the basis of their deformation behavior in different temperature ranges into three categories of deformability of wide range (e.g. MnS), plastic inclusion at certain temperature (non-crystalline glassy) but rigid at low temperature and brittle inclusions such as, crystalline silicates and spinoidals [134].

Studies on ductile fracture of alloys with hard second phase particles in a soft matrix shows that deformation causes microcracks in the bulk material regardless of the temperature of the experiment. Although equiaxed non-metallic inclusions are not responsible for fatigue crack propagation, non-metallic inclusions greater than the micro-roughness of the surface close to surface parts may create fatigue cracks [85]. Size and density of inclusions in the steel also affect the formation of embryonic micro-cracks near inclusions and change fracture and other properties in steel ([184], [187]). Stable void growth ratio for the voids around the inclusions gives a quantitative parameter for the void growth process due to non-metallic inclusions during ductile fracture of steel. This reveals the effect of volume fraction, distribution and shape and composition of nonmetallic inclusions such as MnS on the ductility of steel [321]. Dunne and Katramados [107] studied void formation and growth under compressive force at high temperature for titanium alloys. Gubenko [115] claimed that crack resistance increases by slippage of inclusions in the steel at high temperature along the inclusion-matrix interface boundaries. Different thermal conductivity between the steel matrix and inclusions modifies the stress distribution in the region with inclusions compared to the one without any inclusions or

with different inclusion density. In fatigue tests, micro-stresses of thermal origin around non-metallic inclusions are eliminated before the nucleation of cracks [51]. Kardomateas [322] suggested that a ductile fracture procedure started by a crack initiated at inclusions. The crack then propagates by void growth and coalescence, which forms elongated dimples on a plane of high shear stress or equiaxed dimple on planes normal to the direction of maximum tensile stress. His investigation in lower hardening alloys showed that symmetry decreased crack ductility. Figure 37 shows the voids created adjacent to the inclusions deformed due to a stress field around the inclusions. The voids can also propagate to form cracks [219].

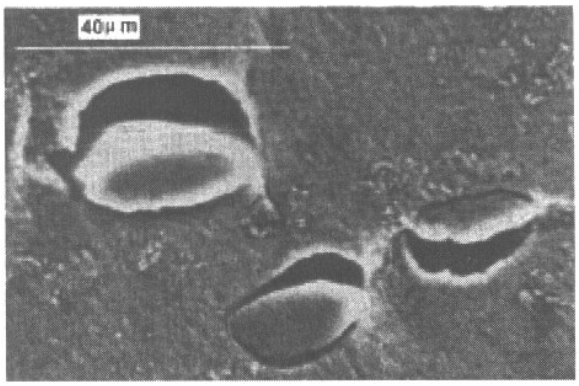

Figure 37 Voids around the inclusions as a result of inclusion deformation (courtesy of [219]).

In the case of non-deformable inclusions, interfaces debond and embryonic voids are generated [166]. Waudby [162] predicted that the conical cracks at the end of the inclusions have the tangential component of the friction forces at the surface of the inclusion. Forces induced by flow of material widen the crack and its base resulting in a conical shaped crack at the end of the inclusions. A fishtail shape partly filling in the conical void can be constructed because of higher forces at the surface of the inclusion compared to its center. Non-plastic behavior of inclusions results in conical shaped voids at the ends of inclusions due to enveloping the inclusions by the flow of the matrix. The actual behavior depends on the bonding interface between inclusions and

matrix and stress and strain states as well as mechanical properties of inclusions and matrix ([22], [24]-[26], [79]-[81], [166], [171]). This can be because of the flow of material matrix above and below undeformable inclusions in the stress flow direction and inability of the flow of steel in contact with the inclusion ([22]-[26], [83]). Gubenko [323] stated for inclusions under strain localization, micro-failure formed in and near inclusions and created a level of inhomogeneity that increases as the rigidity of the inclusion increases.

In the case of the deformable inclusions, eventually the length of the inclusion increases in the direction of streamlines and inclusions take the shape of the streamline and stand less against the flow passing the inclusion ([324],[325]). Baker and Charles [166] discuss the relationship between friction and interface using plasticine in a steel bar model and parallel-sided steel model deformed by forging. They stated that inclusions create an undeformable zone called dead zones above and below inclusions as these regions get more constrained by deformation. Their results show that the gaps between the fragments of the crushed inclusion can be filled by the matrix only if they get far enough by a critical distance from each other. In addition to the relative strength of the inclusion to the matrix the length of the inclusion seems to play a role in constraining the matrix [166]. The flow of the movement of inclusions in the matrix is not determined by inclusions' shape, size, and their orientation relative to the direction of deformation and the magnitude of frictional forces acting along the interface [171]. The mechanism of the formation of the crack around inclusions due to irregular internal stresses can be studied in the steel matrix that experiences external forces. Thermo-mechanical forces create four types of fractures in the inclusions due to compression and shear stresses. These types are, brittle fracture of undeformed inclusions, tough fracture of low plasticity inclusions initially elongated plastically, brittle fracture, and multiphase inclusions with phase separation boundaries

[171]. Mechanical forces in the form of compressive and shear forces exert friction force on the interface of the inclusions within the matrix. These interfacial forces modify the inclusion shape from equiaxed to ellipsoidal. If the forces exceed the intermolecular strength of inclusions, brittle fractures occur as the interfacial surface increases. These changes increase the inclusion density and interaction between dislocations in intersecting planes and create more obstacles to the flow of material, which ultimately results in hardening of steel by impending slipping of the inclusions [171]. Deformation of non-metallic inclusions can give steel anisotropic properties and degrade its quality by multiplying the number of defects such as hairline cracks, pinholes, tears, cracks, blisters, torn edges and banded structure [148].

The formation of the crack resulting from the internal forces has been studied theoretically using numerical method and FEM computational simulation in many publications. Stadnyk [326] gave analytical and exact solutions for stresses and displacements of elastic stress on the surfaces of the ellipsoidal inclusion under the conditions of uniaxial tension. Luo and Ståhlberg [327] analyzed the generation of voids in the vicinity of a hard inclusion. They showed the interface between matrix and inclusion is separated after a critical tensile force. They suggested that normal tensile stresses developed during deformation by the difference in yield stress between inclusion and the steel matrix at the interface is responsible for separating the inclusion and the matrix. Saimoto and Nisitani [270] published their simulation results for crack propagation using Body Force Method (BFM) extended by ordinary boundary type method and implementation of stress field analysis distributed by standard point force doublet for mode I and mode II to avoid numerical integration. They used their method to study the crack propagation in a rectangular plate having a circular inclusion and the stability of crack propagation path in a double cantilever type specimen. They found three characteristic sections in the path of the crack

propagation in the vicinity of a hard circular inclusion in their computer simulation. These sections are initial nearly straight path, detour around the inclusion and path with no effect of reinforcement due to inclusions. They gave the path stability for crack propagation on the basis of their results for the double cantilever type specimen in the order of tensile load, shear load and pure bending. In addition, Harik and Carincross showed the voids change around a cylindrical inclusion with time dependent evolution as the level of strain state and concentration of stress increase [328]. Theoretical models presenting the effect of hard inclusions on the formation of microcracks in the steel are assumed to have strong bonds between the second phase and the matrix ([329], [330]). Determining the strength of steel against different fractures related to the different inclusion size and inclusion volume percentage [85]. Results of computer simulations of Saimoto and Nisitani [270] showed that the crack path nearby a hard circular inclusion experiences reinforcement increase as the ratio of rigidity between inclusion and the matrix gets higher or the distance between the inclusion and initial crack becomes smaller.

6.2 ASPECT RATIO

Some researchers attempt to define a different measurement method for describing the deformation of inclusions imposed by residual stresses around the inclusion. Inclusion deformation is related to the ratio of ductility of the inclusion to that of the matrix containing the inclusion.

Scheil and Schnell proposed the ratio of major to minor axes of the ellipse for this measurement. They used the idea of deforming a spherical inclusion into more and less elongated ellipses during flattening cylindrical steel specimens in a press. This value can be

compared to the initial condition to determine the deformation [180]. Equations 68 and 69 are the mathematical form of Scheil and Schnell method for initial and upset specimens;

$$\lambda_o = \frac{a_o}{b_o} \quad \text{(Eq-68)}$$

$$\lambda = \frac{a_1}{b_1} \quad \text{(Eq-69)}$$

where a_o/b_o and a_1/b_1 are the diameter/thickness ratio for initial and upset specimen respectively.

Pickering defined the inclusion deformation using reduction in cross sectional area of the original ingot during deformation according to the following formula [181];

$$\frac{a_1}{b_1} = \left(\frac{F_o}{F_1}\right)^{3/2} \quad \text{(Eq-70)}$$

In equation 70, F_o is the cross-section area of the original ingot and F_1 is the cross-section area of the deformed bar. The ratio is greater than unity for inclusions softer than the steel matrix and less than one for harder inclusions with lower plasticity than steel.

Malkiewicz and Rudnik implement the Hancky's true elongation to measure the deformation of inclusion in steel and to introduce an index of deformability ν given in the relationship [118] in Eq-71;

$$\nu = \frac{2}{3}\frac{\lg\lambda}{\lg h} \quad \text{(Eq-71)}$$

where $h = \frac{F_o}{F_1}$ and $\lg\lambda$ is the ratio of true elongation. Brunet and Bellot [331],

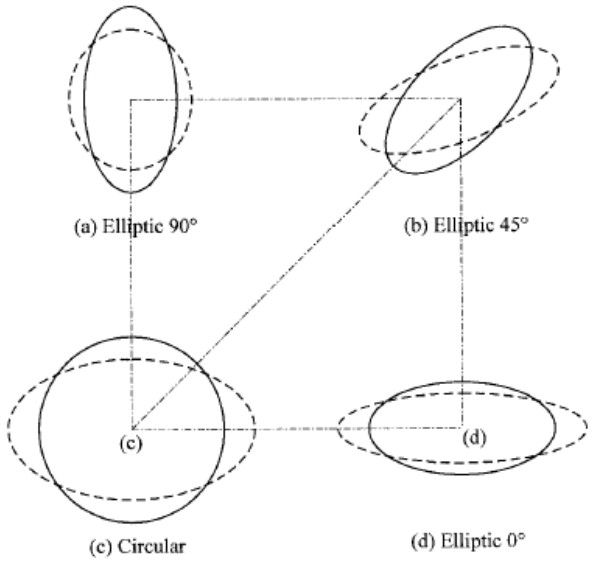

Figure 38 Different angles between upsetting and inclusion orientation

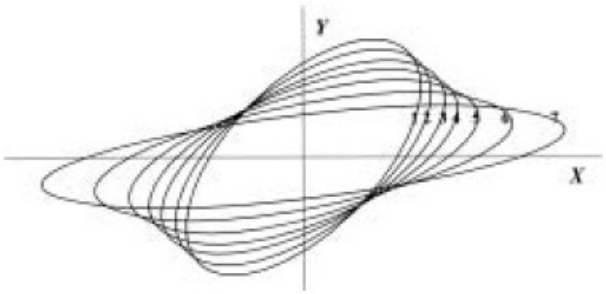

Figure 39 Evolution of deformation for inclusion with 45 degree orientation with respect to upsetting force.

Vodopivec and Gabrovsek [176] Baker and Charles [166] have given several relationships on the basis of this definition for deformation behavior of inclusions in steel. Luo and Ståhlberg [196] used index of deformability to show the deformation of inclusions with different upsetting orientation (Figure 38 and Figure 39).

6.3 MICROSTRUCTURAL OBSERVATION OF FLAW FORMATION AROUND INCLUSIONS INCLUSION

Cooling of the slab generates a thermal stress distribution around the region of the steel matrix containing inclusions. This can affect the interaction of the inclusion and the matrix during cooling because of their differences in thermodynamic material properties. Heat is transferred to the surfaces of the slab by conduction. Inclusions and the steel matrix also contract in a different manner because of dissimilarity in their thermal expansion coefficients. This creates volumetric stresses at the interface zone of contact surface between inclusions and the steel matrix. The volume contraction misfit causes contact surfaces separation initiated from the weakest cohesive zone in the interface region. It, consequently, creates a void and microcracks close to the inclusion due to the thermal gradient produced during slab cooling.

To prove that microcracks exist around the inclusions, several small samples of steel grade 1319* were prepared from the available continuous case slabs used for the NDT tests with the same method of mounting and polishing as was explained in the NDT section. The samples were detected by ultrasonic NDT to contain inclusions. It is obvious that the density of inclusions per unit volume can be an important factor in formation and/or propagation of such a crack. Figure 40 is a photomicrograph of sample cut from an air-cooled cast slab cut from the B-external position in the cast slab, which was heated up to the austenite temperature and quenched in an ice bath. Flaws between two aluminum oxide inclusions can be seen clearly in Figure 40.

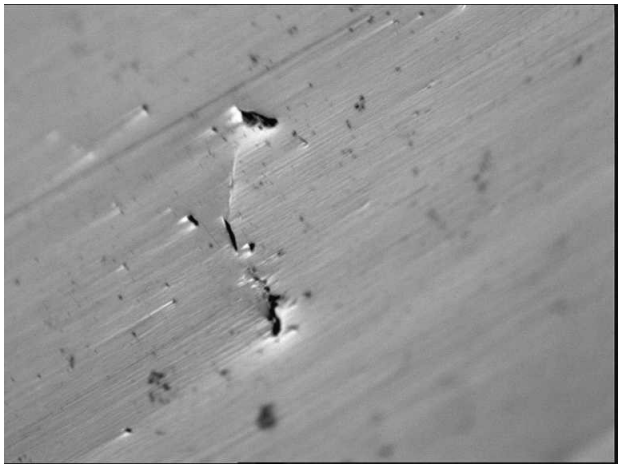

Figure 40 Evidence of microcrack formation around inclusions in the steel grade 1319* from sample slab of B ext group, quenched from austenite temperature.

This shows that the relation between inclusions and voids and cracks is a rather complicated, and depends on other factors such as inclusion type, density, distribution and many other factors.

6.4 SIMULATIONS OF INTERACTION BETWEEN INCLUSION AND STEEL MATRIX INCLUSION

Drawing from the large body of existing research, this research work investigated the deformation of an inclusion embedded in a matrix resulting from stress fields that develop around the inclusion. The FEM analysis simulated the reaction of an inclusion embedded in a steel matrix in response to a developing stress field and thermal gradient through the bulk of the steel. These models help to study the matrix-inclusion interaction during changing two major inclusion specifications of shape and volume changes.

The cooling of a spherical inclusion embedded within a square matrix box is simulated in a 2d axisymmetric model. Since the microcracks are mainly formed around inclusions harder

than the steel matrix, this case is considered in the simulations of interaction of inclusions and steel matrix due to stress fields in the vicinity of the inclusion. The cooling agent in the model is water with the film or convection coefficient of 500 $Wm^{-2}K^{-1}$ [332]. The emissivity coefficient is considered to be 0.8 for reddish to grey color from 1300 ^{o}C to room temperature. The model is exposed to a cooling agent from the top surface in the simulation box with axisymmetric and fully constrained boundary conditions. The thermal condition of all sides of the simulation box, except the top surface, is adiabatic, i.e., heat exchange with the system is zero ($\delta Q = 0$). Figure 41 (41a and 41b) are schematic views of the boundary conditions for axisymmetric and fully constrained simulations, respectively. The inclusion is at the bottom left corner of the model box. The model was meshed denser around the interface which is the critical region in the simulations. Material properties of α–alumina with 99.9% purity are used for the simulation due to lack of direct information of mechanical and thermal properties of the aluminum oxide inclusion. The material properties of the aluminum oxide ([333]-[335]) and steel matrix [145], [336]) used in the model, are listed in Table 7 during cooling of the inclusion and the matrix from 1300 ^{o}C. The material properties of the alumina and the steel matrix in all of the simulations are considered to be temperature independent. The inclusion and matrix bodies are modeled with a plane element with designated number 223 in ANSYS element reference. It has eight nodes with up to four degrees of freedom at each node and capability of coupling fields. The element is set for thermal-structural analysis. The interactions of the inclusion with the steel matrix are modeled with three different numerical methods for contact problems available in ANSYS. These methods are interfacial contact element, interfacial cohesive zone elements and glue surfaces in contact.

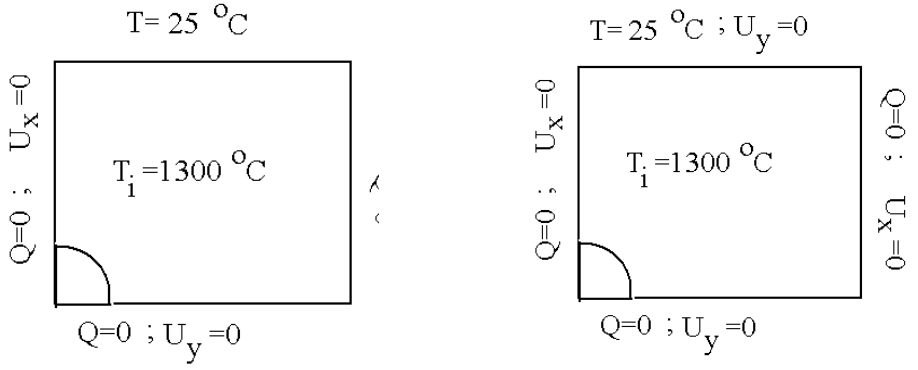

(a) Axisymmetric (b) Fully constrained

Figure 41 General schematic view of inclusion and matrix boundary.

Table 7 Mechanical and thermal properties of Al_2O_3 (α-alumina 99%) and the steel used in the simulations.

Material Property	**Al_2O_3**	**Steel matrix**
Elastic modulus ,GPa	393	210
Coefficients of thermal expansion , 10^{-6} / °C	8.3	15
Poisson's ratio	0.22	0.29
Mass density (×1000 kg/m3)	3.99	7.8
Specific heat J/kg (25-1000 °C)	1050	460
Thermal conductivities (×100W/cm . K)	13	33

In the contact element method, an interfacial layer is built at the inclusion-matrix interface with combination of the outermost elements of two surfaces in contact. In numerical analysis of this class of bonding, the three nodes Conta-172 element are associated with its compatible target element Targe-169. The cohesive force at the contact layer interface of the models is set to be 0.2 GPa with a thermal conductivity of 33 W/(m.K).

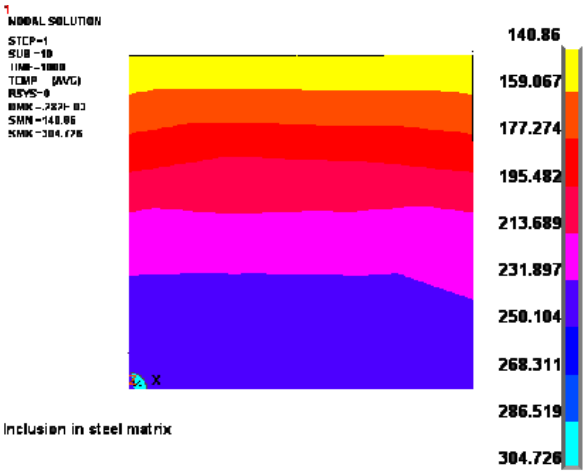

(a)

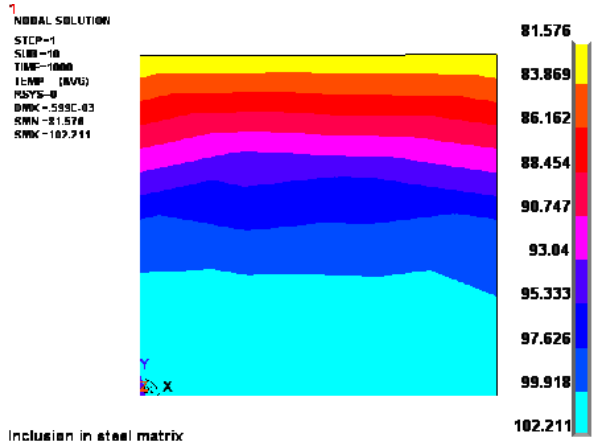

(b)

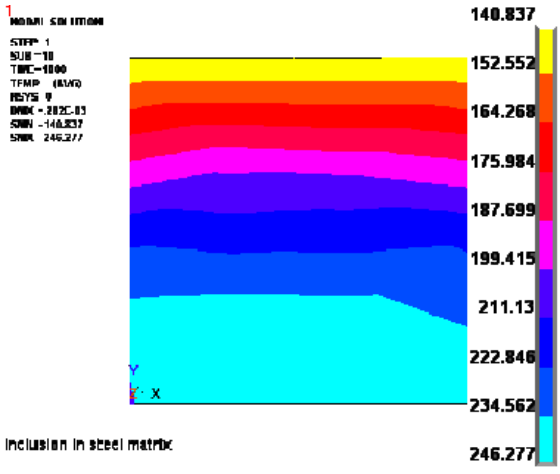

(c)

Figure 42 Temperature distribution [^{o}C] in the model of Al_2O_3 inclusion and steel matrix with (a) contact layer interface (b) cohesive zone interface (c) glue interface.

The second is the cohesive zone model to create a physical interface zone without the contribution of inclusion and matrix material by generating new elements at the interface with cohesion properties. The cohesion force of the interface is 2.1 GPa with 10 and 30 micrometer allowance for normal and tangential contact separation, respectively. This method is performed by the Inter-203 element which is a 6-node linear interface element. In the third class of interface definition, surfaces of the inclusion and the matrix are joined at the interface to study a homogenous thermodynamic inclusion-matrix model. In this method, there is no abrupt change in the thermal-structural field due to the presence of the interface. However, the abrupt change takes place because of the material property changes.

The characteristics of the interface of a non-metallic inclusion with the steel matrix govern the thermal and mechanical load exchange between the two phases. It is important to notice in the simulations presented in this paper that only the thermally induced strain due to material expansion/shrinkage by the thermal gradient produces thermal-structural interaction between the inclusion and the matrix and no other microstructural phenomena such as solid-solid phase transformation or diffusion has been considered. In all models, both the matrix and the inclusion have uniform initial temperature of 1300 ^{o}C. All simulation results are captured after 1000 time steps. All models are applied to the axisymmetric boundary conditions unless it is indicated otherwise. The model is a quarter circle of 2 mm radius in a 1600 millimeter square simulation box. Temperature distributions for the three classes of the interface are shown in Figure 42. The heat transfer method at the interface, defined by the glue technique, contact elements and cohesive elements, are conduction, convection and combination of the radiation with convection, respectively. Figure 42 (42b and 42c) present continuous temperature distributions across the interface built by cohesive zone elements and the glue technique. It is not

the case for the contact layer method employed by interfacial contact elements (Figure 42a) since a discontinuity of the thermal field at the interface causes a higher temperature prediction for the inclusion compared to the two other methods. However, Figure 42 shows a faster cooling rate for the cohesive zone due to higher order heat transfer by radiation at the interface instead of the conduction heat transfer for the glue interface. The interface in the applied cohesive elements model, unlike the simple glue technique interface, is not only a border line between two phases but it is a physical interfacial layer with 200 MPa cohesive forces at the interface.

Passing heat by convection in the interfacial contact element rather than conduction in glued surfaces in contact can explain the higher temperature of the inclusion in the model with the interface defined by contact elements in comparison to the glue technique interface. Therefore, it can be concluded that the physical rule applied to the inclusion-matrix interface has an important role in predicting the interaction of the inclusion and matrix in response to the thermal load. The influence of the interface properties in transferring the thermal and mechanical stress between two phases can be perceived better if the Von Misses stress distributions around the inclusion for the models with different interfacial techniques are compared (see Figure 43). Applying the glue technique at the interface (Figure 43a) or defining the interface properties by the contact layer method (Figure 43b) develops localization of the stress in a narrow stress concentration zone at the interface. Both methods predict accumulation of the residual stresses about 0.7 GPa at the interface. The cohesive zone interface (Figure 43c) calculates the equivalent stress at the interface region as high as 0.95 GPa in a homogenous continuous stress field. Boundary conditions also modify the shape and size of the stress concentration zone at the interface region. This fact can be observed if a more critical boundary condition such as a fully constrained boundary condition of the simulation box is imposed on the model.

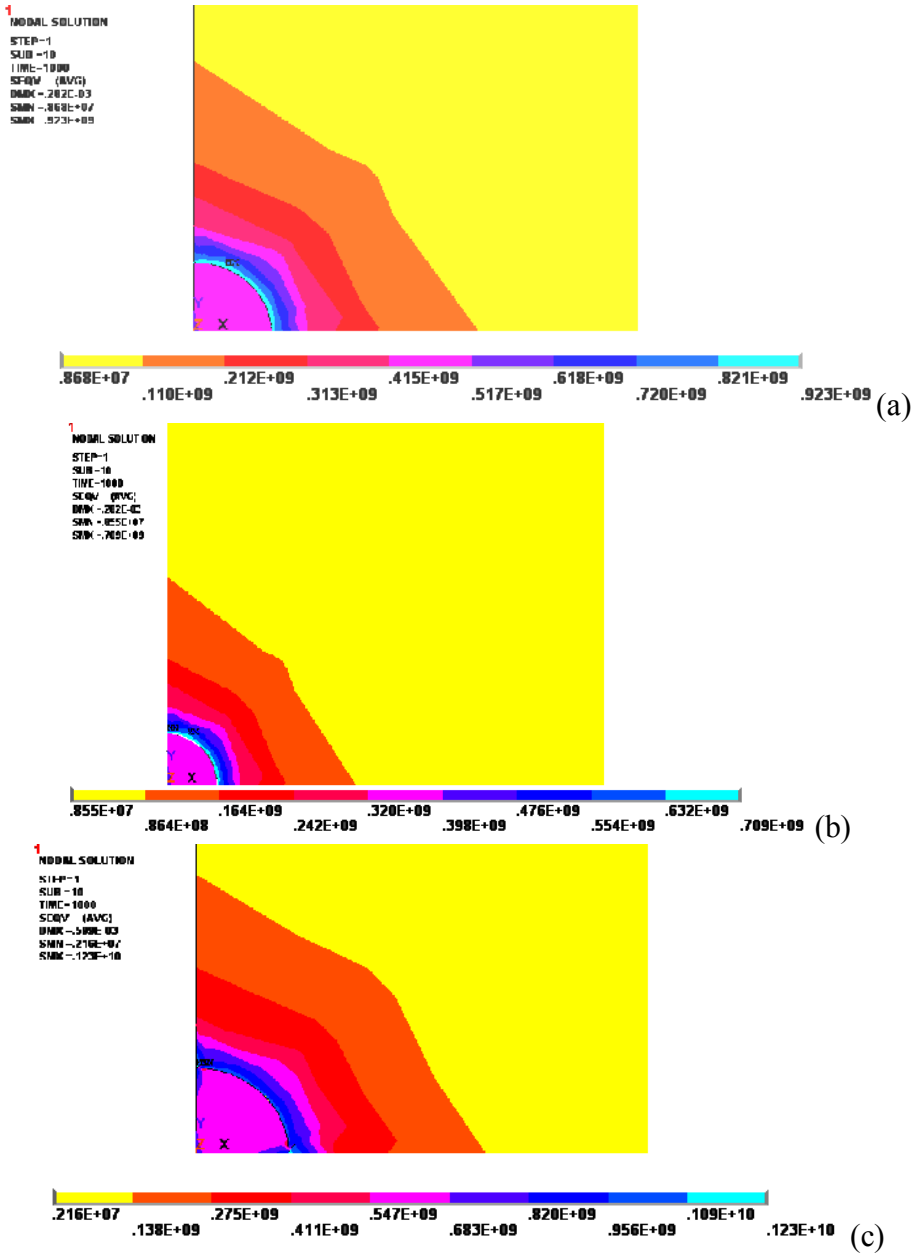

Figure 43 Equivalent Von Misses stress distribution [Pa] in the model of Al2O3 inclusion and steel matrix with (a) glue interface (b) contact layer interface (c) cohesive zone interface.

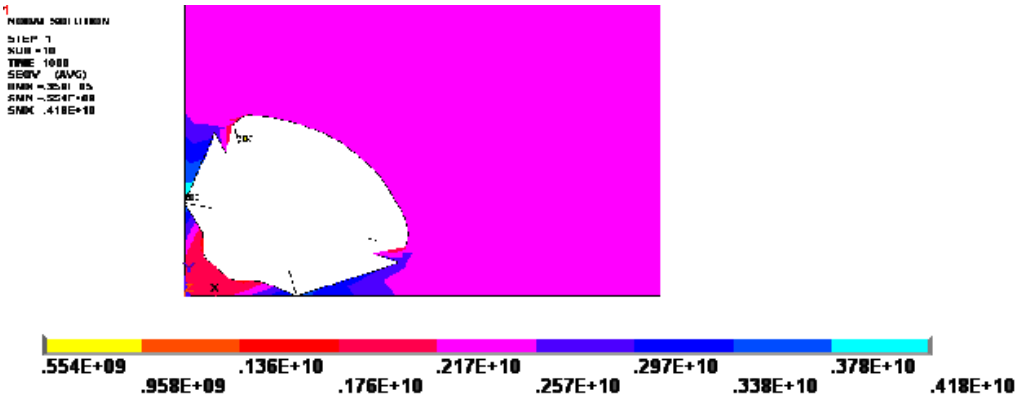

(a)

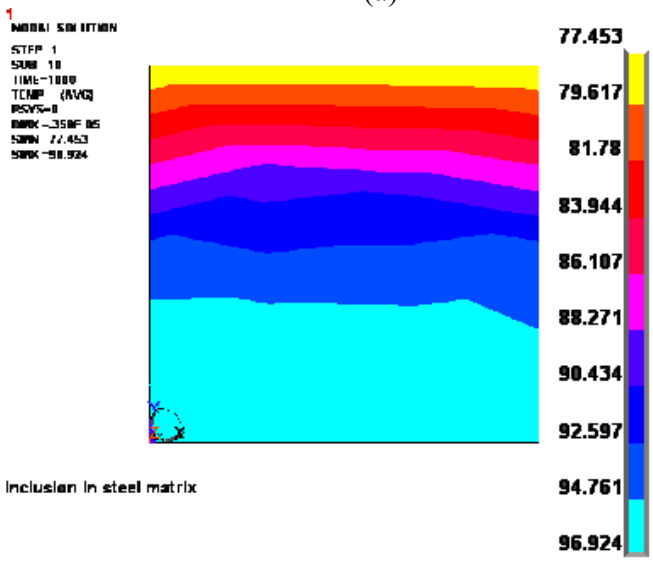

(b)

Figure 44 Fully constrained (a) equivalent stress distribution [Pa] (b) temperature distribution [^{o}C].

Figure 44 shows the equivalent stress distribution and temperature distribution for the fully constrained model with a cohesive element interface. The interfacial cohesive elements have the ability to expand at the interface under tensile load to simulate the separation of the surfaces in contact at the interface. Figure 44(a) is a model with fully constrained boundary conditions for the inclusion-matrix interface defined with the cohesive elements. It shows the void formation around the inclusion in the simulation. This behavior is similar to the experimental evidence in Figure 41. By comparing Figure 44(b) and Figure 42(b), one can notice

that the cooling rate is higher under fully constrained boundary conditions which can occur as a result of different directions of the flow of the material by shrinking of the matrix.

Series of simulations with different inclusion radii (r_{inc}) are performed to study the effect of size of the inclusion and the area fraction of hard non-metallic inclusion material on the maximum equivalent von Mises stress (σ_{eqv}) at the interface during the cooling process. Two non-dimensional parameters are defined for stress distribution and geometry factor by normalizing the maximum equivalent stress with the interfacial cohesive force (σ_{coh}) and taking the ratio of the inclusion radius to the side of the simulation box (L_o) which represents the matrix material affected by the inclusion deformation. These dimensionless parameters were plotted against each other in Figure 45. Since L_o and σ_{coh} are kept constant in these simulations, the plot in the Figure 45 shows the variation of the maximum stress at the interface for different inclusion size. The plot shows that as the size of the inclusion (r_{inc}) is increasing, the residual stresses accumulated by induced thermal strain at the interface are decreasing. However, the curve approaches an asymptotic value of 0.5 for inclusions larger than critical size. The axes of the graph in Figure 45 are independent of the unit of the radius of the inclusion and concentrated residual stress, therefore, it depends on the nature of the interface between hard non-metallic inclusions and the steel matrix used in these simulations. Hence, the maximum stress at the interface is independent of the size of the inclusion. The maximum stress is a function of the ratio of the inclusion radius to the depth of the region in the matrix affected by the thermal-structural interaction between the steel matrix and the inclusion. The maximum stress at the interface is also a function of the cohesion force built at the interface during solidification of the steel matrix.

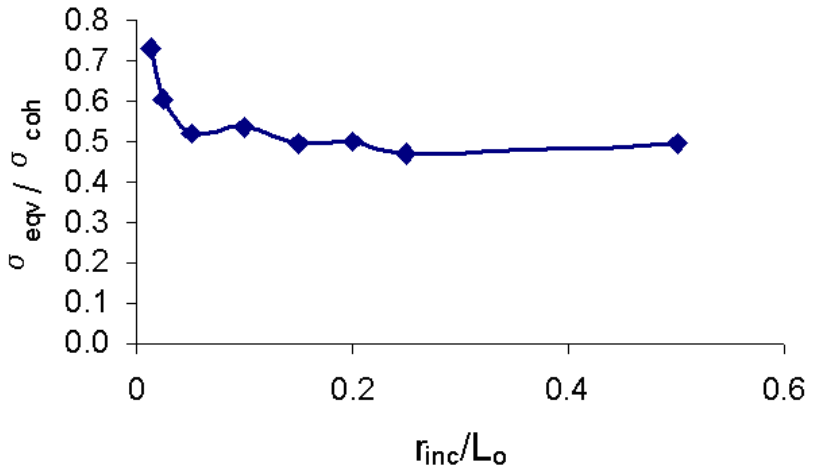

Figure 45 Non-dimensional presentation of the inclusion size effect on the equivalent stress distribution induced by thermal strain of inclusion and matrix at the interface.

The strength ratio between inclusions and the steel matrix defines the non-metallic inclusions to be soft or hard inclusions, or both. Investigation of the influence of the composition on the residual stress concentration at the inclusion-matrix interface is accomplished via similar simulations with different modulus of elasticity of the inclusion. Ratio of the logarithm of the modulus of elasticity of the inclusion to the logarithm of the modulus of elasticity of the matrix, log ($E_{inclusion}$)/log (E_{matrix}), gives a dimensionless factor to judge the rigidity of the inclusion in a given matrix. It is observed that the risk of the separation of the contact surfaces at the interface is more for an inclusion with a rigidity factor higher than one. A dimensionless stress concentration factor is defined as the ratio of the average accumulated residual stress in a region in the model to the defined interfacial cohesive force of the cohesive zone elements. The stress concentration factor provides a tool to examine the variation of stress concentration regardless of the dimensions applied to the model. The stress concentration factor is defined for the average stress concentration in the inclusion ($\sigma_{inclusion}$), at the cohesive zone elements ($\sigma_{interface}$) and at the matrix surface of the interface (σ_{matrix}) as log($\sigma_{inclusion}$)/log (σ_{coh}), log($\sigma_{interface}$)/log (σ_{coh}) and

log(σ_{matrix})/log (σ_{coh}), respectively. Figure 46 shows the variation of the stress concentration factor in the examined region versus the rigidity factor of the inclusion. It can be concluded from the plot in the Figure 44 that changing the composition of the inclusion from soft to rigid, increases the stress concentration within the inclusion. It can be seen in Figure 46 that the stress concentration factor is minimum within the interfacial cohesive zone elements and maximum at the matrix contact surface to the interface where the modulus of the elasticity of the inclusion is close to the modulus of elasticity of the matrix. It seems from the plot in Figure 46 that the stress distribution within the inclusion for the softer inclusions is controlled by the properties of the interface but the stress distribution in the hard inclusion is influenced by the property of the matrix.

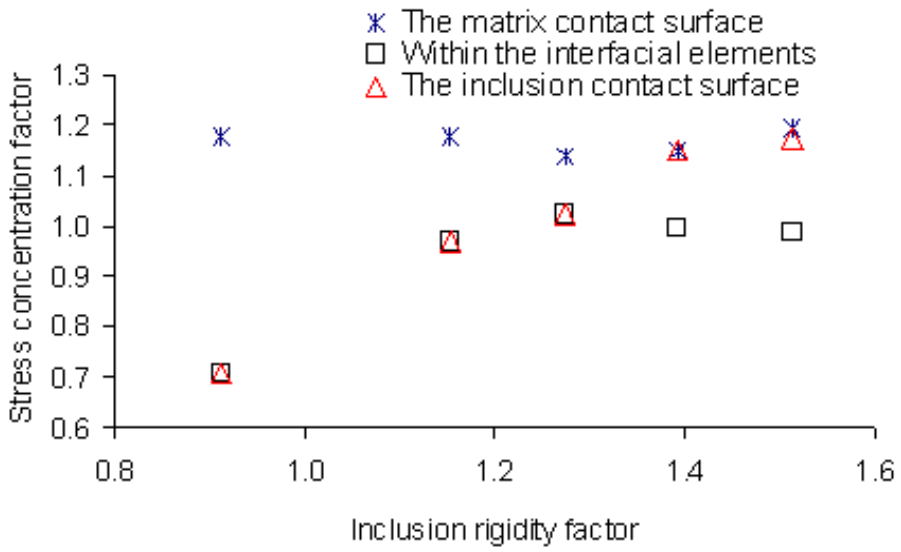

Figure 46 Variation of the stress concentration factor with increasing rigidity of the inclusion as compared to the rigidity of the matrix within an inclusion phase, at the interfacial cohesive elements and surface contact of the matrix at the inclusion-matrix interface.

7.0 COOLING EXPERIMENTS OF AS-CAST STEEL

7.1 COOLING EXPERIMENT PROCEDURE

A series of cooling experiments with different cooling rate were set to produce crack and flaw in continuously case steel. Two sets of samples with different dimensions from 1010*, 1319* and 1091* grade of continuous casting steel in two sets with different dimensions. All samples were verified by the pretest NDT images to be almost defects free. The small size samples were cut in the 13 mm^3 and cooled after encapsulating. The second set of the sample were cut in a block with dimension of 75 mm x 75 mm and 50 mm thickness. The samples were conducted to the microstructural analysis to detect the formation of the flaw as a result of the accelerated cooling rate. No defect formation was found in the encapsulated samples therefore the results are not discussed in this chapter. The results of the air cooling of large set of the samples which produced cracks in the samples are presented in this chapter.

7.2 EXPERIMENTAL PROCEDURE

To monitor the temperature variation through the sample thickness during cooling experiments, all samples were drilled by 3 mm (1/8 inch) drill bit which is almost twice of diameter of the thermocouple to avoid sticking inside the sample because of volume changes due to high

temperature during heat treatment. The holes were drilled at distance 8 mm, 13 mm and 25mm from top surface with depth of 25 mm from cut side (with bright color). Figure 47 is a view of the design for the samples used for this experiment with its dimension.

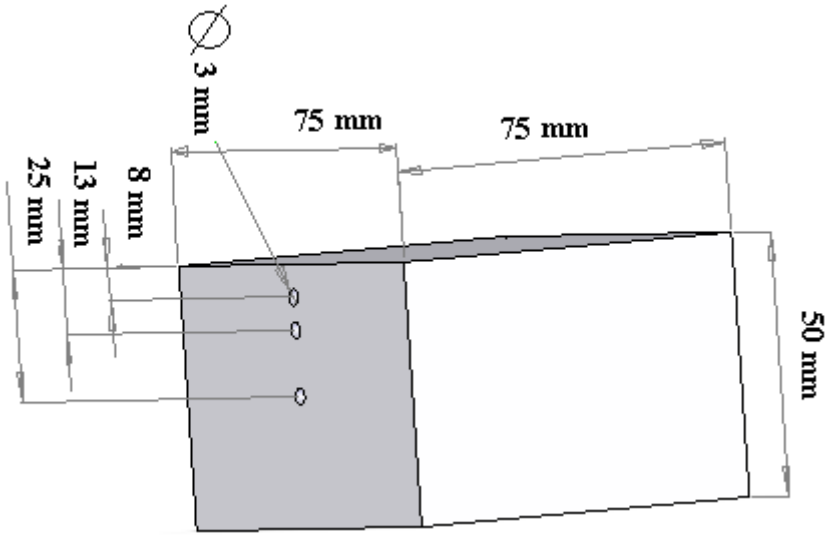

Figure 47 Schematic view of the sample used for the cooling rate experiment.

The furnace was set to the austenite temperature range between 900-1100 C depending on the grade of steel and was kept for 15 to 30 minutes at this temperature to homogenize the temperature across the furnace.

A three channels Lab view interface program was recoding the data from the sample in real time. The program presents the data in both real time and average over 50 points' samples data in two different graphs as the experiment is proceeding. The program was set with DAQ Rate 1000 Hz, Effective DAQ 20 sample/second. The lab view program is running in a desktop PC computer and DAQ channels are connected to three thermocouples, which are inserted into the sample holes. Sample is put in and out of the furnace using a fork.

A conveyer facilitated smooth sliding of the sample in and out of the oven to avoid removing the thermocouple from its place and to ensure the contact of the thermocouple to the

sample during experiment. The furnace was adjusted to a desirable temperature. Figure 48 is the picture of the system used in these experiments.

Figure 48 Experimental set up.

The data were recorded during both austenization and cooling process in different files. Both processes need predefined data and procedures. During austenization, the samples were heated above the austenite temperature and the cooling rate was monitored from the austenite phase to have as uniform carbon content as possible. The changes in microstructure were studied using post image processing ultrasonic NDT test developed in this research work (see section 5 and [337]). Steel grade 1010* and 1319* are hypoeutectoid steel and 1091* is hypereutectoid steel. Hence, austenitizing temperature in the phase diagram for 1010* and 1319* are above A3 line and for 1091* is above A_{CM} line. Therefore, it was necessary to estimate the starting and ending range of solid-solid phase transformation region, which is the temperature range falling between A_1 and A_3 or A_{CM} in the iron-carbon phase diagram, during heating up and cooling down for each of the material.

Having the qualitative and quantitative information about the components in the microstructures of each sample, a commercial software called JMATPRO estimates austenitizing temperature which is the temperature labeled as A_3 and A_{CM}. This temperature varies with alloy content.

The carbon equivalent for the steel grade 1010*, 1319* and 1091* can be computed as 0.2128, 0.4356 and 0.5474, respectively. Room temperature was checked before each experiment, and the cooling rates were measured during cooling after heating them up to the austenite temperature.

The Lab view program and thermocouples were checked to calibrate them during the experiment time for a given cooling rate. The necessary calibration between thermocouples was set before each experiment. The deviation between thermocouples was also checked and recorded for computational reasons. To do this, all thermocouples were placed next to each other to measure the temperature at same spot in the furnace and the differences are recorded.

Recording of the heating process started after initial parasite signals in lab view graphs as the temperature started to increase through the sample thickness from exterior to interior and it ended when all of the thermocouples showed the austenite temperature range. The interior thermocouple at the center of the sample indicates when the temperature all over the sample reaches above austenization temperature.

Using the CCT graph the final microstructure of steel of each grade for a given cooling condition can be predicted. CCT and TTT diagrams can be constructed by the aid of JMATPRO, given the qualitative and quantitative information about the solid-solid phase transformation in the steel composition of each sample. To have the same set up for all samples, the furnace was set up to be at the designated austenite temperature range before putting the sample in the furnace. The tested sample is left for 1 hour at this temperature to have uniform temperature in the furnace. Before putting the samples in the furnace, the thermocouples were placed in the holes inside the sample and fixed on the sample.

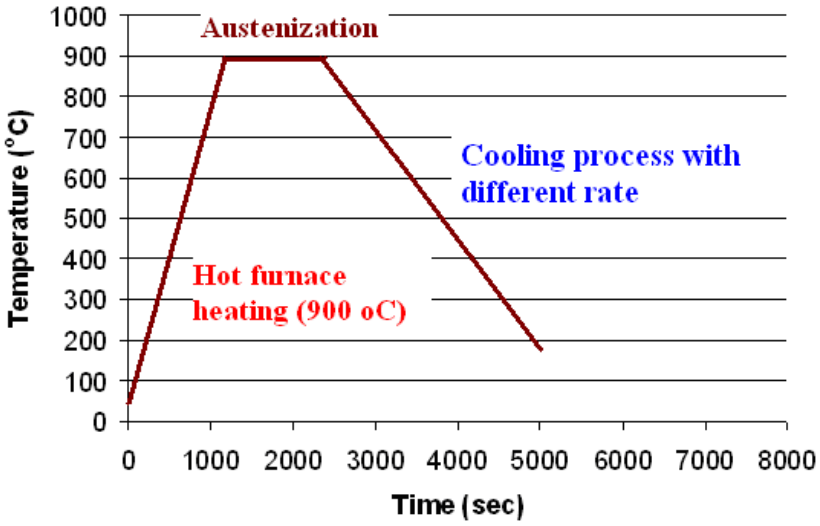

Figure 49 Schematic view of experimental procedure.

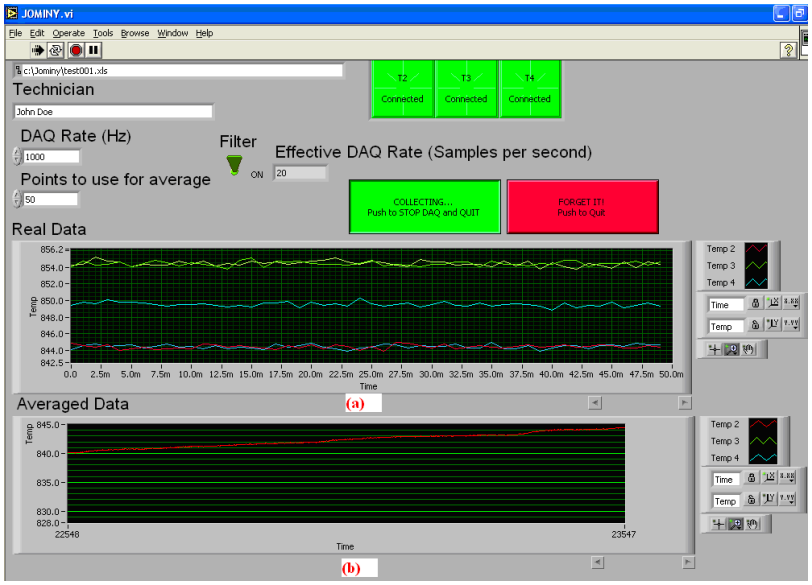

Figure 50 Interface of the Lab view program recoding the data captured by the thermocouple during heating and cooling of the sample; (a) the real time graph (b) time averaging graph; real time graph shows the difference between the thermocouples when they are placed in the furnace without attaching to the sample before the experiment on sample 503B (grade 1319*)

Data were set to be stored in real time in Excel files during heating and cooling processes for post processing and analyzing. The cooling rate recording was stopped near ambient temperature. The experimental procedure is presented schematically in the Figure 49.Figure 50

presents the Lab view interface and the difference between thermocouples for experiments on 1319* steel grade sample during the air cooling experiment.

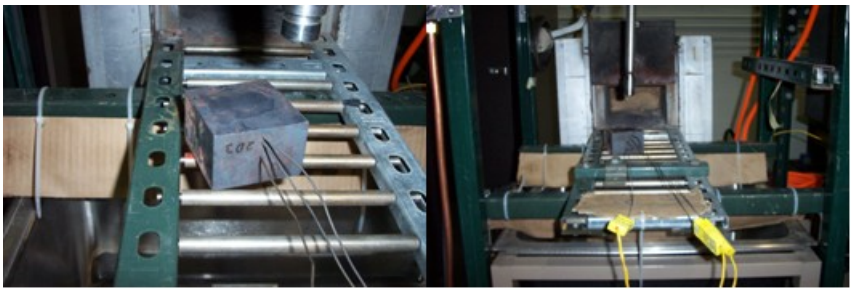

Figure 51 Recording data of the sample during cooling stage.

After the sample reaches the austenite temperature homogenously across its thickness, it was pulled out of the furnace with thermocouples connected to it. Figure 51 is an image of the sample during cooling with thermocouple attached to it. The sample was then exposed to a cooling agent depending on the desired cooling rate to start the cooling process. The cooling agent must be agitated whenever is necessary to have a constant ambient boundary around the surfaces of the sample. All the thermocouples were removed from the sample and results are saved and plotted in Excel file for detailed analyzing.

7.3 JMATPRO RESULTS

The NDT images of the distribution of anomalies in the slabs, from which samples were originally cut, are given for all five gates of NDT ultrasonic tests. Slabs for the tests were selected based on the available portion with little or no defects in their NDT images. The chemical composition and cooling history of the original slabs of the slab samples were available for estimation of CCT and TTT diagrams by JMATPRO (see Appendix A).

Figure 52 to Figure 57 are the CCT and TTT JMATPRO estimation for steel grade 1010*, 1091* and 1319*, in turn. The software estimates the solid-solid phase transformation based on the composition of the steel, the volume fraction of the elements in the microstructure and the grain size.

The TTT diagram gives the solid-solid phase transformation temperature for tested grade steel at equilibrium conditions. This gives an idea of the austenization temperature range for the heating process of the experiment. However, the experimental values may be different than the JMATPRO estimation values. The austenization temperature range for cooling rate higher than the equilibrium cooling case can be approximated by deploying the CCT diagram.

The asymptotic line for starting austenite decomposition in the CCT and TTT diagrams, calculated by JMATPRO for grade steel tested in the cooling experiments, are listed in Table 8. Sample cut from the slab of a specific steel grade will have single-phase austenite in its microstructure if its temperature is higher than the corresponding temperature for a given steel grade.

Table 8 JMATPRO austenitizing temperature computed for each tested steel grade. The sample will have uniform austenite texture above the austenization temperature.

Samples cut for air cooling experiments	A_3 /A_{CM} [C]
160530 grad 1010*	855
160530 grad 1091*	794
160530 grad 1319*	839

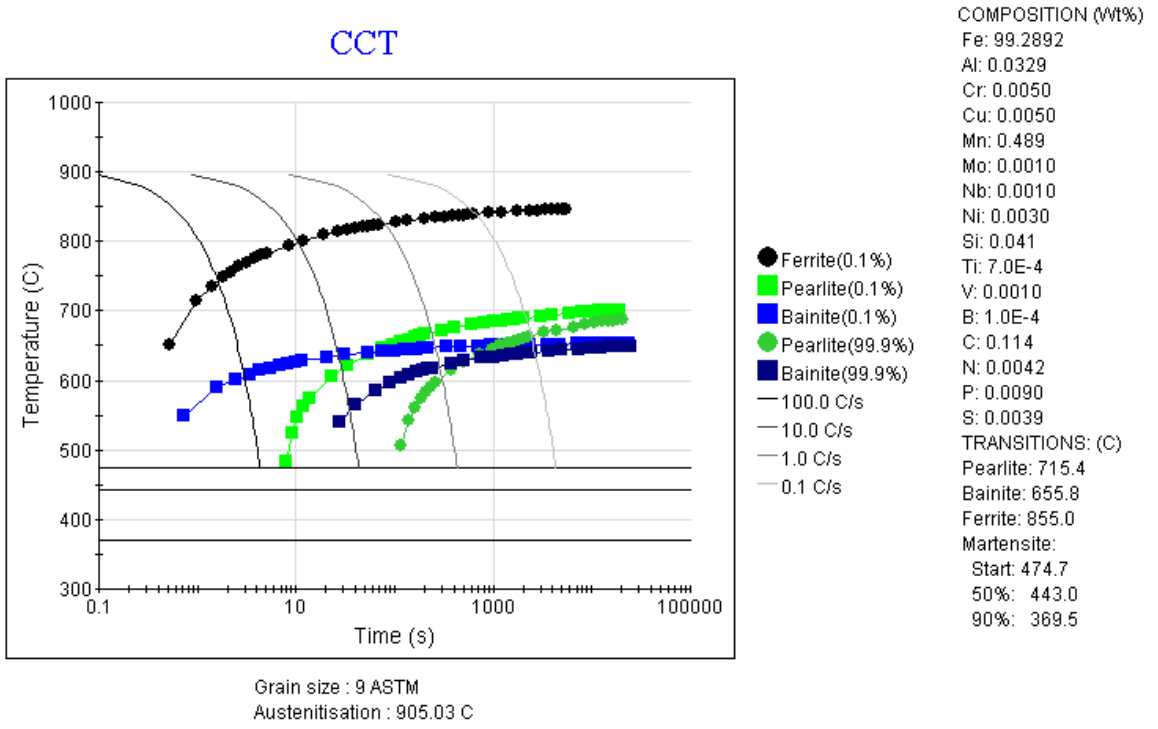

Figure 52 JMATPRO estimation for CCT diagram of Steel grade 1010* based on the composition provided by the manufacturer.

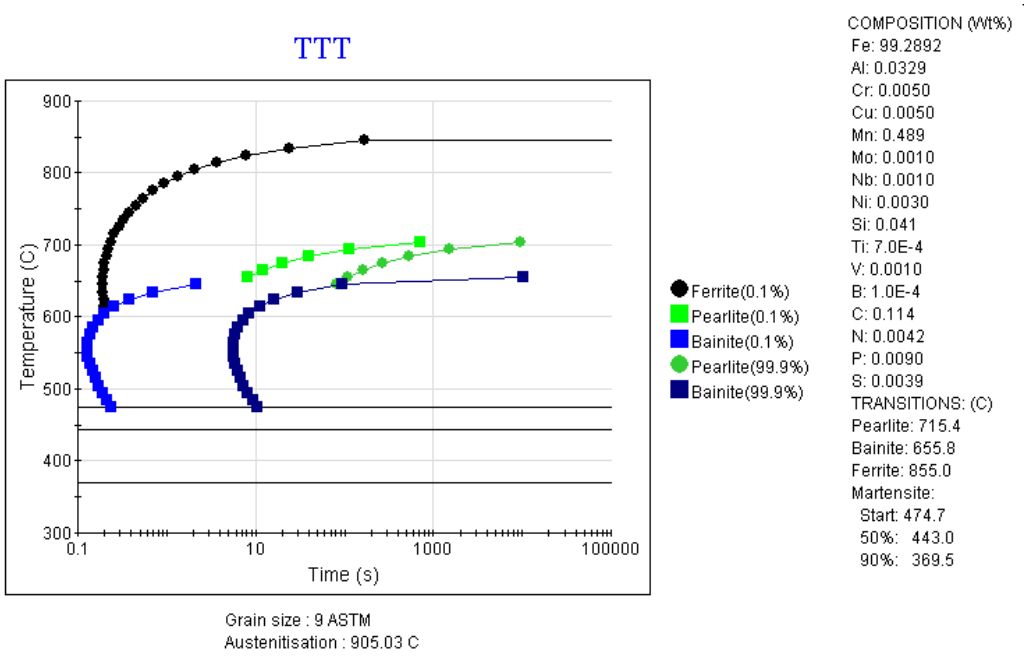

Figure 53 JMATPRO estimation for TTT diagram of Steel grade 1010* based on the composition provided by the manufacturer.

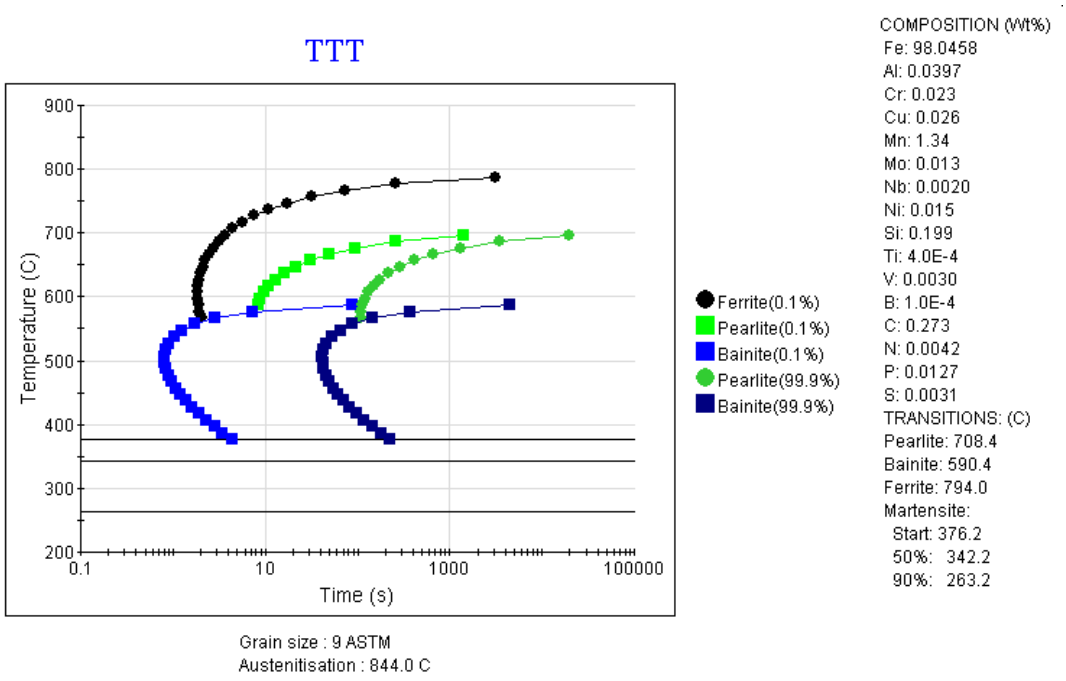

Figure 54 JMATPRO estimation for TTT diagram of Steel grade 1091* based on the composition provided by the manufacturer.

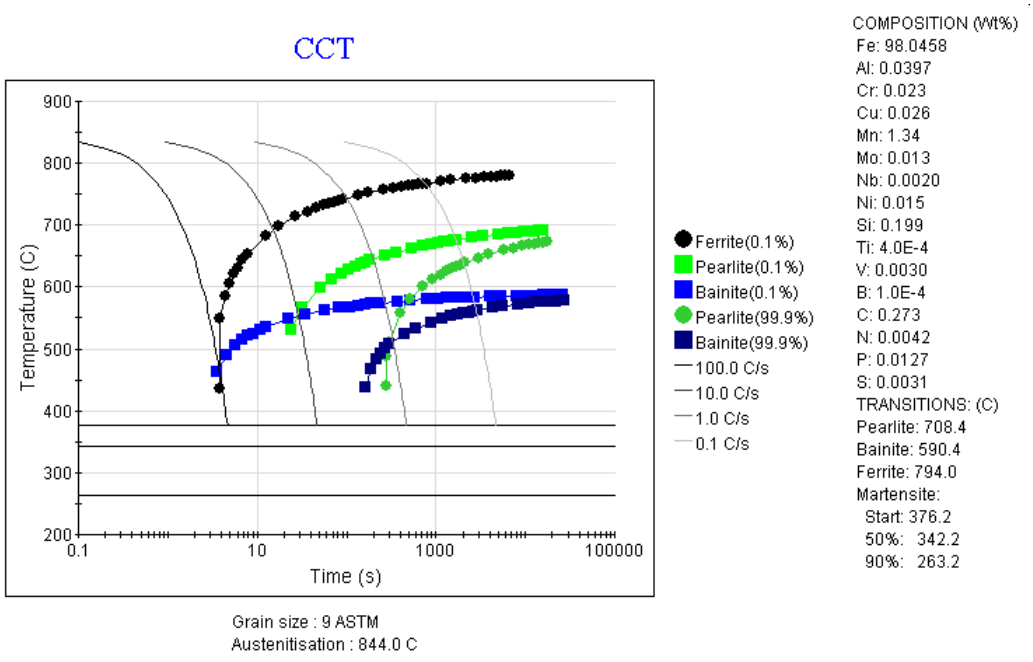

Figure 55 JMATPRO estimation for CCT diagram of Steel grade 1091* based on the composition provided by the manufacturer.

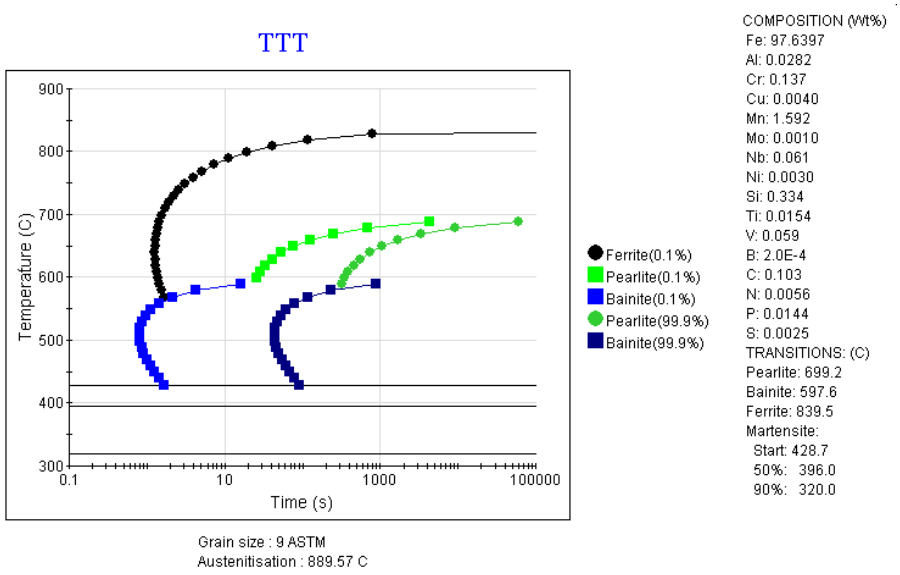

Figure 56 JMATPRO estimation for TTT diagram of Steel grade 1319* based on the composition provided by the manufacturer.

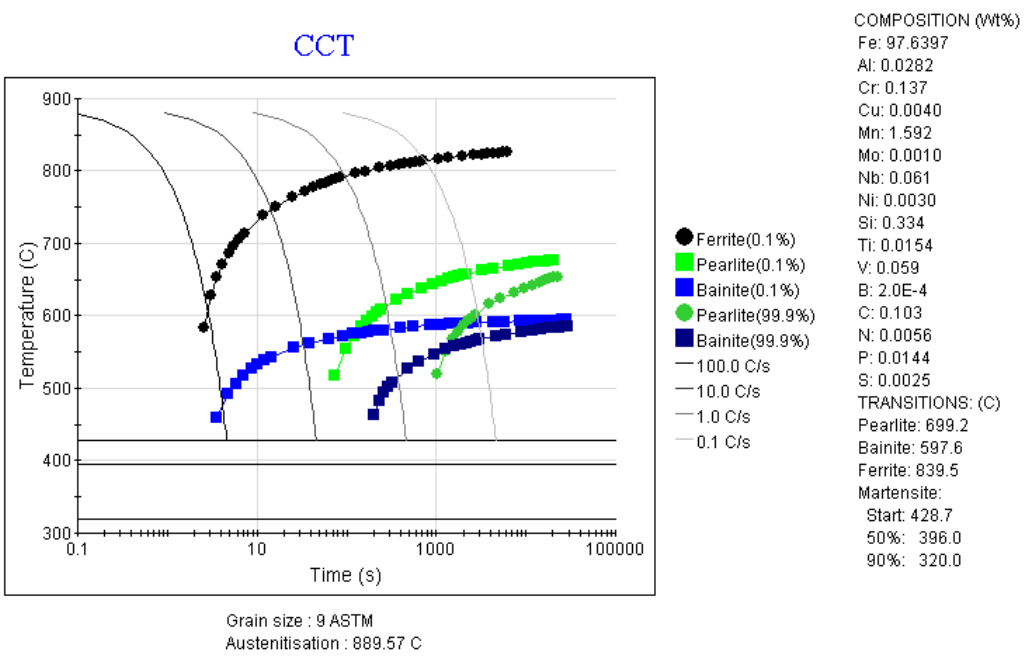

Figure 57 JMATPRO estimation for CCT diagram of Steel grade 1319* based on the composition provided by the manufacturer.

Higher austenitizing temperature increases the "equilibrium" austenite carbon content under equilibrium conditions. Therefore, the sample was heated 50 degrees or more above the

temperature predicted by JMATPRO to assure getting more homogenous single-phase austenite phase microstructure. The experimental data measured by thermocouples and recorded by the Lab view, were analyzed and plotted in excel file for each sample and $\gamma-\alpha$ phase transformation was investigated through in the range close to the estimated transformation temperature by JAMTPRO.

7.4 AIR COOLING EXPERIMENTS

The experiment procedure is a short austenization followed by normalizing. It is usually used to enhance the tensile strength of the steel. However, in this experiment, normalizing is used as a given rate for cooling the sample. Slabs in Table 9 were chosen to be cut in producing the samples for the air-cooling experiments.

Table 9 Slabs selected for producing samples for the air-cooling experiment.

Slabs used to produce the samples	Cooling method of the cast steel	AISI grade of the steel
160530-503 B cent	Chamber cooling	1319*
160530-103 A ext	Air cooling	1091*
160530-205 A cent	Air cooling	1010*

In this experiment, the sample's temperature reached 900 C after 1500 seconds and was kept for another 900 seconds to ensure homogenous temperature in the bulk material. ASME standard for normalizing by natural air is 1 hour per inch. Longer times may be required for

alloys containing elements that retard carbon diffusion in the austenite. It was observed that after 2 hours, all thermocouples reach room temperature consistent with the ASME standard.

7.4.1 Steel grade 1010*

The areas inside separated by the red square in Figure 58 are the NDT images of the sample for different layers 1 to 5 from top of the slab's surface.

Figure 59 is the plot of temperature versus time during heating the sample. Selecting a closer range around the temperature suggested by JMATPRO in Figure 60 exhibits the starting and ending of austenite formation during heating the sample above the existence of austenite as single phase in the texture. Using first derivative of the graph, the starting and ending of $\gamma-\alpha$ phase region can be recorded from the heating rate graph. Two straight lines with different trends in Figure 60 are used to find the single-phase portion of the curve. The graph in Figure 60 shows that in heating up the phase transformation, started at 722.2 ^{o}C and after 765.0 ^{o}C, the texture must have single-phase austenite.

Comparing the upper and lower portion of the graph in Figure 61-a and Figure 61-b show that the temperature of the middle thermocouple is closer to the interior one at the lower temperature while it has smaller deviation with the exterior one compared to its deviation to the interior thermocouple.

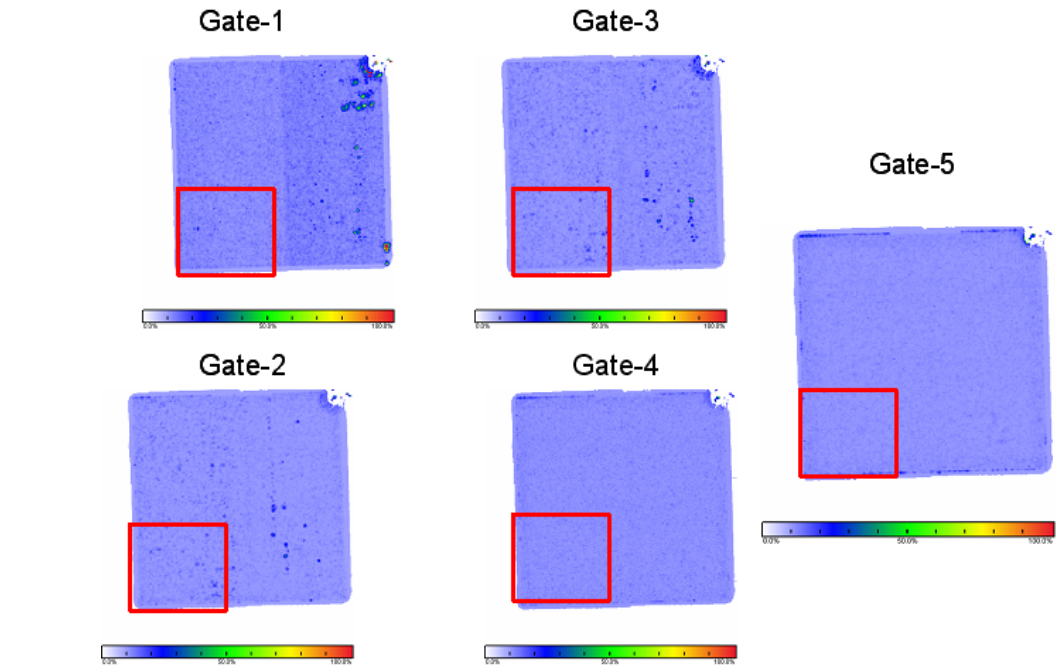

Figure 58 NDT images for five layers (gates) of 1010* grade steel from slab 160530-205 A center.

The cooling stage of the experiment starts after the hot furnace heating and austenization stages. Figure 62 shows the cooling rate of the middle thermocouple is closer to the exterior than interior with same proportion as the thermocouples distance from each other. A close look at the portion of the curve in Figure 63 around the isothermal reaction of phase transformation presents three different major slopes in the curve, which can be used for the computation of the starting and ending of the austenite transformation. From Figure 63 it can be extracted that phase transformation begins near 797 ^{o}C and all the austenite must disappear from the texture at temperatures below 764 ^{o}C.

The thermal ranges for supercritical, intercritical and subcritical in the cooling graph of the 1010* steel can be detected in the detailed sketch of the cooling curve in Figure 63. The high accuracy of R2 near 1 indicates the accuracy of the concluded bounded temperature for the solid-solid transformation. Figure 64 is the image of the sample after the experiment. A very thin

layer of corrosion was formed during the heating and cooling experiment which was easily removable from the sample.

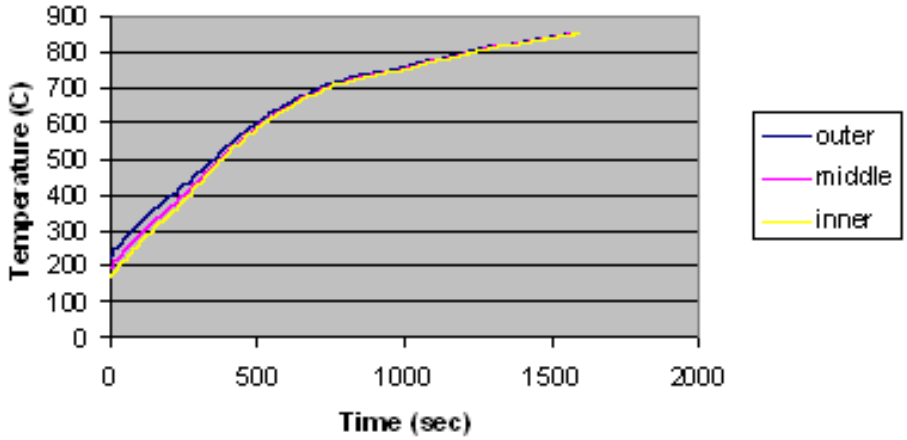

Figure 59 Heating rate graph of the 205-A-center sample (grade 1010*)

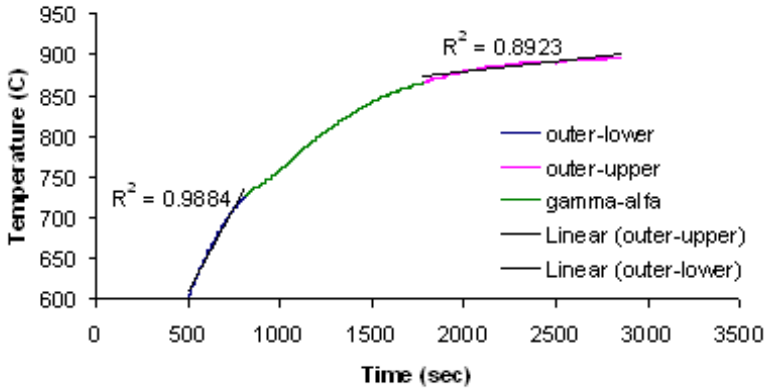

Figure 60 Starting and ending of phase $\alpha-\gamma$ transformation.

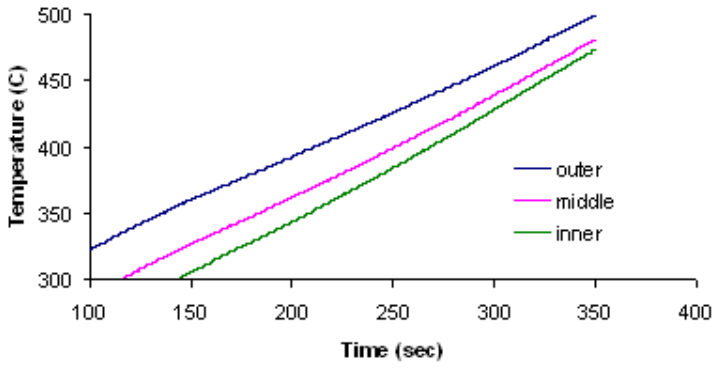

(a)

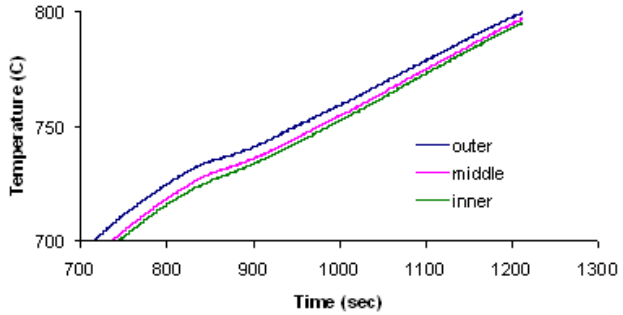

(b)

Figure 61 Comparison between rate of temperature through the thickness of the sample between (a) lower portion and (b) upper portion of the graph

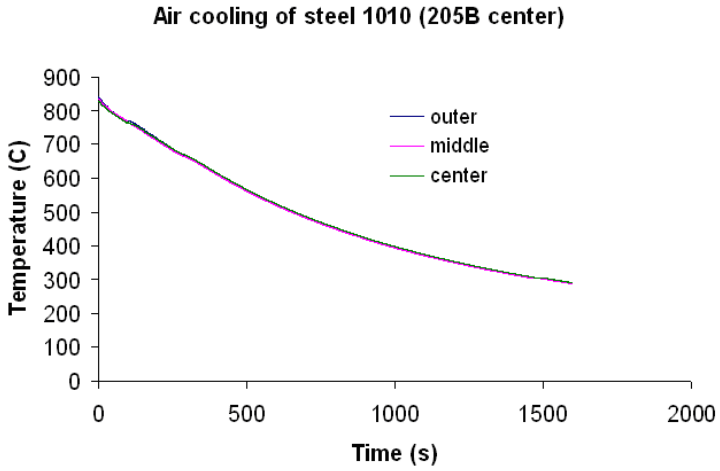

Figure 62 Cooling Rate graph related to air cooling of Steel 1010*.

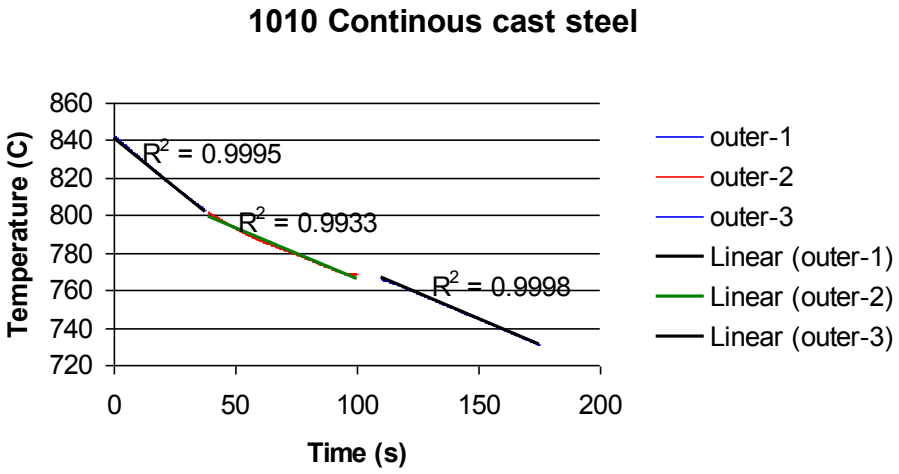

Figure 63 Change in the slope of major trend lines, shows the phase transformation period.

Figure 64 Image of the corrosion on the sample after experiment.

7.4.2 Steel grade 1091*

Figure 65 is the NDT images of the slab and portion of the slab cut to make the sample. The isothermal reaction of the phase transformation and completed temperature and time of phase transformation can be seen in the heating rate graph shown in Figure 66. Cooling rate at the first 1500 seconds portion of the cooling process where the isothermal reaction of γ–α phase transformation started and completed can be observed in Figure 67. It also gives the temperature range, for γ–α phase transformation, to be 730 ^{o}C to 647 ^{o}C in the cooling process of the sample

of steel grade 1091*. The corrosion files in this case were thicker and harder to remove compared to that of the 1010* steel. Figure 68 is an image of the sample after the experiment.

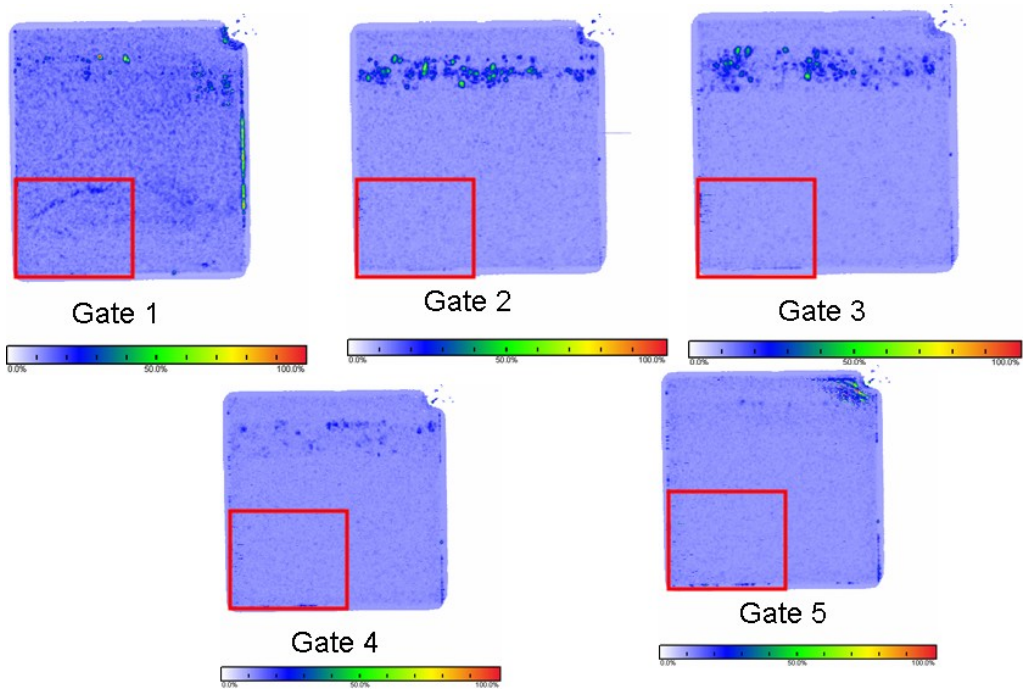

Figure 65 NDT results for texture images of 1-5 layers (gates) from top to bottom of the 103-A-center slab; the selected area is the portion cut to make the sample for experiment of steel AISI grade 1091*.

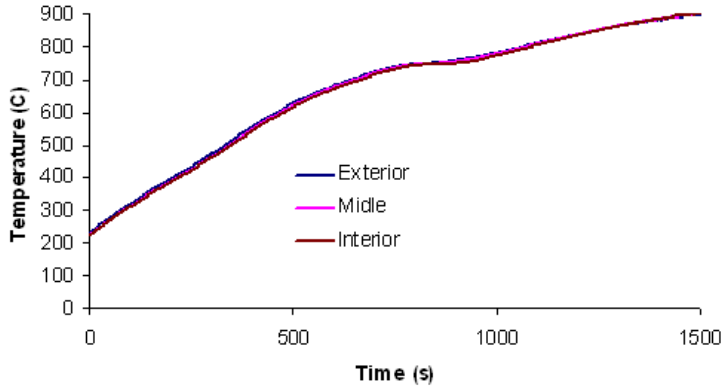

Figure 66 Heating rate graph of the 103-A external sample (grade 1091*).

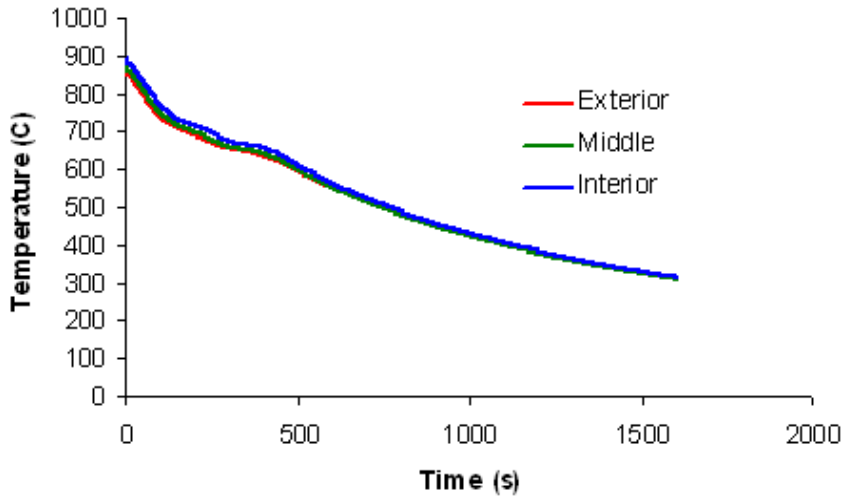

Figure 67 Cooling rate curve for grade 1091*.

Figure 68 Image of sample 1091* after 3 stages of the experiment.

7.4.3 Steel grade 1319*

A sample with the given sizes in Figure 47 is cut from slab 160530-503 B center. These NDT images of sample made from steel grade 1319*, unlike samples 1010* and 1091*, contained more anomalies, in the portion cut from the slab (Figure 69) in gates 3 and 4.

The heating rate graph and the first part of the cooling rate that included the complete phase transformation of austenite are shown in Figure 70 and Figure 71. The high change in the

slope of the curve in Figure 71occurs because of the $\gamma-\alpha$ phase transformation. Tracking of the slope changes in Figure 71 show that a range of between 748 C and 609 C can be considered for the phase transformation temperature range.

Figure 72 is the image of the sample after completing three stages. A long crack near the center plane of sample 1319* proved that the critical cooling rate to avoid formation of new defect in the microstructure for the steel grade with composition of AISI 1319* is slower than air cooling. The formation of the crack in 1319* may be explained based on the chemical composition of the 1319* steel and, especially, since it was the only slab cut from a chamber cooled, cast steel, and that has undergone a higher cooling rate in the laboratory cooling experiment.

According to Figure 73, the cooling rate at the center of the 1319* sample in the upper portion of the cooling curve is 1.2031 C/s and in the lower portion is 0.5046 C/s. The lower value for the starting austenite decomposition compared to that estimated by JMATPRO occurred because of the faster cooling rate compared to the calculated cooling rate of 1 C/s in the TTT and CCT diagrams for the JMATPRO estimation in addition to the computational error of the JMATPRO.

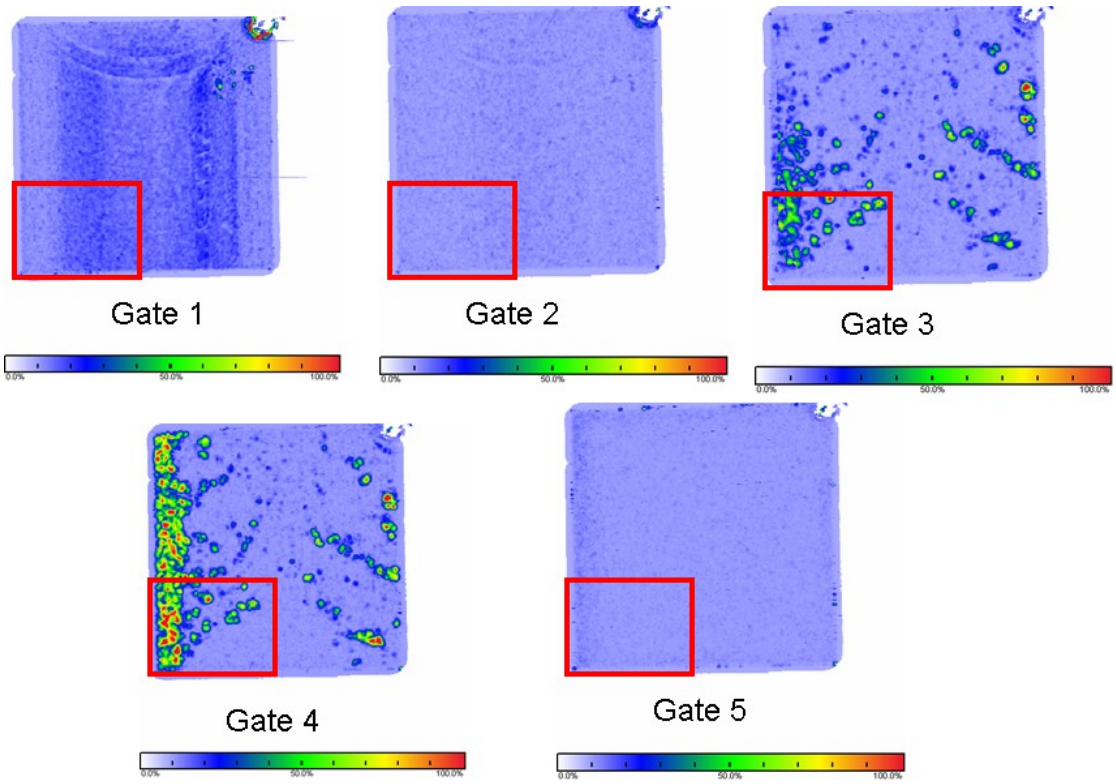

Figure 69 NDT results for texture images of 1-5 layers (gates) from top to bottom of the 160530-503 B center slab; the selected area is the portion cut to make the sample for experiment of steel AISI grade 1319*.

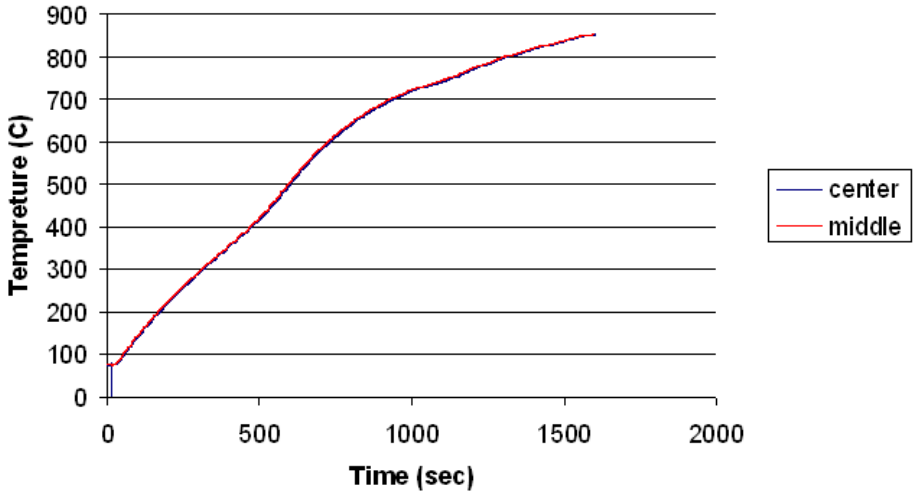

Figure 70 Heating rate graph of the 160530-503 B center sample (grade 1319*).

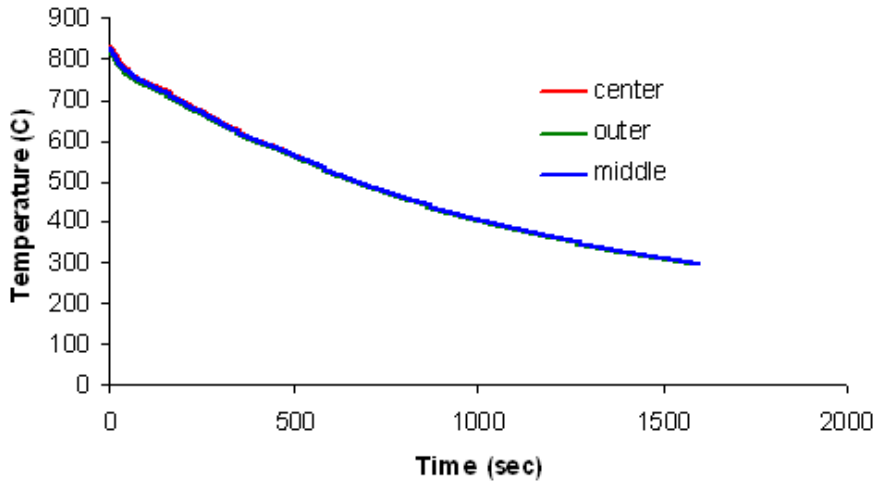

Figure 71 Cooling rate curve around the phase transformation for grade 1319*.

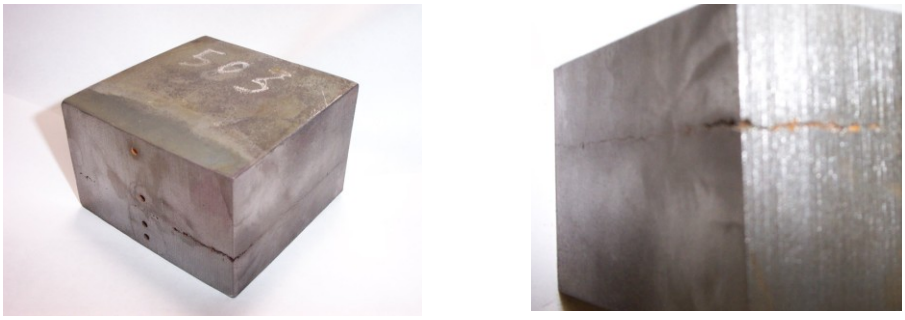

Figure 72 Image of sample 1319* after 3 stages of the experiment.

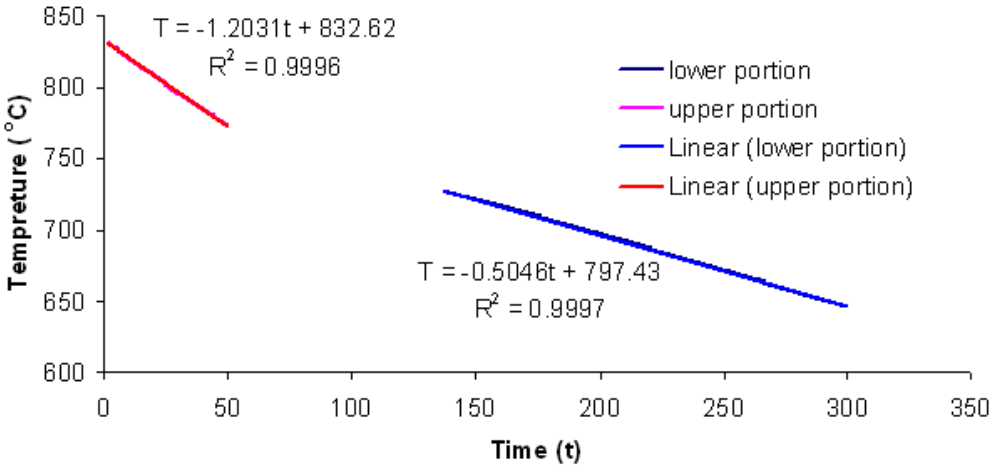

Figure 73 Trend line of the cooling curve of the sample of grade steel 1319* recorded by the thermocouple attached to the center plane of the sample shows the cooling rate before and after eutectoid transformation.

8.0 FEM ALGORITHM AND VERIFICATION

8.1 THE NUMERICAL COMPUTATIONAL ALGORITHM

To achieve the main objective of this dissertation, an FEM algorithm with ANSYS codes was developed to simulate cooling as-cast steel from supercritical, intercritical, and subcritical temperature ranges. The model should be able to produce the thermodynamic stresses generated by thermal strain and phase transformation deformation for any grade of steel. The model is applicable for any type of cast steel (slab, billet and bloom, bar, etc) and adaptable for any method of cooling (unidirectional or multidirectional). Cooling with any cooling agent can be simulated with the algorithm in an ideal case (no bubble formation, homogenous constant temperature, etc.). The phase transformation of the steel in the algorithm can be based on the CCT diagram obtained from real time-temperature-transformation experiments for steel with any chemical composition. This makes the model quasi-real simulation. Furthermore, correction factors for the computation parameters and FEM variables provide adjusting tools for different simulation case to increase the precision of the results in industry.

Every crystal unit cell can be considered as an element in the FEM simulation, and then the nodes at nodal sites of the element have the same role as atoms in the crystal. Interaction of atoms and metallurgical behavior of unit cells in a crystal are more complicated than the model considered here. To simplify the model, many factors are neglected here. In this model, the heat

transfer due to three modes of the heat transferring, conduction, convection and radiation, are considered. The material is assumed to be perfectly isotropic, which for heat treated multi crystal material is a reliable assumption. Heat treatment eliminates unique directions of grains.

It is important to note that the computation time was not the same as real time in the cooling experiment. The relation between real time in the CCT diagram and computational time was set through a number of time steps per second. This value was set in a time correction factor, (TCF), whose value is a function of different factors of the steel sample microstructure. Some of these factors are composition, size of the sample of the model, method of building grain boundaries, meshing size and type of elements used in the model as well as microstructure information such as grain size, quantity and distribution of anomalies in the microstructure and degree of homogeneity. Therefore, the value of the TCF should be set experimentally to employ the phase transformation in the model accurately. The proposed algorithm builds the model based on the chosen type of the steel composition from the material library and steel product geometry library. Then it applies the computational parameters and FEM parameters to the model. The block specified for the decision of phase transformation decides the necessity of the phase transformation and furnishes the information for data sorting to introduce the phase configuration after each load step. The model was designed to be controlled with the volume fraction of phases presented in the final microstructure after cooling to room temperature to increase the accuracy of the stress analysis. The detail of the algorithm can be seen in the Figure 74.

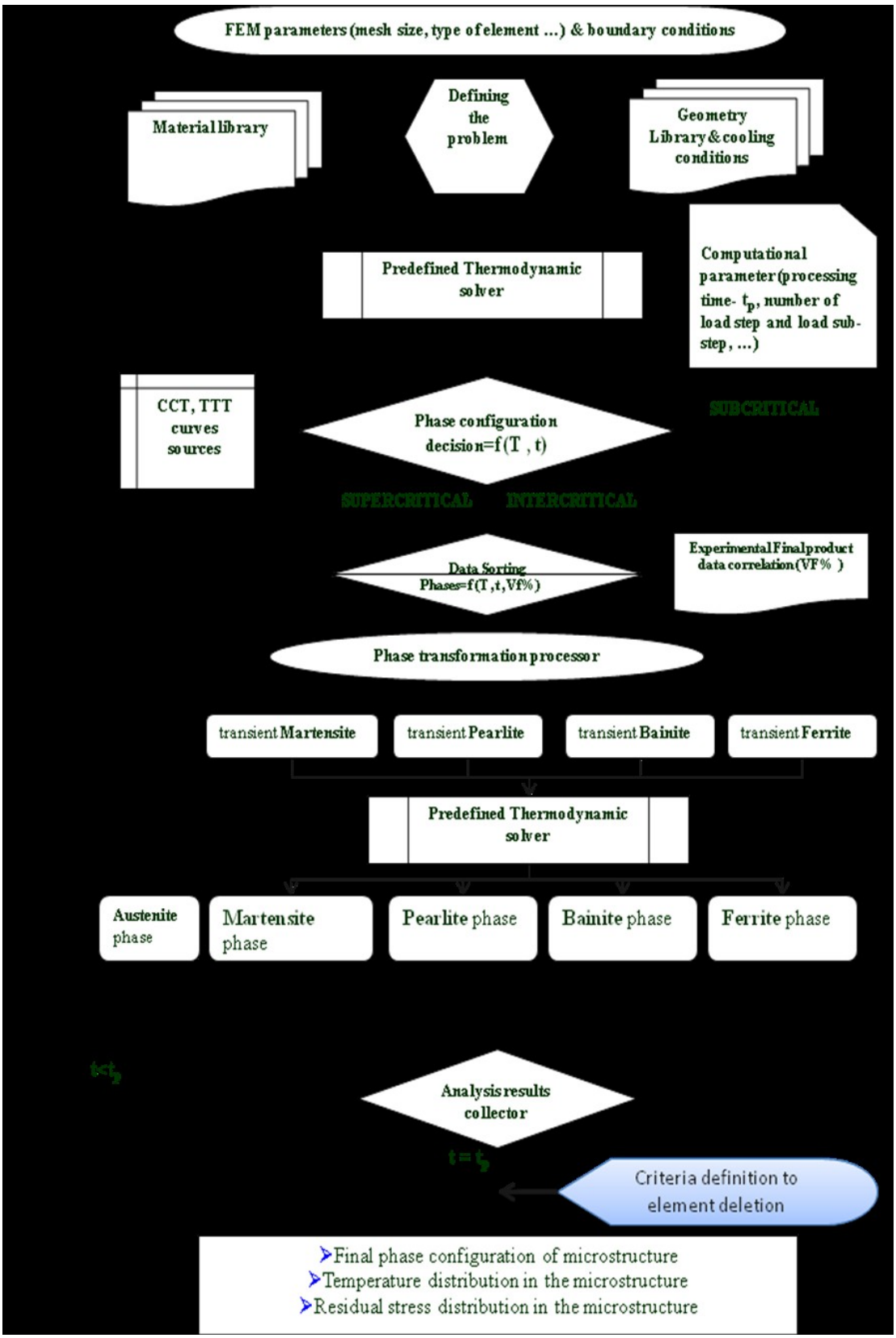

Figure 74 The flow chart of the FEM algorithm proposed to simulate cooling of the as-cast steel slab.

The solid-solid phase transformation is imposed to the algorithm via a transient phase corresponding to each austenite phase transformation products. The structure deformation within the element due to the solid-solid transformation carries out by introducing thermo-elastic strain into the elements subjected to the phase transformation in an isothermal condition. The nodal and element outcomes of the proposed algorithm in the ANSYS provide the final phase configuration of the microstructure and thermal distributions and accumulation stress concentration zones. Thereby, the results can mark the vulnerable region to the formation of microcracks or the growth of flaws.

ANSYS Parametric Design Language (APDL) is utilized to introduce the CCT diagram into the FEM code and couple the thermal and dynamic analysis. A plane 223 element is used for the thermo-elastic analysis during cooling. As it was mentioned, it has eight nodes with up to four degrees of freedom per node. The qualitative and quantitative information about the elements in the microstructures of each sample can give the approximate phase transformation temperature as a function of alloy content, time and temperature.

The CCT diagram furnishes this information for the model to be able to simulate the cooling of a steel slab with different cooling rates for given compositions. JMATPRO software or experimental results provides the CCT diagram of the given steel. Therefore, the model can simulate both a simple cooling curve and a complicated cooling path process for a wide range of different types of steel. If the final product of the cooling is known, the program can be set to mimic the experimental data for final volume fractions of different phases in the microstructure. Nevertheless, the priority of phase transformation is determined by the CCT diagram introduced into the program. The volume fraction phases presented in the microstructure after transformation of austenite to the other phases follow the unity percentage rule.

8.2 GRAIN BOUNDARY DEFINITION METHODS

Understanding the mechanism of crack propagation in material is crucial in many industrial fields such as aeronautical engineering, material sciences and geophysics and etc. Crack propagation can be simplified by introducing new surfaces within the solid material through a dynamic process which results in changing geometry and topology of the model [338]. Crack develop mainly at the grain boundaries, therefore the properties of the grain boundaries play an important role in the formation of flaws and microcracks due to accumulation of residual stress in the steel microstructure.

Grain boundary geometry, commonly referred to misorientation, is a terminology to define the crystallographic relationship between the grains, which are adjacent to each other in the polycrystalline microstructure [339]. The property of the grain boundary depends on the free volume at the boundary and includes energy, diffusivity, segregation, mobility, resistivity, cavitations' corrosion, embrittlement, fracture migration, precipitation, sliding and other phenomena attributed to mechanical and chemical characteristics of the grain boundary such as reaction to the etching agent [340].

The cohesive forces which keep the grains next to each other are considered as strength of the grain boundary. This strength is a grain boundary characteristic which depends on many factors including the composition of steel, phases of grains sharing same grain boundary and the presence of impurity elements in the grains, properties of grains and etc. The grain boundary strength can be changed by the segregation of impurities of grains at the common grain boundary. Kameda and McMahon [341] studied the effect of the impurities of Sb, Sn and P on intergranular cohesion. Their work showed that maximum segregation impurities are at grain

boundaries and the distribution of the facet normal to the maximum tensile stress is one per grain.

Seah and Hondros [342] gave the relationship between the equilibrium segregation and temperature of the binary system. They showed the concentration of segregated atoms is related to the free energy of segregation and segregating atom distribution at un-segregated and binary regions. Non equilibrium segregation is a kinetics process in the quenching process from high solution treatment temperature. The source of the non equilibrium segregation is the formation of solute vacancy complexes from super saturated vacancies and solute atoms ([343]- [346]).

Diffusion of these complexes to the grain boundaries as the sink of the vacancies is the boundary segregation of the impurities. The boundary segregation is sensitive to the cooling rate such that it reaches its maximum value at a critical cooling rate. Any cooling rate higher than the critical one result in dominating the boundary segregation and cooling rate slower than the critical cooling rate causes the desegregation of impurities from the boundaries [347].

Non equilibrium segregation of Sn occurs along interfaces between the pro-eutectoid ferrite and austenite and along austenite grain boundaries which reduces the grain boundary strength ([348]-[351]). Yuan et al. [347], investigated the effect of critical cooling rate in the segregation of impurities such as Sn. Fulker [352] introduced a model to predict the segregation of boron, aluminum and titanium to grain boundaries in austenitic steels. He thought that non-equilibrium segregation depends on the binding energy between impurity atoms and vacancies as well as the temperature range of fast cooling. This dependency is more significant for cooling from high temperature where the steel matrix temperature is above the temperature at which diffusion becomes more significant. The non equilibrium segregation occurs because of misfit between the impurity atoms and matrix and the preferential in-plane bonding between non-

metallic and metallic elements compared to the trans-plane bonding Therefore, the atomic size of an impurity and bonding energies in a binary system influence the segregation parameters.

In general, non-equilibrium segregation is blamed for reducing the strength of the grain boundary. Tin is known to increase the tendency of surface cracking in the continuous cast slab between 700-900 ^{o}C [353]. However, segregation does not always reduce the grain boundary strength. The best example of it is segregation of carbon to the grain boundaries which increases the strength of the grain boundary ([354],[355]). Segregation of Ti in an iron grain containing Ni and Sb enhances the strength of the grain against embrittling [356]. Therefore, the strength of the grain boundary is defined by the combination of the cohesive stresses at the grain boundary and its deviation due to the non equilibrium segregation.

Proper method to define grain boundary is the major problem of the numerical models presented in the literature. In the numerical model presented in this work, the defect formation is investigated in relationship with the properties defined for the grain boundary of the microstructure. The interaction between contact surfaces (e.g. adjacent phases or inclusions and steel matrix) is a contact problem and, like all other contact problems, is highly nonlinear and requires significant computer resources to solve. The solution may converge with difficultly after a number of iterations or totally diverge or contact surfaces may overlap each other in a largely unpredictable and abrupt manner depending on the loads, material, boundary conditions, and other factors [312]. Four different methods to define the grain interfaces are introduced to be used in the models built by the proposed FEM algorithm. These methods are discussed below.

Four methods of intergranular definition can be applied to the models. These methods are rendered to the grain boundaries by interfaces formed from glued grains, thin layer bodies with thermodynamic properties, contact-target element method, and interfacial cohesive zone method.

Each method of creation of a grain boundary can be dependent or independent of temperature. The two latest ones are implemented in the model with two groups of the element types, contact elements and interface elements. These techniques were extensively explained in [312]. In the cohesive zone technique, the intergranular cohesive force materials change with temperature exponentially [357] and the grain boundary has linear softening characterized by maximum traction coupled with maximum separation or critical energy release rate [358].

The contact element technique is a master and slave contact method implemented to build the forces acting at the interface. The interfacial separation in delaminating with contact elements or debonding behavior is a function of contact gap or penetration and tangential slip distance. The bonding energy in this method is set by stiffness of the contact surfaces. All the reaction forces are accumulated in the specified node assumed to be the more critical point at the interface as a result of stress intensity. This point is called the pilot node and the debonding starts from this point and it then develops along the interface. The thermodynamic communications between surfaces initially in contact cease after debonding of the surfaces. Contact element is a 2 D three node surface to surface contact applicable to solid elements with mid-side nodes for structural analysis coupled with a contact field. It has three degrees of freedom (DOF) at each node, translations in the nodal x and y directions as well as temperature, with optional characteristics of standard contact behavior and Gaussian points' calculation.

The ANSYS elements used for introducing contact and target zones in these models are CONTA172 and TARGE169. The element in meshing of the contact-target models has eight nodes with up to four degrees of freedom per node possessing thermal expansion, structural-thermal capabilities in dynamic analyses. The constants of these elements set the properties of the contact zone.

The detailed description of these constants can be focused in [312]. The main challenge in these techniques, in addition to those mentioned, is that all thermodynamic exchange information between the debonded contact surfaces is stopped after the gap between the contact surfaces gets larger than a critical value.

An alternative method to model the interface bonding is by adopting softening relationships between traction and the separation. This technique introduces the cohesive zone by interface elements. The adhesion forces at the interface are represented with a special set of interface elements with properties to characterize the constitutive behavior of the interface. The properties specified for the element and material model define the traction acting on the interface and the corresponding interfacial separation by adopting a softening relationship at interface surfaces in which fracture energy governs the behavior of breaking apart the surfaces at the debonding interface.

The interface element, INTER202, used for the cohesive method simulations, is a 2D structural element defined by four nodes having two degrees of freedom at each node, translations in the nodal x and y directions with plasticity, creep, swelling, stress stiffening, large deflection, and large strain capabilities [312]. This method can be implemented only for the structural analyses between parts, which share coincident nodes within elements with only displacement degrees of freedom. Hence, parts can be meshed only with structural elements having only three displacement degrees of freedom in the X, Y and Z axes. Because of this disadvantage of the method in the current ANSYS (version 11.0), it cannot be a good tool in solving problems related to temperature gradient boundary conditions.

In the algorithm presented in this dissertation, the critical adhesion among the grains before failure is assumed to be constant or variable as a function of temperature, although the

adhesion force at the intergranular sites depends on the method of the grain boundary definition. The main problem in simulation of the contact mechanism is the control of the region where the defined properties are effective. All the surfaces with its FEM feature, i.e., nodes and elements, beyond this region, do not have the ability to possess the properties and, consequently, a model cannot present the void or fracture simulation properly or crash the simulation due to the solution divergence in numerical calculation. Therefore, the method of deactivation of the elements subjected to the stresses beyond the critical intergranular adhesion force was deployed in the algorithm after completion of the simulation, instead.

8.3 VERIFICATION OF THE SINGLE PHASE COOLING MODEL

The FEM program was used to model the cooling experiment of the 1010* steel grade, explained in the cooling experiment of the as-cast steel. Therefore, the model was built to have the dimension of 75 mm x75 mm and 50 mm thickness to compare the analytically determined results with the results of the laboratory cooling experiment. The initial temperature was considered to be 1100 ^{o}C to give the model the same thermal condition as the sample tested in the cooling experiment.

The model was a single phase homogenous, isotropic and it was able to capture the thermodynamic changes due to thermal contraction without considering the strains generated by the phase transformation. The model simplifies the whole bulk material as one crystal without any precipitations, inclusions or voids.

Table 10 is properties of steel grade 1010* extracted from a several previously published papers on this type of steel ([288],[290],[359]-[364]).

Table 10 Experimental properties of steel grade 1010*.

Properties		Conditions	
		T (°C)	Treatment
Density (×1000 kg/m3)	7.7-8.03	25	
Poisson's Ratio	0.27-0.30	25	
Elastic Modulus (GPa)	190-210	25	
Tensile Strength (Mpa)	365	25	cold drawn
Yield Strength (Mpa)	305		(round bar (19-
Elongation (%)	20		32 mm)) more
Reduction in Area (%)	40		
Hardness (HB)	105	25	cold drawn
			(round bar (19-
			32 mm)) more
Thermal Expansion (10^{-6}/ºC)	15	0-700 more	annealed
Thermal Conductivity (W/m-K)	65.2	0 more	
Specific Heat (J/kg-K)	450	50-100 more	

The film or convection coefficient in the model was 25 $Wm^{-2}K^{-1}$ with the constant emmisitivity coefficient of 0.8. Figure 75 is the schematic of the model. The analytical results were recorded for the points in the model with the same depth from the top surface as the location of the thermocouples in the laboratory cooling tests.

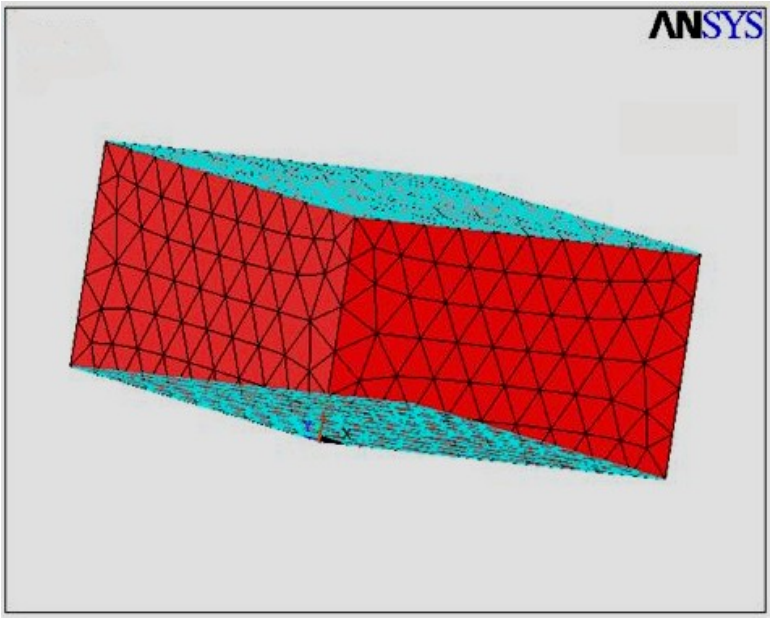

Figure 75 The model of the cooling experiment in the ANSYS.

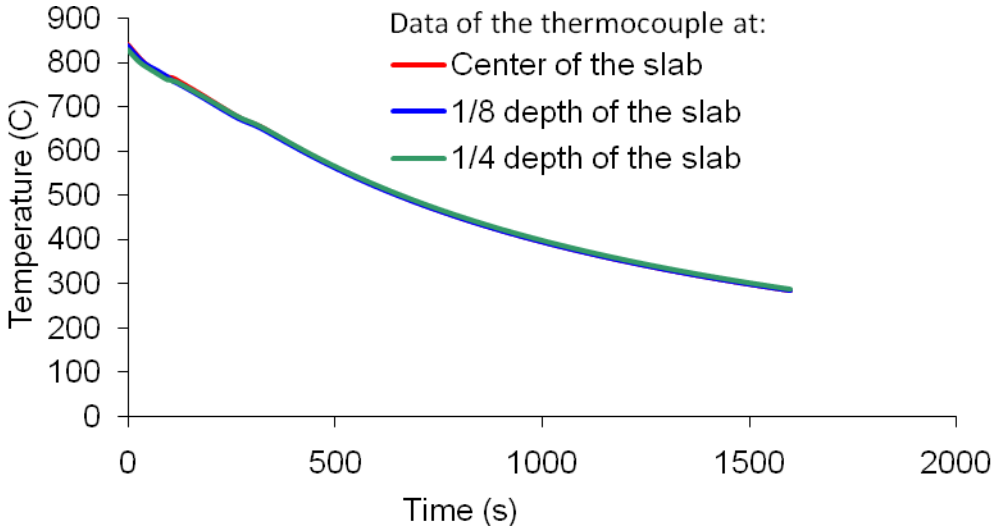

Figure 76 Cooling rate graph related to air cooling of Steel 1010*.

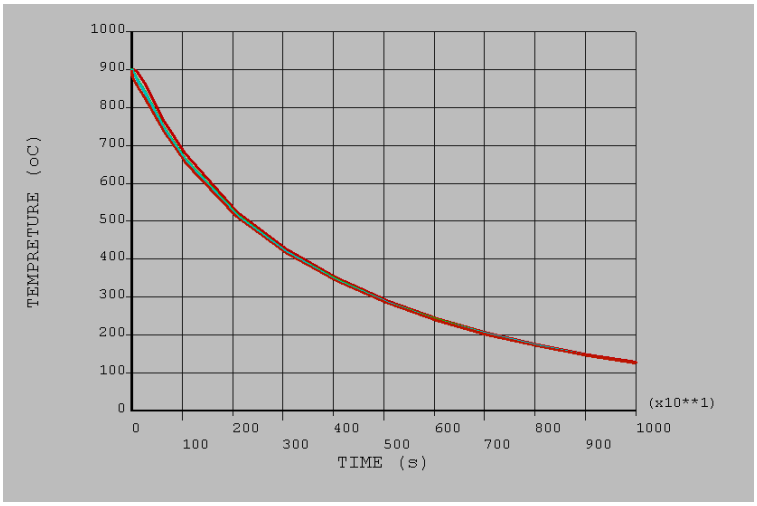

Figure 77 The through thickness cooling rate of sample 1010* in the cooling model of the sample.

Figure 76 and Figure 77 contain the cooling rate results for the laboratory cooling slab tested in this dissertation and analytical FEM computation. Comparing the results observed in the Figure 76 and Figure 77, shows similar trends and gives a good correlation between numerical results computed by FEM and obtained from experimental results.

A more complicated simulation was modeled to show the stress accumulation due to strain introduced to the microstructure using the proposed algorithm in Figure 74. Then the results were compared with the crack formation in the steel grade 1010* in the cooling test described in the experimental cooling section. It can be seen from Figure 78 that the stress concentration plane is the more vulnerable sample plate for the formation of the defect. Figure 78 is evidence that the proposed algorithm can give valuable information about the location of the formation of the defect as well as other information about the microstructure explained above, if the input information and adjusting correction factors are defined accurately.

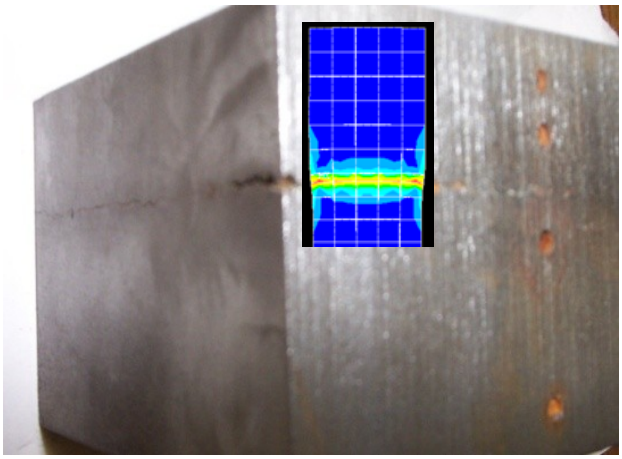

Figure 78 Comparison of the defect formation in the laboratory cooing test sample with the result of the model simulated by the proposed algorithm.

9.0 RESULTS AND DISCUSSION

9.1 EFFECT OF THE PHASE TRANSFORMATION IN THE THERMALLY INDUCED STRAIN

The stress analysis of stress generation due to a cooling process and estimation of phase transformation was conducted to study the effect of the rate of cooling in stored residual stresses in the microstructural configuration. The thermodynamic strain method, which is embedded in the proposed algorithm, increases the accuracy of the computation of the strain induced by the solid-solid phase transformation in comparison to the superposition method for unit cell structure change since the solid-solid phase transformation affects the temperature distribution in the model as well.

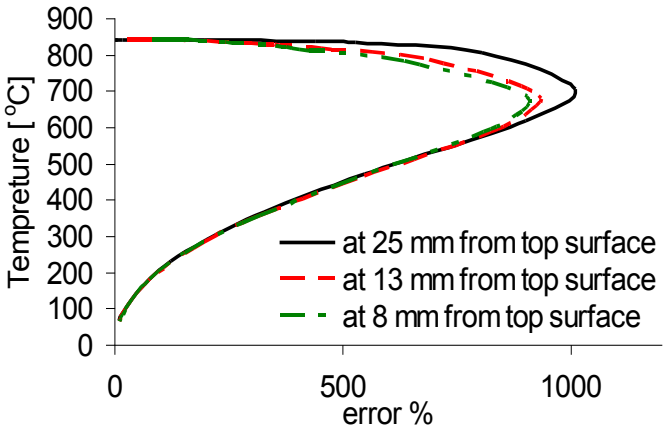

Figure 79 Error percentage of temperature of both sample and the model during the cooling process at a symmetric plane through thickness at different distances from the top surface.

A comparison of temperature variation during the cooling process between laboratory experiments and the FEM model without phase transformation in Figure 79 shows that the percentage error of the numerical computation increases at the phase transformation temperature range.

9.2 INVESTIGATION OF THE INTERACTION OF THE STEEL'S PHASES DURING COOLING

Adopting the proposed algorithm, the FEM model presented in this section is deployed to simulate the cooling of steel grade 1010* with the composition and the corresponding phase transformation based on the CCT diagram in Figure 80. Rectangular models with dimension of 3 in 15 mm were applied to study the stress concentration of the different phases with the microstructure composed of one or two phases produced during cooling from the supercritical temperature. The possible combinations of the phases at the interface under study are listed in Figure 81.

All the models were initially stress free and at the super critical temperature range. The cycle of microstructure scanning and the restating of the new microstructural configuration after each load step, embedded in the program ,introduced stress concentration zones at the two phase boundaries formed after phase transformation.

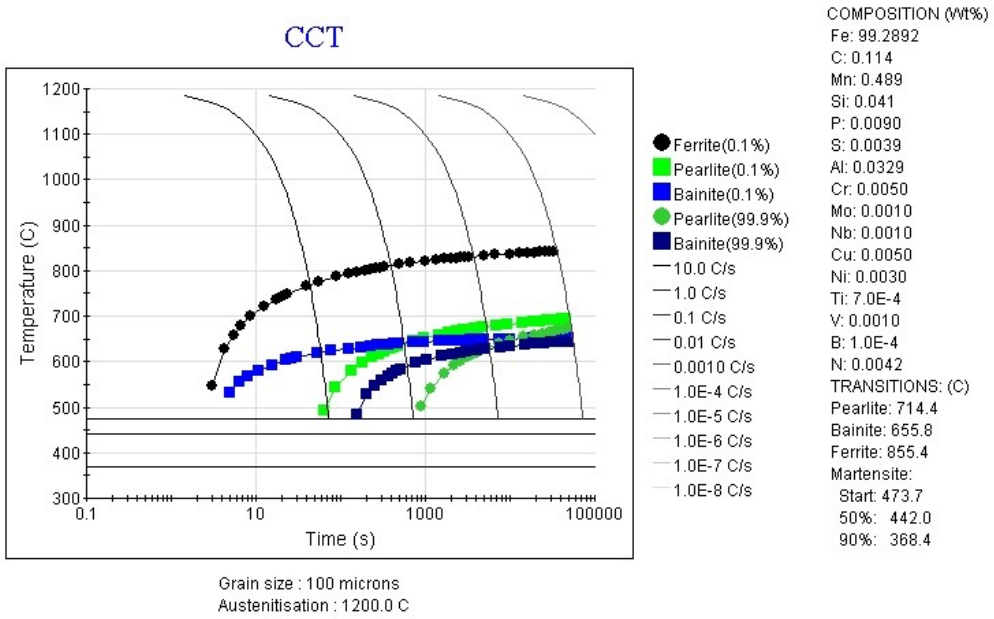

Figure 80 CCT diagram for steel 1010* used in the simulation.

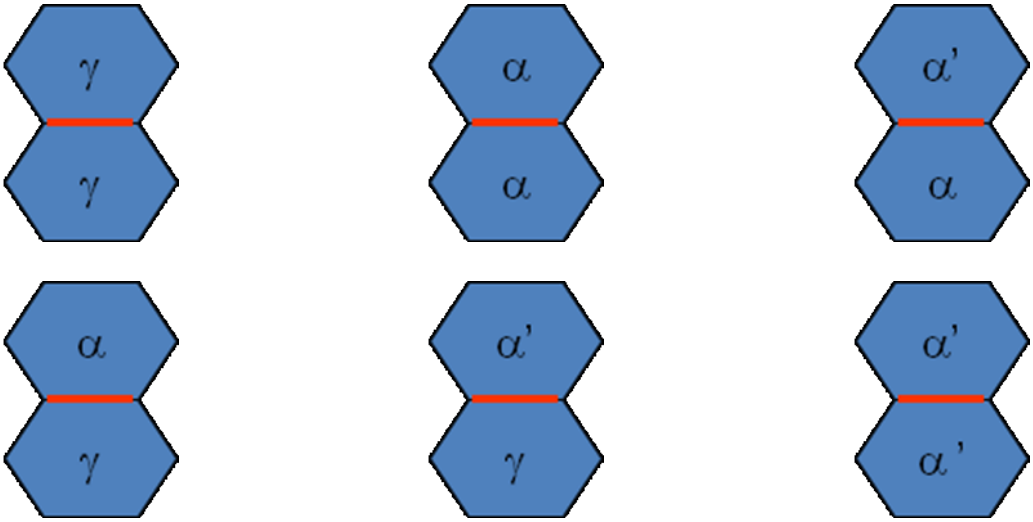

Figure 81 Interface of two phases of different combinations of austenite (γ), ferrite (α) and martensite (α').

In the models, the phase transformation of the steel is based on the CCT diagram for average grain size of 1000 μm for steel grade 1010* quenched with different rates from 1200 ^{o}C. The heat is transferred from the top surface of a 2-D model with no heat exchange from other surfaces with the environment (i.e. adiabatic thermal conditions). The model is constrained from

the bottom. It is to simulate the half section of a 30 mm thick slab, using symmetric conditions, cooling using cooling agents from top and bottom surfaces in an ideal case (no bubble formation, homogenous constant temperature, etc.). Cooling rate can be controlled with three different methods as follows: the applied convection film coefficient, environment temperature and time parameters of the FEM computation. In these simulations, in order to have better control over changing the rate of cooling, the latter method was used. The boundary conditions applied to the models are shown in the Figure 82.

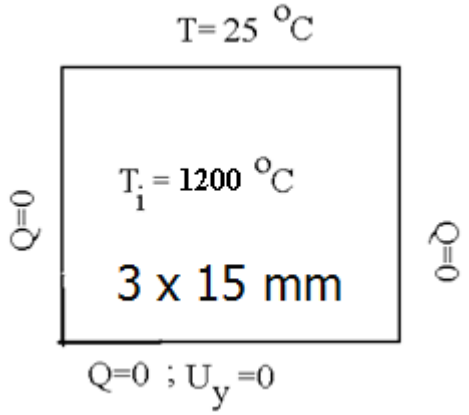

Figure 82 Boundary conditions of the models used for studying the stress accumulation at the interface.

The material properties of all phase products formed after cooling steel grade 1010* were obtained from JMATPRO. All the material properties of each phase are linearly temperature dependent between the two temperatures show in Table 11. The material is assumed to be perfectly isotropic, which for a polycrystalline microstructure is a reliable assumption. The grain boundary is assumed to be slightly softer than the grains based only on the density of the non lattice site atoms compared to the unit cell atoms and the presence of the voids within the grain boundaries without considering grain boundary hardening and participation of alloy elements at

the grain boundaries. It is only to show the effect of the grain boundaries thermodynamic properties in the accumulation of the stress in the microstructure during cooling.

Table 11 Material properties of microstructural phases appearing in the steel grade 1010* cooled from 1200 °C with different cooling rates.

Steel Phase	Temperature [°C]	Instantaneous coefficients of thermal expansion [1/K] × 10^{-6}	Elastic modulus [GPa]	Specific heat [J/(kg.K)] × 10^{3}	Thermal conductivities [W/(m.K)]	Poisson ratio	Density [kg/m3]
Austenite	1200	26	100	0.65	32	0.36	7450
	714.4	22	155	0.60	27	0.32	7740
Ferrite	855.4	15.8	135	0.72	27	0.29	7700
	25	12	210	0.44	51	0.31	7880
Martensite	473.7	17	160	0.60	22	0.32	7760
	25	12	210	0.44	51	0.29	7820
Pearlite	714.4	16.2	165	0.85	34	0.31	7680
	25	12	210	0.45	51	0.29	7845
Bainite	655.8	16	165	0.8	34	0.31	7760
	25	12	210	0.45	51	0.29	7880

The volume fraction of the phases at room temperature can be controlled in the model to have a phase combination close to experimental results for a defined cooling rate of any specific

steel composition. The film or convection coefficient in the model was 500 $Wm^{-2}K^{-1}$. The emmisitivity coefficient is considered to be 0.8 for reddish to grey color of the sample from 1200^{o}C to room temperature. The grains are represented by body entity in the models and elements within the body are unit cells in the grains. The grain diameters are considered to be 1000 μm in the model. The grains are homogenous and isotropic without any dislocations or any type of anomalies. The interaction between contact grains is a contact problem and, like all other contact problems, is highly nonlinear and requires significant computer resources to resolve. The solution may converge after a number of iterations or totally diverge or contact surfaces may overlap each other in a largely unpredictable and abrupt manner, depending on the loads, material, boundary conditions, and other factors [365]. The grain boundaries are defined as atoms in non-lattice sites. In this model, the grain boundaries were built as thin layer bodies at grain interfaces with the material properties different than the material properties of the grain. The material properties of the grain boundaries in the model are close to the material properties of the phases of adjacent grains before and after phase transformation.

The grains and grain boundaries are rectangular bodies meshed with quadrilateral-shaped elements or hexagonal bodies meshed with triangular shaped elements. All bodies are glued together to provide a homogenous model without discontinuity. However, the interaction of atoms and the metallurgical behavior of unit cells in the crystal are more complicated than the model considered here. The crystal structures are the same for different phases but their material properties are modified as a function of time and temperature while they are transformed to different phases as a result of the cooling process. The volumetric changes of unit cells are implemented via a transient phase with thermal expansion properties in the cooling process at the corresponding phase transformation temperature.

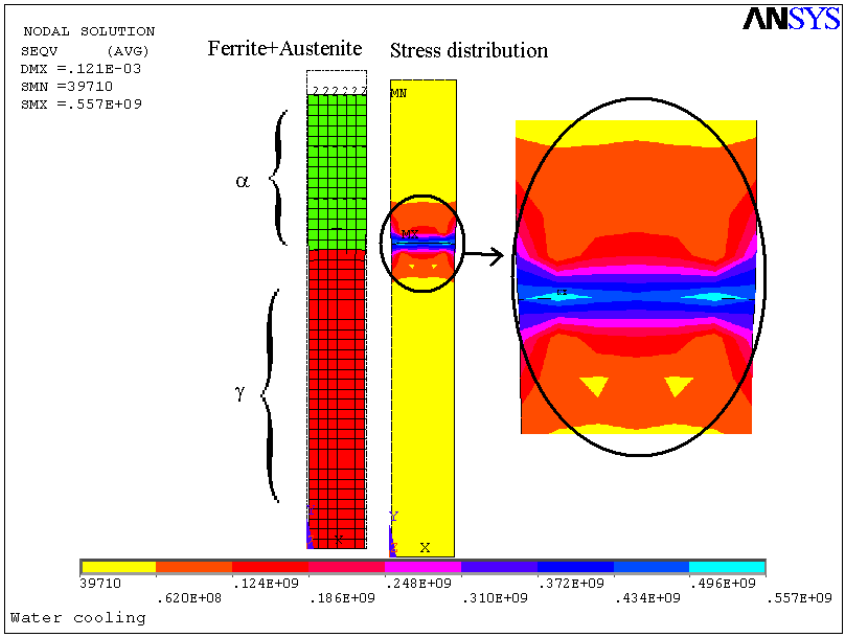

(a) Stress distribution (α+γ phases)

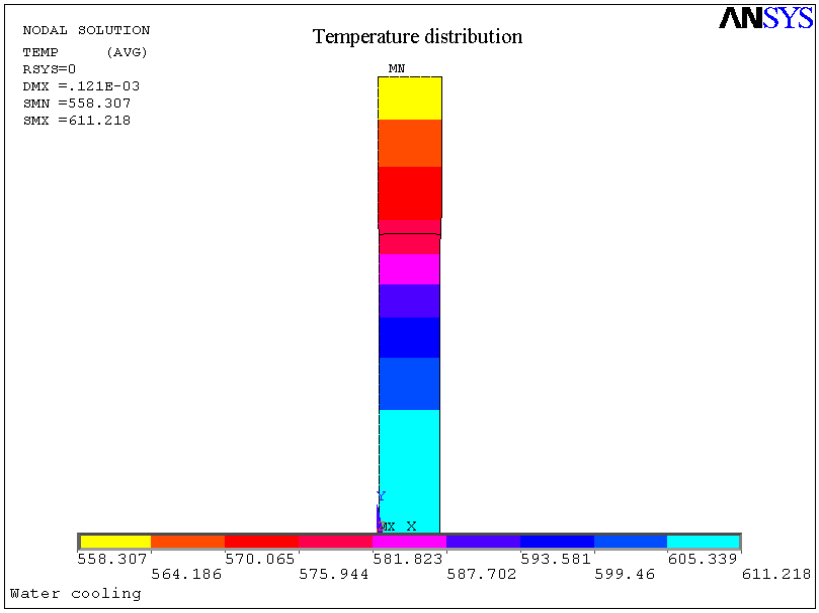

(b) Temperature distribution (α+γ phases)

Figure 83 Rectangular grain model with no grain boundary at the grain interfaces with a two phase microstructural configuration state resulting from austenite to ferrite phase transformation during cooling; (a) stress distribution, (b) temperature distribution

All bodies in the models have a homogenous microstructure without any discontinuity. Solidification processes and other intermediate steel manufacturing processes store residual stresses in the cast steel. However, in the simulations presented in this paper, all models were in the neutral pre-stress state. The program scans the time-temperature phase configuration after each load step and reintroduces the phase configuration of the microstructure based on the data extracted from the CCT diagram. Results presented in Figure 83 are for cooling and phase transformation simulation for a model composed of many grains with rectangular shape and glued to each other. Thus, interface was not defined between the grains and the grains in the models interact with each other homogenously. Figure 83 shows the stress (Figure 83a) and thermal distributions (Figure 83b) during austenite (γ) phase to ferrite (α) phase transformation resulting from the accelerated cooling process. The maximum stress concentration in the bulk material is around the region of two phase boundaries (see Figure 83a). The phase distribution next to the stress distribution results in Figure 83(a) provides the evidence of the formation of accumulation of residual stress at the interface of the γ phase with the α phase.

Figure 84 shows the thermal and stress distribution within the microstructure after completion of the γ to α phase transformation. It can be observed from Figure 84 that the high stress concentration at the former boundary of the γ phase to α phase is maintained in the microstructure. The number of similar simulations reveals that the depth of the formation of high stress concentration is a function of the numerical calculation time, the time step, size factor of the model, shape of the grains, and the properties of grains and their interactions with each other at the grain boundaries. An example of the effect of these factors on the formation of high residual stress bands during accelerated cooling can be observed in Figure 85. The grains in the simulation presented in Figure 85 are hexagonal with interfacial layers as grain boundaries at the

interface between grains adjacent to each other. It can be seen that the γ to α phase transformation has created two bands of stress concentration in the microstructure with the maximum stress concentration occurring at the two phase interface. Figure 86 and Figure 87 present the results of the simulation of quenching of the model. In these models, the γ phase is transformed to the martensite (α') phase. While Figure 86 shows the results of the simulation for a double phase microstructure with γ and α' phases, Figure 87 is the microstructural configuration after completion of the phase transformation. The effect of phase transformation at the inter-phase boundary region can be observed in these simulations, as well. Both models are designed with a wider size to demonstrate, better, the occurrence of the bulge due to γ to α' phase transformation.

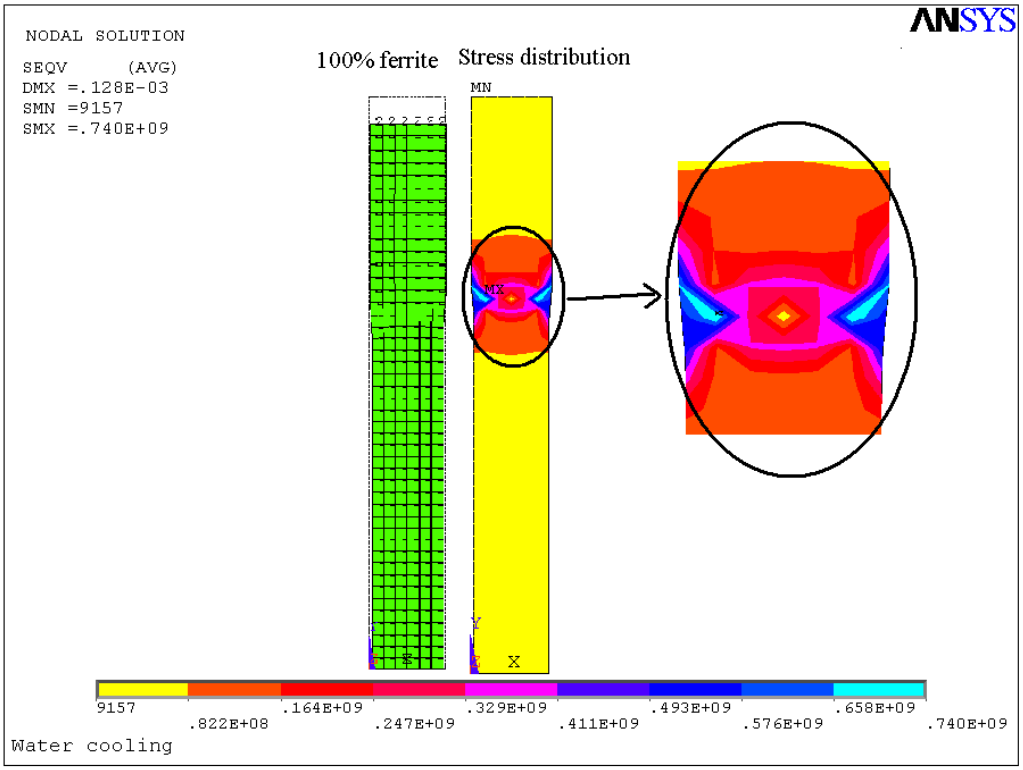

Figure 84 Stress distribution of rectangular grain model with no grain boundary at the grain interfaces after completion of austenite to ferrite phase transformation resulting from the cooling process.

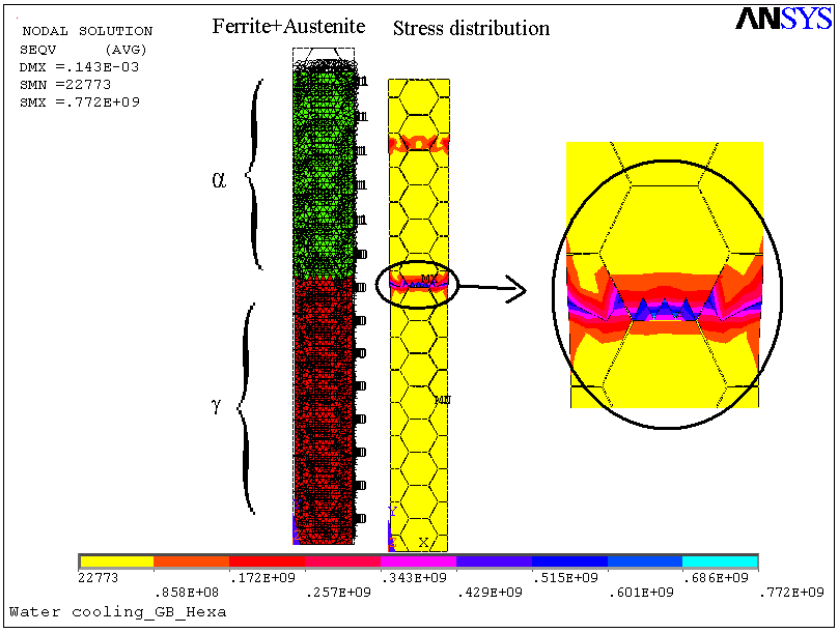

(a) Stress distribution (α+γ phases)

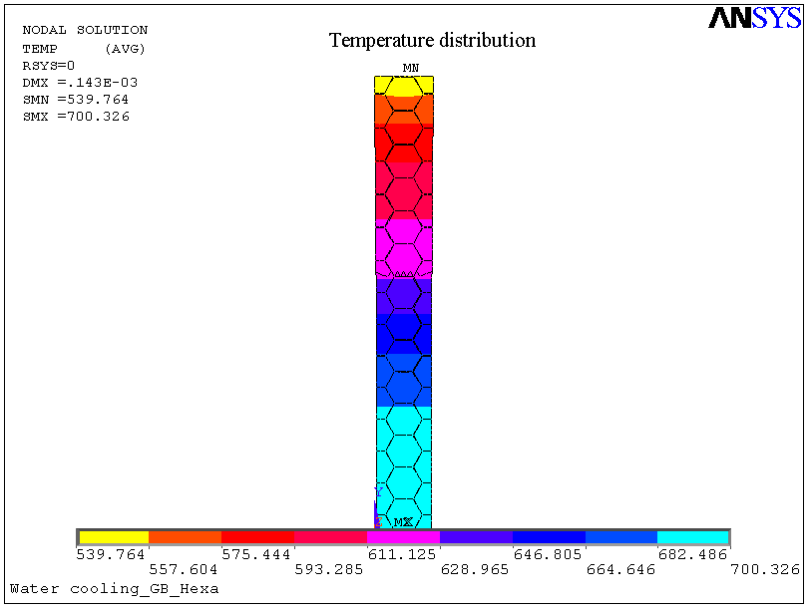

(b) Temperature distribution (α+γ phases)

Figure 85 Stress distribution results of phase transformation from the austenite to ferrite during accelerated cooling for the hexagonal grain model having body layers at the grain interfaces representing the grain boundaries.

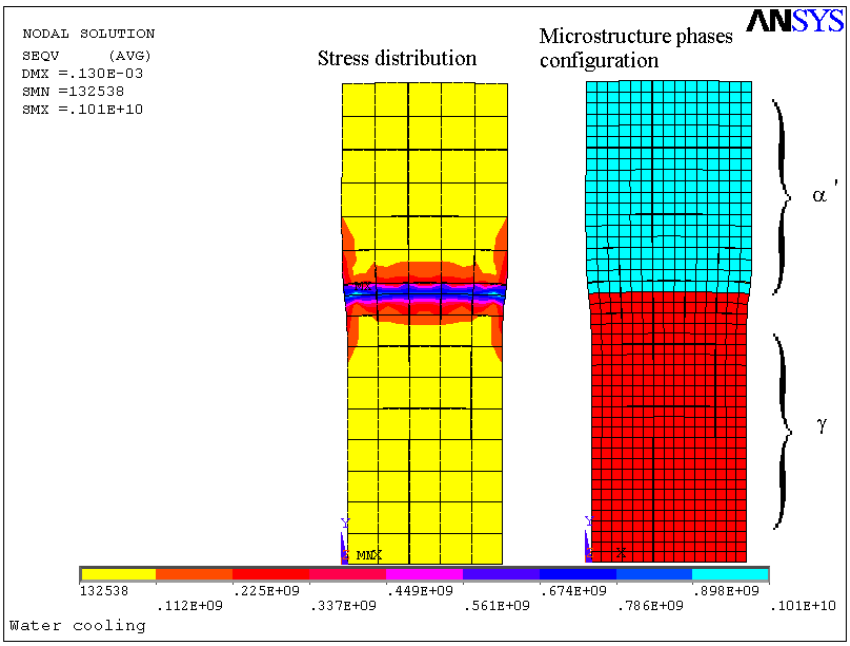

Figure 86 Two phase configuration (γ + α') stress distribution results obtained from the simulation of γ to α' phase transformation during the cooling of steel from the austenite temperature range.

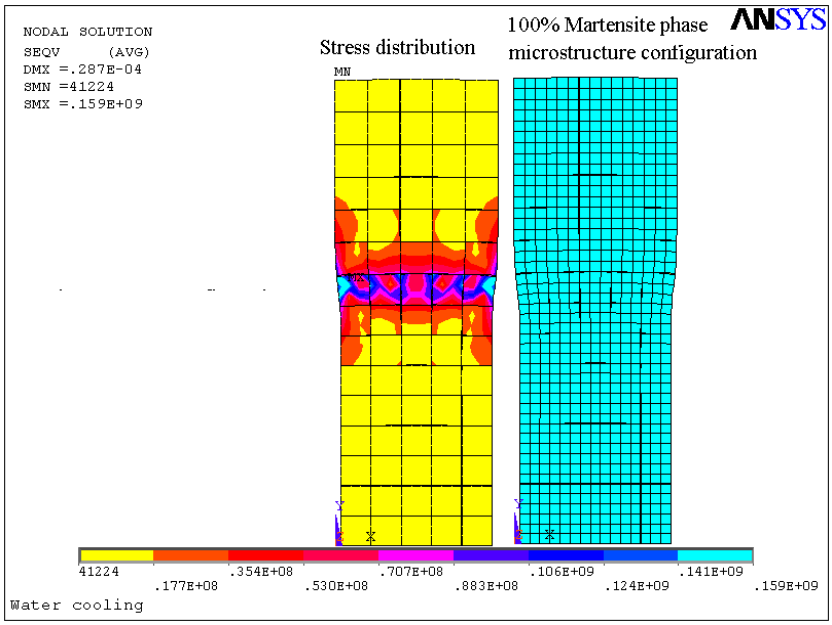

Figure 87 Stress distribution results obtained from the formation of a martensite microstructural configuration resulting from the simulation of γ —> α' phase transformation during cooling.

Figure 88 demonstrates the ability of the algorithm of the program to generate the two phase microstructure composed of α phase and α'phase from the γ phase microstructure. From

Figure 87 and Figure 88, it can be verified that residual stresses after the quenching process are accumulated at the martensite and ferrite phase boundary similar to the results for the two phase configuration with the γ phase and the α phase. These results represent the residual stress developed in the microstructure due to the transformation of the FCC lattice cells to BCC or HCP lattice cells, or both. The width of the models in Figure 87 and Figure 88were selected to be 5 mm to show that the stress accumulation occurs at the interface of the two phases for a wider model, as well.

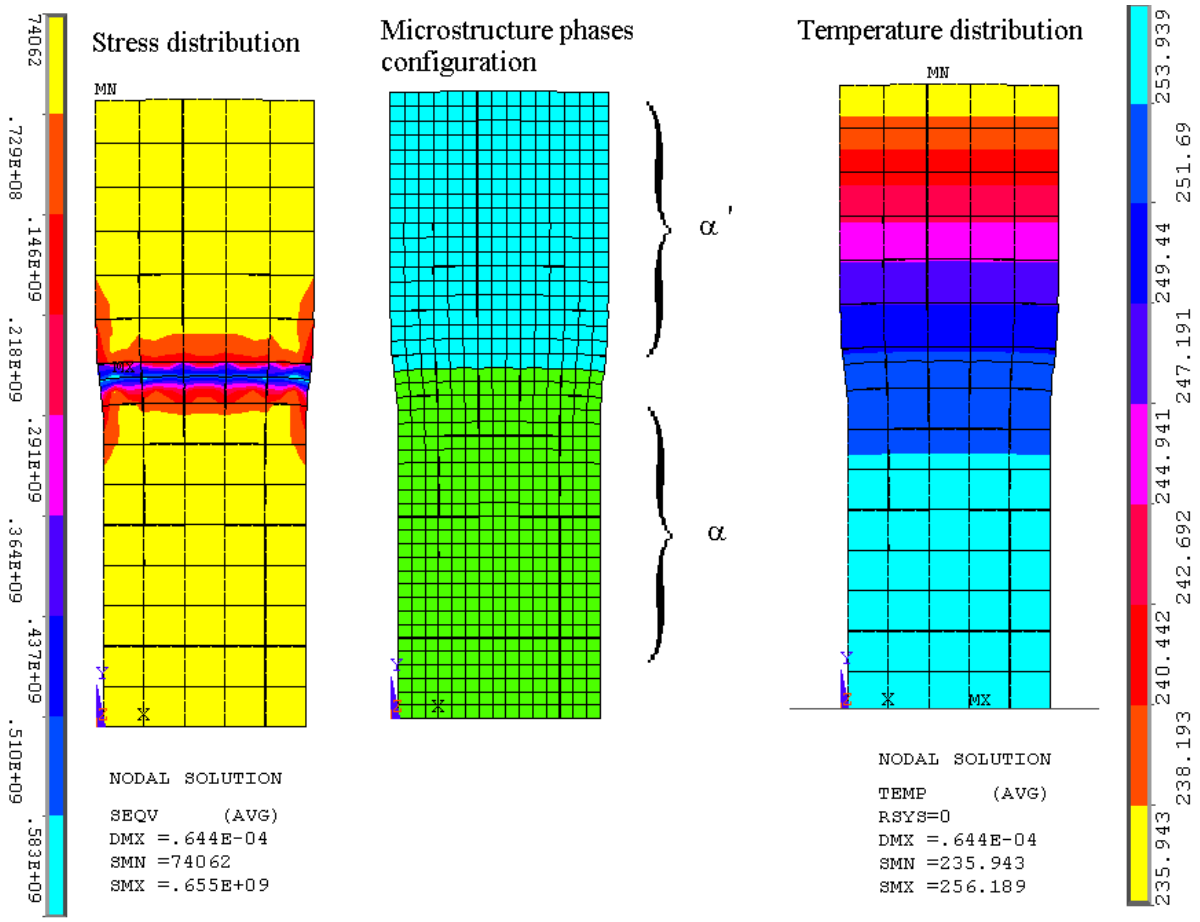

Figure 88 The results of γ—> (α + α') ' phase transformation simulation during the quenching process with an intermediate quenching rate.

The models were initially stress free, therefore, the source of high stresses in the model after phase transformation is volumetric strain of the solid-solid phase transformation rather than the thermal gradient due to cooling of the material. It can be deduced from the results of the stress analyses that neighboring grains with different phases experience higher stresses than the rest of the model. These regions are more vulnerable to the formation of microcracks or flaws or growth of the existing cracks or voids. This is because the stress concentration at the grain boundaries causes the debonding of the grain boundaries. It is consistent with the conclusion from previous research which stated that following both Griffith (energy) and Orowon (stress) criteria and, according to the Hall Petch equation, grain refinement requires higher debonding fracture stresses [336].

9.3 EFFECT OF THE DEFINITION OF THE GRAIN BOUNDARIES

Models with the same dimension and boundary conditions, as shown in Figure 82, were constructed with different methods of building grain boundaries at the grain interfaces. In the previous models, the results of models with two methods were presented .The first method was a model without any grain boundary at the intermediate surfaces of adjacent grains. In the no-grain boundary method, the thermodynamic information exchanges among the grains with, simply, a glue technique as one homogenous field. It is to neglect the effect of the grain boundary and to make the material properties of the grains responsible for any abrupt changes in the thermal or stress state within the model. The second method was the thin layer possessing all thermal and mechanical properties. The contact elements and cohesive zone methods give only the stress and strain failure criteria properties to the model. Figure 89 is the stress and temperature distribution

of the model with the grains interactions based on the cohesive zone technique. The cohesive force at the grain boundary is considered to be temperature dependent with a given value based on the graph in Figure 90 only for the sake of the simulation and not from any experimental results. The adhesion force among the grains in the model presented in Figure 91 was built of slave-master contact element methods and it was considered to be a constant value of 210 GPa. It can be observed that both the cohesive zone technique and the contact element method produced the same compression stress state results.

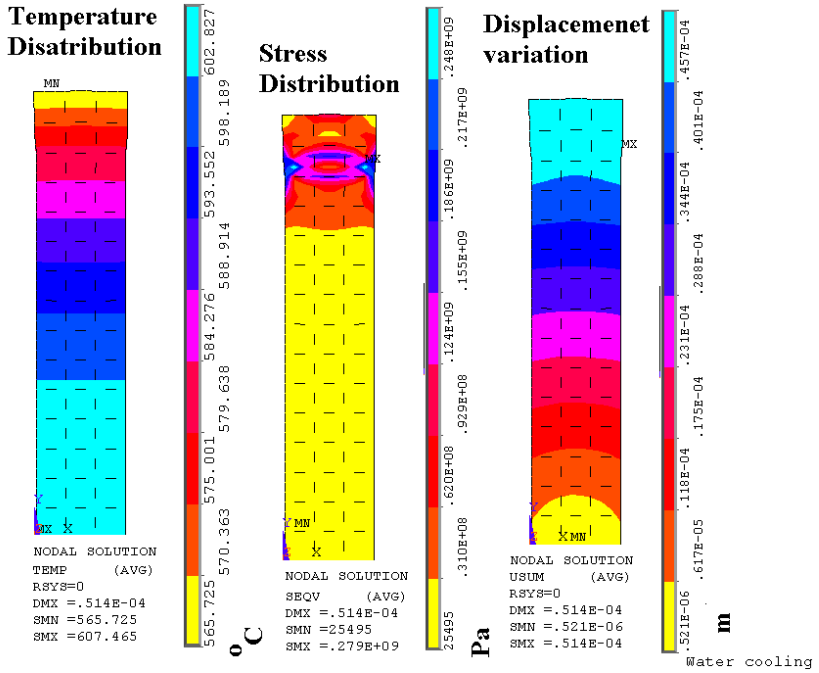

Figure 89 Results of the model with the grain boundary structure with the cohesive zone method.

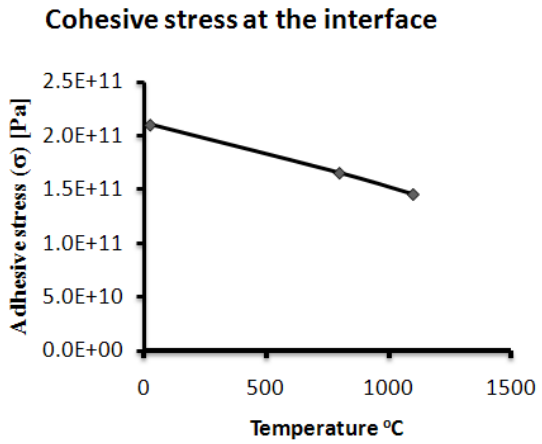

Figure 90 Temperature dependent cohesive force at the grains interface area assumed for the cohesive zone models.

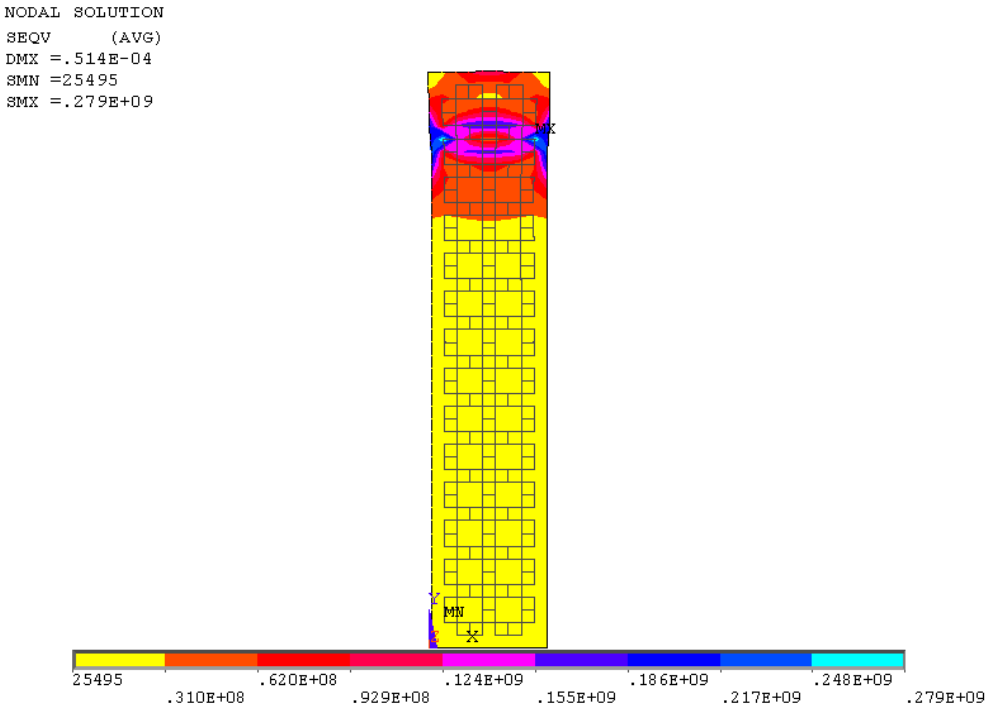

Figure 91 Stress distribution of the model with the grain boundaries defined with the contact element method.

9.4 EFFECT OF THE DEFINED COOLING RATE PARAMETERS ON THE ACCUMULATED RESIDUAL STRESS

Figure 92 is a summary of a series of the simulation with different time computational parameters to impose different cooling rates. The strain induced by the austenite to martensite transformation was considered slightly smaller than the strain induced by the austenite to ferrite phase transformation. This fact was applied in the algorithm based on the equation developed by Onink et al. and Lee et al. formulation explained in the governing equation Chapter. The results are collected after completion of the phase transformation.

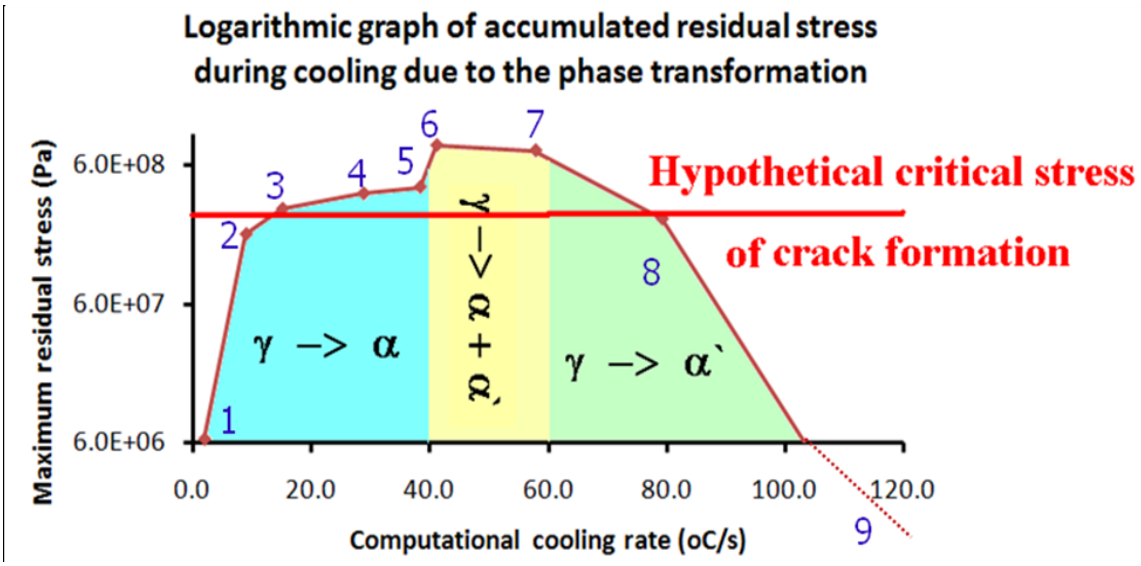

Figure 92 Variation in the stress accumulation at the grain boundary interface due to application of different cooling rates after completion of the solid-solid phase transformation.

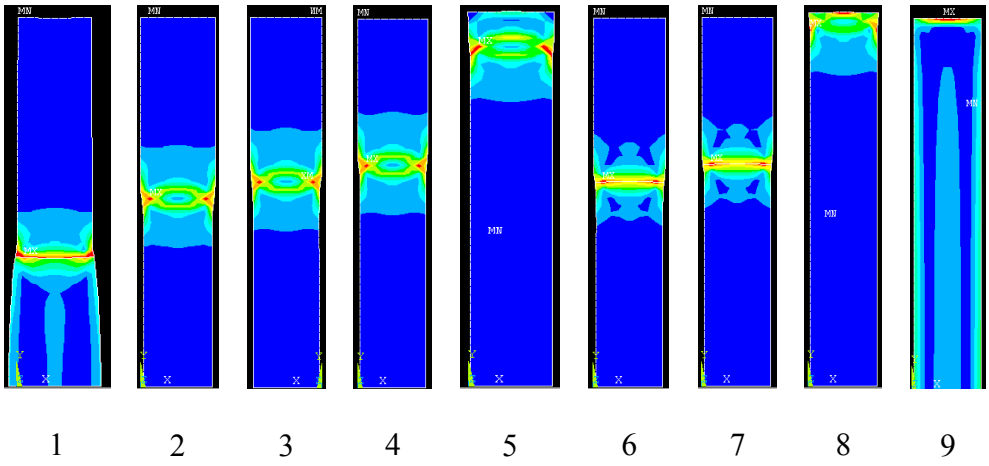

Figure 93 Stress distributions for results of the graph in the Figure 14.

The first section is the austenite to ferrite transformation and it shows that the residual stress accumulation is increasing as a higher cooling rate is applied. However, a slight decline in the stress accumulation can be observed in the two phase formation as the martensite formation took place with higher cooling rates. This can be a direct result of the lower strain of the martensite formation compared to the ferrite formation. The decrease of the maximum stress concentration in the third section is due to the effect of the time parameter in transforming the austenite to its solid-solid phase transformation products. In the case of a higher cooling rate the high stress concentration band is closer to the top surface and the chance for relaxation is higher. It can be understood by investigating the gradual transformation images in Figure 93. When the phase transformation is completed before the end of the load step, the cooling proceeds as single phase cooling simulation and the residual stresses are only the result of the thermodynamic strains without influence of the phase transformation strains. It shows the importance of applying parameters to assure accuracy of the results for simulation to obtain the optimum cooling rate.

9.5 PRESENTATION OF THE CRACK AND VOID FORMATION IN THE ALGORITHM

The last block in the proposed algorithm is to present the void and flaw initiation in the final results. However, if this block is placed in the time process cycle, the accuracy could be increased. Moreover, the probability of the divergent solution and crash of the simulation gets higher, as well. Figure 94 presents the void and flaw initiation in the model. The image on the bottom right side of the Figure 94 shows that the final product of the phase transformation is martensite. In this model, the cooling was applied from the top and the left side surfaces.

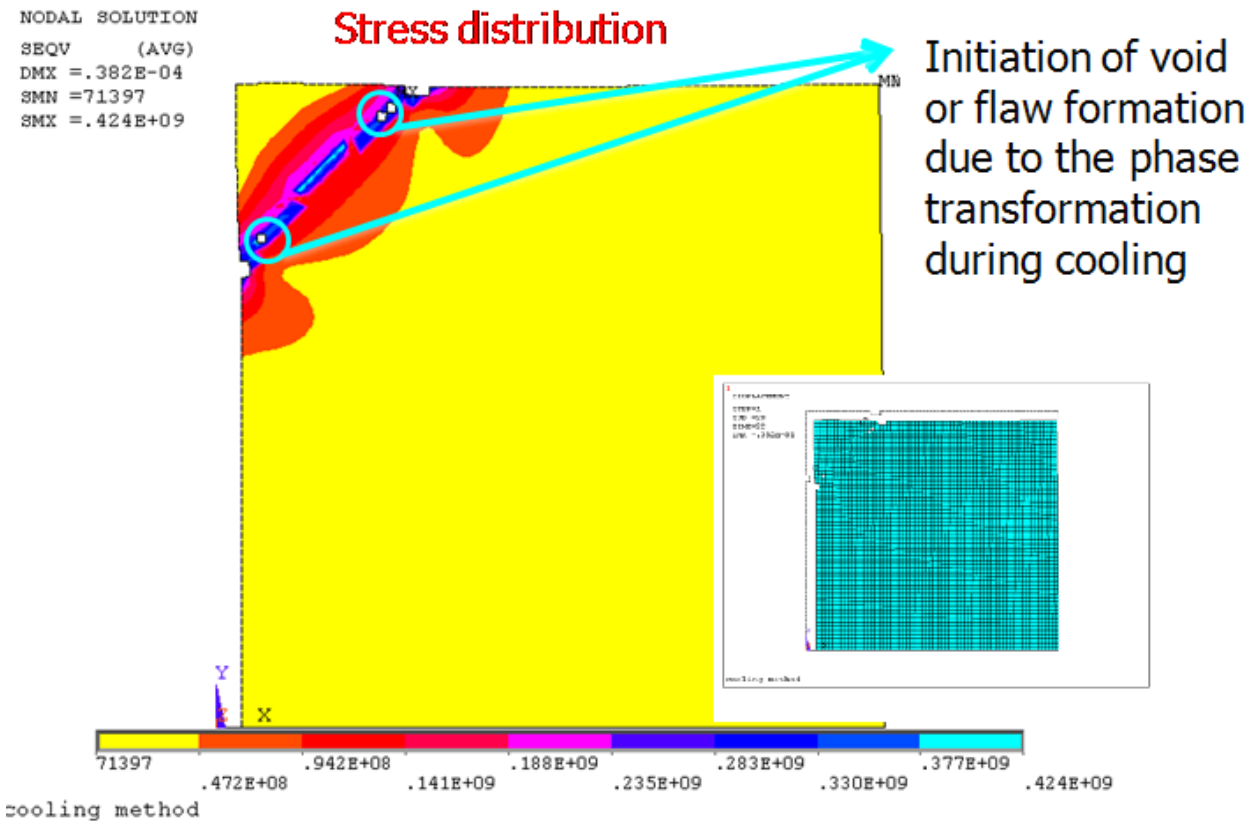

Figure 94 Presentation of the void and initiation of flaw formation.

9.6 RESULTS OF SUBCRITICAL COOLING

Figure 95 shows the results of the same model cooled from 600 ^{o}C. The cooling rate in the model presented in Figure 95 is approximately 50 ^{o}C/s. Low stresses in the model in Figure 95, show high cooling rates from the subcritical temperature range do not have much influence on the changes of the stress state and, consequently, defect configuration of the steel microstructure. Figure 95 is also evidence that the critical cooling rate has a strong relationship with the phase transformation.

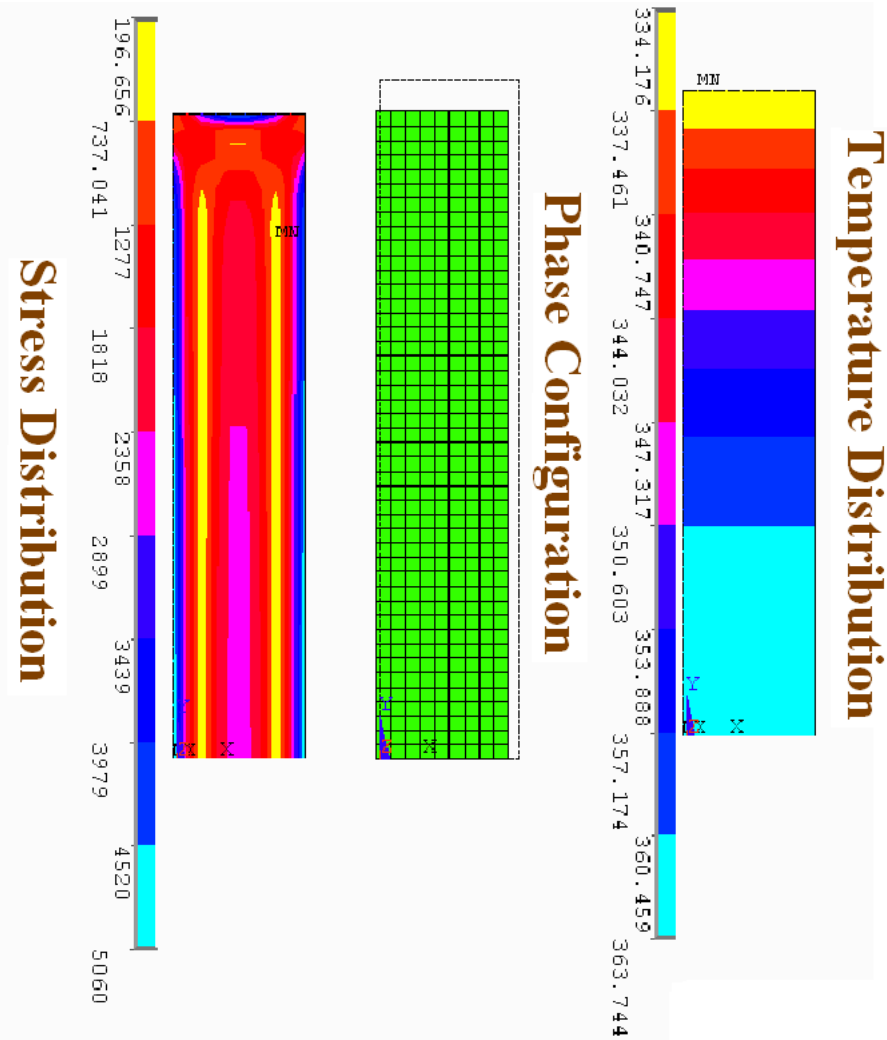

Figure 95 Cooling simulation from the subcritical temperature zone.

9.7 EFFECT OF THE GEOMETRY ON THE COOLING RATE

Comparing the results of the two models with the same numerical computation parameters and cooling method and parameters but different geometric dimensions, shows the effect of the geometry of the as-case on determining the optimum cooling rate. Figure 96 and Figure 97 can be used to compare the results of the two models with similar computational and modeling parameters with only a difference in the geometry of the models.

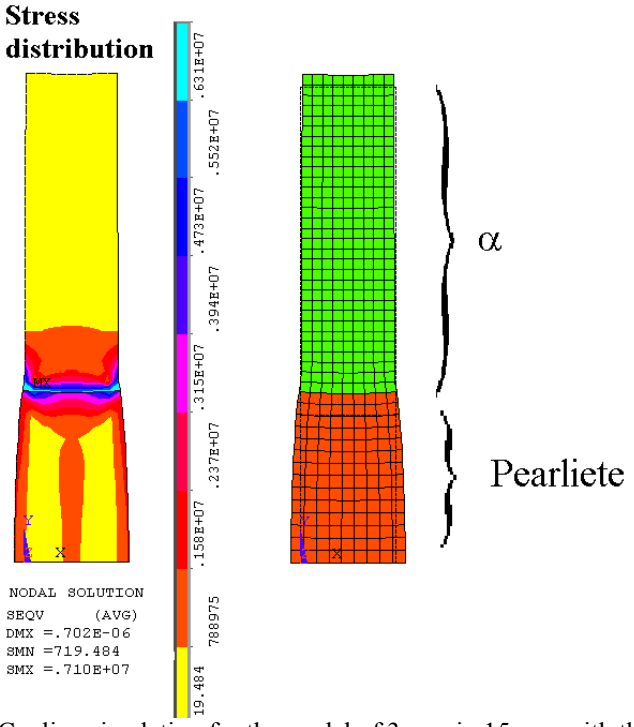

Figure 96 Cooling simulation for the model of 3 mm in 15 mm with the TCF =5.

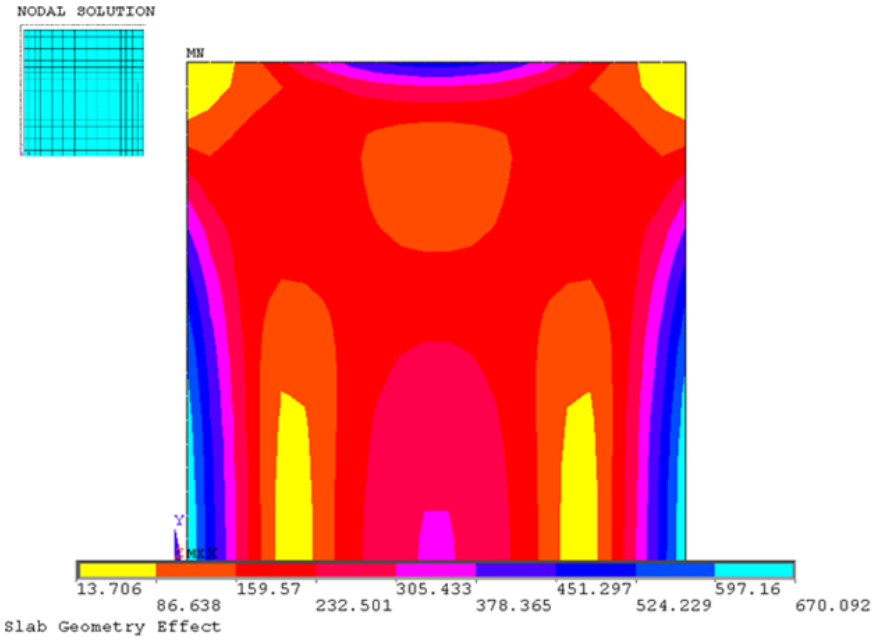

Figure 97 Cooling simulation for the model of 7 mm in 7 mm with the TCF=5.

Figure 96 is the model of 3 mm in 15 mm and the model in Figure 97 has the dimension of 7 mm in 7 mm. In these models, the cooling rate was controlled by the TCF=5. In addition to different phase transformation products, it seems that the load step is not the proper value if the model's dimensions are changed to shorter and wider size. Increase in the width provides a larger surface for the heat flux between the model and the cooling agent.

10.0 SUMMARY AND CONCLUSIONS

Main objective of this dissertation was to obtain a method to define the optimum cooling rate for the industrial size cooling as-cast steel especially for continuous casting steel production. An FEM algorithm developed with the ANSYS codes was introduced in this dissertation to simulate the cooling of as-cast steel from any temperature below solidification temperature. The algorithm is capable to be customized to simulate the thermodynamic behavior of as-cast steel microstructure with any chemical composition and any casting geometry for a desired cooling method.

The economical advantage of NDT tests over DT, i.e., microstructural analysis tests, is obvious, but their disadvantages are the level of accuracy and the strength or detail of the information. Furthermore, detailed information cannot be extracted from two-dimensional ultrasonic test directly and ultrasonic tests from different angles are more costly. The ultrasonic NDT post image processing developed in this dissertation coupled with the DT microstructural investigation, provides information to decode the information embedded in the NDT tests images. The Microsoft Excel program is coupled with a commercial software ultrasonic image processing process and analyzes TOF results to provide the tools to specify the type of the anomalies in the microstructure and the objective Cartesian coordinate position of the defect in the microstructure and, thereby, to assess each type of anomaly present in the microstructure of the continuously cast slabs cooled at different conditions. The proposed NDT image decoding

elaborates to perceive the behavior of the microstructure during cooling with higher precision by considering the existence of the major defects in the models for industrial applications.

The effect of the composition of the inclusion on the distribution of the stress concentration zone in the matrix was studied by two dimensionless factors, as defined in this paper. These factors were introduced as the stress concentration factors and the inclusion rigidity factor. Variation of the rigidity of the inclusion in a given matrix shows local extremum points within the interface and matrix contact surface at the interface. However, the average stress concentration inside the inclusion is higher for more rigid inclusions. The defined properties for the interface govern the average stress concentration around soft inclusions but the stress concentration around the inclusions with higher rigidity factor is related to the properties of the matrix. From the results of the simulation of the interaction of the inclusion in the steel matrix, it can be deduced that the smaller inclusions localize the residual stresses and create a higher stress concentration. Investigation of the size effect of the inclusion on the level of the stress concentration reveals a critical size of the inclusion where the stress concentration does not increase with the growth of the inclusion for a given applied load and boundary conditions.

The cooling rates of three different grades of steel were obtained experimentally. The numerical results for grade steel 1010* was computed to show a good estimation for experimental results using FEM code developed in this project using FEM numerical methods. Certain observations were made during the experiments. The FEM model is capable of computing the cooling rate considering the simplification and assumptions made in the model. The laboratory cooling experiments showed that cooling rates higher than critical cooling rates may produce a defect in the microstructure due to solid-solid phase transformation.

The simulations of the cooling models, based on the proposed algorithm, provided proof that there exists a specific critical cooling rate for cooling each grade of steel from the super-critical and inter-critical temperature ranges due to solid-solid phase transformation in which any cooling rate above the critical one may cause a crack or flaw in the continuously cast steel. Results of simulations also showed that although all five sources of the stress generations listed in this dissertation increase the residual stress of the microstructure, compared to solid-solid phase transformation, other sources of stress generation influence the optimum cooling rate on a smaller scale. The models presented in this research work demonstrated the potential concentration of residual stresses around two phase material such as iron-carbon alloys produced from solid-solid phase transformation and, on a smaller scale, due to the thermal gradient within the microstructure developed by the cooling process (e.g. around inclusions in the steel matrix).Since the maximum stress concentration zone usually appears at the interface of two phases in the microstructural configuration. The models were designed for thermally induced stresses (such as those resulting from cooling) rather than mechanically applied stress models. The properties of the grain boundaries (GB) play important roles in the intensity of the accumulated residual stresses due to phase transformation in steel slabs with accelerated cooling. This fact can be observed by comparing the models with four intergranular interaction methods introduced in this work. These four methods of the building interfacial region are;

- Interfaces formed by glued grains (without any grain boundary properties or structure)
- Thin layer bodies as such as grain boundaries with thermo-dynamic material properties
- Contact element interface method

- Cohesive zone interface method

The algorithm can simulate the cooling and solid-solid phase transformation processes for any grain shape. It was observed from the results of the numerical computation that the shape of the grains changes the distribution of stress concentration zones. The collection of the numerical simulations, resulting from different steps of the accelerated cooling simulation, indicates that the stress concentration zones generated by solid-solid phase transformation were stored in the microstructure. Thus, it indicates that further cooling below the transformation temperature with any cooling rate may not result in complete relaxation of regions of accumulated residual stress. From simulations it can be concluded that the critical cooling rate depends on the following

- Cleanliness of the microstructure (pre-existing flaws and voids)
- Initial stress state of the microstructure (σ_i)
- Chemical composition of the steel ($c\%$)
- Thermodynamic material properties of each phases
- Microstructural configuration (single phase or multi phase)
- Grain size and grain shape (D_γ^c)
- Size of the slabs (V_s)
- Cooling procedure ($T_{s\ i=1,\ldots,n}(\dot{T}^c_{s\ i=1,\ldots,n})$)
- Shape of the slabs
- Initial temperature of the as-cast slab at the start of the accelerated cooling process (T_t)
- Grain boundary properties (σ_{coh})

To obtain a critical cooling rate, the above factors can be formulated in a cooling rate equation:

$$\dot{T}^{c}_{crack\ formation} = f(T_{s\ \ i=1,\ldots n}(\dot{T}^{c}_{s\ i=1,\ldots n}), c\%, D^{c}_{\gamma}(T^{c}), \sigma_{coh}, \sigma_{i}, T_{t}, \alpha_{thermal}, V_{s}) \qquad \text{(Eq-72)}$$

The main conclusion of this research work is that a guideline can be introduced to find the cooling rate for each grade of steel. A combination of NDT and DT tests with thermodynamic material properties can be used to assess the cooling rate using the ANSYS FEM algorithm developed in this dissertation. The steel making industries can use this as a guide line to predict the following

- The possibility of crack formation or propagation for the applied cooling rate,
- Information about the size of the crack for the applied cooling rate,
- A platform to investigate the relationship between the crack formation and the steel composition for a given cooling rate.
- Connection between Continuous Cooling Transformation (**CCT)** diagram and altering the defect density for a given steel composition
- The residual stress distribution within the known microstructural configuration

11.0 FUTURE WORK

The accuracy of the guide lines proposed in this dissertation can be increased if different advanced steps are added to it. For example, in this work, the criteria to present the flaw initiation was based on having quenching stress higher than a constant critical value considered as cohesive stress at the grain boundary. In this case, the segregation of different alloying elements, the grain boundary resistance to flaw formation, changes as a function of elements present in the steel chemical composition. Figure 98 shows that competition between tensile residual stress and grain boundary resistance to the formation of a flaw as a function of segregation determine the critical optimum cooling rate for specific grade of steel.

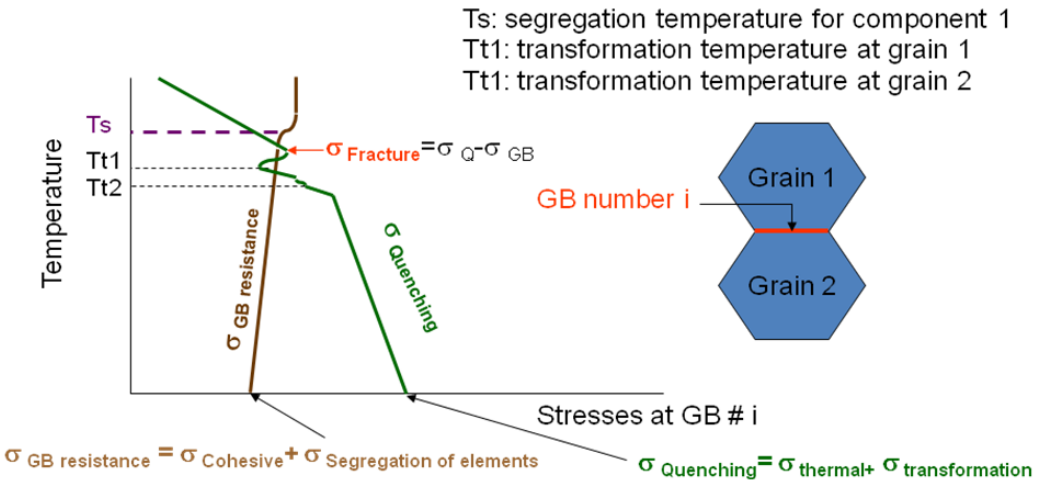

Figure 98: Increasing the accuracy of the algorithm by including the effect of segregation elements at the grain boundary to the flaw formation.

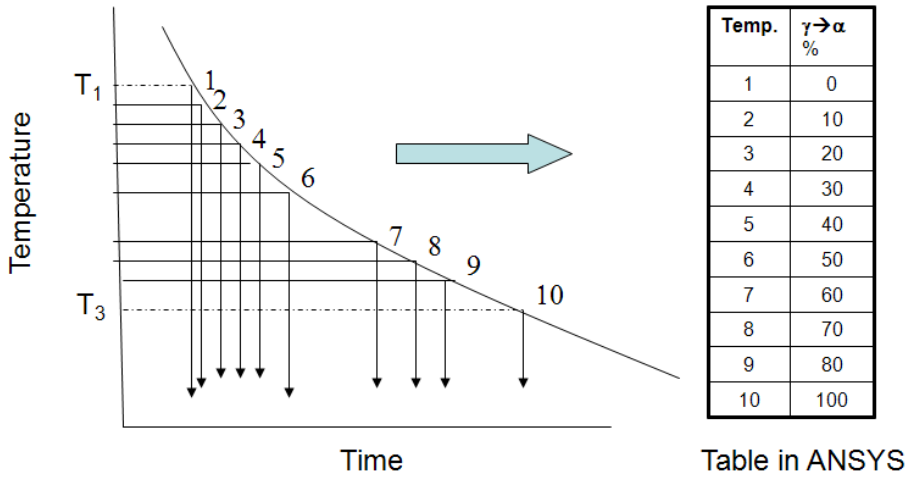

Temp.	γ→α %
1	0
2	10
3	20
4	30
5	40
6	50
7	60
8	70
9	80
10	100

Figure 99: Encapsulating method applied to determine the phase transformation product for each cooling rate.

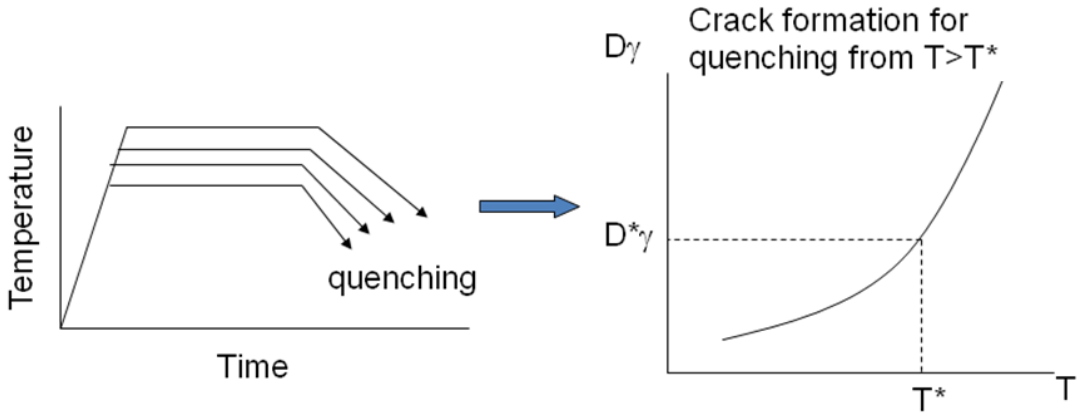

Figure 100: Collecting the cooling and casting experimental data to determine the critical values of the factors influence the optimum cooling rate of the continuous casting steel for each chemical composition f the steel.

The correction factors in the algorithm control the accuracy of the results. The precise value of these correction factors must be obtained for each case of the cast steel via cooling experiments in the laboratory and on industrial scales. Some laboratory test experiments have been started for this dissertation whose completions promote the accuracy of the results to determine the critical value for each factor involved in the critical cooling rate calculation. Figure 99 and Figure 100 are schematic views of these tests. Arranging a set of encapsulating steel sample to be used in the cooling tests with different cooling rates provides the samples for

microstructural investigation to determine the formation of the defect and volume fraction of the phases produced in the microstructure. Laboratory casting of steel with different compositions can regulate the correction factors designed in the algorithm to increase the accuracy of the results for the prediction of the crack formation in the continuous casting steel.

The growing demand for new steel products and competition to produce steel with higher quality and optimum production rate, will keep this research field open for many new ideas and researchers.

APPENDIX A

IDENTIFICATION NUMBER AND COOLING HISTORY OF EACH SAMPLE SLAB TESTED IN THIS DISSERTATION

STEEL TYPE	NAME			SIZE (INCHES)	COOLING METHOD
1010* STEEL	160530	204-A	CENT	9.5625x 9.875 x 2	Air Cooled
	160530	204-A	EXT	9.875 x 9.875 x 2	Air Cooled
	160530	204-B	CENT	9.875 x 9.875 x 2	Chamber Cooled
	160530	204-B	EXT	9.8125 x 9.8125 x 2	Chamber Cooled
	160530	205-A	CENT	9.8125 x 9.875 x 2	Air Cooled
	160530	205-A	EXT	9.8125 x 9.8125 x 2	Air Cooled
	160531	205-B	CENT	9.5625 x 9.8125 x 2	Chamber Cooled
	160530	205-B	EXT	9.8125x9.5625x 2.0625	Chamber Cooled

IDENTIFICATION NUMBER AND COOLING HISTORY OF EACH SAMPLE SLAB TESTED IN THIS DISSERTATION (CONTINUE)

STEEL TYPE	NAME			SIZE (INCHES)	COOLING METHOD
1319* STEEL	260191	502-A	CENT	7.5625 x 10 x 2	Air Cooled
	260191	502-A	EXT	7.5625 x 10.0625 x 2	Air Cooled
	260191	502-B	CENT	8 x 8 x 2	Chamber Cooled
	260191	502-B	EXT	8.125 x 8.125 x 2	Chamber Cooled
	260191	503-A	CENT	9.9275x9375x2	Air Cooled
	260191	503-A	EXT	9.9375x9.8125x2	Air Cooled
	260191	503-B	CENT	9x9x2	Chamber Cooled
	260191	503-B	EXT	9x9x2	Chamber Cooled
1091* STEEL	554754	102-A	CENT	8.5x8.5x2	Air Cooled
	554754	102-A	EXT	9.1875x9.8125x2	Air Cooled
	554754	102-B	CENT	9.4375x9.4375x2	Chamber Cooled
	554754	102-B	EXT	9.4375x9.4375x3	Chamber Cooled
	554754	103-A	CENT	9x9x2	Air Cooled
	554754	103-A	EXT	9x9x2	Air Cooled
	554754	103-B	CENT	8.5x8.5x2	Chamber Cooled
	554754	103-B	EXT	9.8125x9.8125x2	Chamber Cooled

BIBLIOGRAPHY

[1]. Bramfitt B. L., Speer J. G.; metal Trans., 1990, 21A, 817-829.

[2]. Ohmoi Y., Ohtsubo H., Jung Y. C., Okaguchi S., Otani H.; Metall. Trans., 1994, 25A, 1981-1989.

[3]. Lotter U., Hougardy H. P.; Prakt. Metallogr., 1992, 29, (3), 55, 201.

[4]. Dube C. A., AAeonson H. I., Mehl R. F.; Reb. Metall., 1958, 55, 201.

[5]. Aeonson H. I; "Decomposition of austenite by diffusioinal processes", 389, 1960, Philadelphia, PA, AIME.

[6]. New World Dictionary of the American Language 1986; Second college edition; Simon and Schuster.

[7]. Nemethy K., Stock E., Mackay B. F.; "Progress in Continuous Casting Stainless Steel Slabs at Atlas Steels Limited"; Continuous Casting, No. 62-18699,1962,pp:119-154.

[8]. Zhang, L. Thomas B. G.; "Inclusions in continues casting of steel"; XXIV National steelmaking Symposium, Morelia, Mich, Mexico, 26-28, pp 138-183, Nov 2003.

[9]. Lange K. W.; Inter.; Materials Reviews; 1988, 33(2), 53.

[10]. DeArdo A. J., Garcia C. I., Palmiere E. J.,; " Basic Metals Processing Research Institute", Department of Materials Science and Engineering, University of Pittsburgh; ASM Handbook, Vol 4, Heat Treatment, 1991.

[11]. Chunhui Luo; "Modeling of the behavior of inclusions in plastic deformation of steels", Doctoral thesis; division of Materials forming, Department of production engineering, royal Institute of technology, Stockholm, 2001.

[12]. Kiessling R.; Metal Science; 1980, 15(5), 161.

[13]. McPherson N. A., McLean A.; "Continuous Casting Volume Seven-Tundish to Mold Transfer Operation"; ed s 7,ISS, Warrendale, PA, 1992, 1-61.

[14]. Zhang, L. Thomas B. G.; ISIJ Inter., 2003, 43(3), 271.

[15]. Mu D., L. Holappa; "Gov. R.es. Announc. Index (USA); Report No. PB93-179471/XAB, 1993.

[16]. Cramb A. W.; in Impurities in Engineered Materials; Impact Reliability and Control, C. L. Briant, eds., Marcel Dekker Inc., New York, 1999, 49-89.

[17]. Continuous Casting of Steel 1985-A Second Study; International Iron and Steel Institute; Committee on Technology; Brussels; 1986.

[18]. Lei H., Zhu M-Y., He J. C.; "Simulation of nonmetallic inclusion behavior in the continuous casting mould"; Guocheng Gongcheng Xuebao (The Chinese Journal of Process Engineering) (China). Vol. 1, no. 2, pp. 138-141. Apr. 2001.

[19]. Y. Murakami, S. Kodoma, S. Konuma; Int J. Fatigue, 1989, 11, 291-298.

[20]. Y. Murakami, H. Hsuki; Int. J. Fatigue, 1989, 11, 299-307.

[21]. Y. Murakami, K. Kawakami, W. E. Duckworth; Int J. Fatigue, 1991, 13, 489-499.

[22]. Y. Murakami; T. Triyama, E. M. Condert; J. test Evaluation; 1994,22,318-326.

[23]. Y. Murakami, J. Res. Nat. Inst. Stand. Technol., 1994, 99, 345-350.

[24]. Y Uemura, Y. Murakami, trans. Jpn Soc. Mech. Eng., 1990, 56, 162-167.

[25]. Beretta S.1; Murakami Y.; Statistical Analysis of Defects for Fatigue Strength prediction and Quality Control of Materials; Fatigue & Fracture of Engineering Materials & Structures, Volume 21, Number 9, September 1998, pp. 1049-1065.

[26]. Shi, G.; Atkinson, H.V; Sellars, C.M.; Anderson, C.W. Comparison of extreme value statistics methods for predicting maximum inclusion size in clean steels; Ironmaking & Steelmaking, Volume 26, Number 4, August 1999, pp. 239-246(8).

[27]. Hogan, W.T. "Steel in the 21st Century", Lexington Books, New York, 1994.

[28]. B.G. Thomas, "Continuous Casting: Modeling," The Encyclopedia of Advanced Materials, (J.Dantzig, A. Greenwell, J. Michalczyk, eds.) Pergamon Elsevier Science Ltd., Oxford, UK, Vol.2, 2001, 8p., (Revision 3, Oct. 12, 1999).

[29]. U.S. Patent #1908, George Sellers.

[30]. Bessemer H.; "On the manufacture of Continuous Sheets of Malleable Iron and Steel Direct from Fluid Metal"; paper presented at the Iron and Steel Institute Meeting Oct 1891; J. Met., Vol 17, 1965, p 1189-1191.

[31]. Continental Iron and Steel Trade Report; The Hague, Aug 1970.

[32]. Pehlke T. D,; "Continuous Casting"; University of Michigan.

[33]. Bruce Kozak, Joseph Dzierzawski; Continuous Casting of Steel: Basic Principles; American Iron and Steel Institute;2005.

[34]. Tsai H. T., Yin H., Lowry M., Morales W.; "Analysis of Transverse Corner Cracks in Slabs and Countermeasures"; Iron & steel Technology; July 2006; 23-31.

[35]. McPherson N. A.; in Steelmaking Conference Proceedings; 68, eds., ISS, Warrendale, PA, 1985, 13-25.

[36]. Riboud, P. V. and Larrecq, M. Proc. NOH-BOS Conference, AIME, Rev. Metall. CIT, Jan. 1981, 78 (1), 29.

[37]. Scheel R. et al. Secondary steelmaking for production improvement; The Metals Society, London; Oct, 1984, Paper 6.

[38]. Charles R. Taylor; "Continuous casting Update"; Metallurgical transactions B; Vol. 6B; Sep 1975; pp: 359-375.

[39]. Andrezejewski P, Drastik A, Kohler K U, Pluschkell W 1990 New aspects of oscillation mode operation and results in slab casting. Process Tech. Conference Proc. (Warrendale, PA: Iron & Steel Soc.) vol. 9, pp 173-181.

[40]. Brendzy J L, Bakshi I A, Samarasekara I V, Brimacombe J K 1993 Mould-strand interaction in continuous casting of steel billets, part 2: Lubrication and oscillation mark formation. Ironmaking Steelmaking 20: 63-69.

[41]. Brimacombe J K 1993 Intelligent mould for continuous casting of billets. Metall. Trans. B24:917-928.

[42]. Darle T, Mouchette A, Nadif M, Roscini M, Salvadori D 1993 Hydraulic oscillation of the CC slab mould at Soleac Florange: First industrial results, future development. Steelmaking Conference Proc. (Warrendale, PA: Iron & Steel Soc.) vol. 76, pp. 209-218.

[43]. Harada S, Tanaka S, Misumi H 1990 A formation mechanism of transverse cracks on CC slab surface quality. South East Asian Iron & Steel Institute, pp 26-32.

[44]. Hoedle H, Frauenhuber K, Moerwald K 1999 Advanced equipment for high performance casters. Steelmaking Conference Proc, vol. 82, pp. 141-151.

[45]. Kim K, Yeo T, Oh K B, Lee D N 1996 Effect of carbon & sulphur on longitudinal surface cracks. Iron Steel Inst. Jpn. Int. 36: 284-292.

[46]. Nakagawa T, Umeda T, Murate T 1995 Strength and ductility of solidifying shell during casting. Trans. Iron Steel Inst. Jap. 35: 723-728.

[47]. Ray S K 2001 Effect of chemistry and solidification behaviour on quality of cast slabs and rolled products of stainless steel. J. Mater. Performance.

[48]. Ray S K, Mukhopadhyay B, Bhattacharyya S K 1996 Prediction of crack-sensitivity of concast slabs of AISI-430 stainless steel. Iron Steel Inst. Jpn. Int. 36: 611-612.

[49]. Ray S K, Mukhopadhyay B, Das P C 1999 Effect of chemistry on solidification and quality of stainless steel. Presented at Annu. Tech. Mtg. of Indian Inst. Metals, Jamshedpur, 14-17 Nov. 1999.

[50]. Saucedo I G 1991 Early solidification during continuous casting of steel. Steelmaking Conference. Proc. (Warrendale, PA: Iron & Steel Soc.) vol. 74, pp 79-89.

[51]. Sen S, Mukhopadhyay B, Ray S K 1996 Continuous casting and hot rolling of AISI-310 stainless. Steel India 19: 18-23.

[52]. Suzuki M, Mizukmi H, Kitagawa T, Kawakami K, Uchida S, Komatsu Y, 1991 Development of new mould oscillation mode for high-speed casting. Iron Steel Inst. Jpn. Int. 31: 254-261.

[53]. Szekeres E S 1996 Overview of mould oscillation in continuous casting. Iron Steel Eng. July: 29-37.

[54]. Tada K, Birat J P, Riboud P, Larrecq M, Hackel H 1984 Modeling of slag rim formation and pressure in molten flux near the meniscus. Trans Iron Steel Inst. Jpn. 24: B-382-B-387.

[55]. Takeuchi E, Brimacombe J K ;"The formation of oscillation marks in the continuous casting of steel slabs"; Metall. Trans., 1984, B15: 493-509.

[56]. Takeuchi S, Miki Y, Itoyama S, Kobayishi K, Sorimachi K, Sakuraya T 1991 Control of oscillation mark formation during continuous casting. Steelmaking Conference Proc. (Warrendale, PA: Iron & Steel Soc.) vol. 74, p. 303.

[57]. Wolf M M 1986 Strand surface quality of stainless steel. Ironmaking Steelmaking 13: 248-259.

[58]. Shirota Y.; in Nishiyama Memorial Seminar; 143/144. eds., ISIJ Tokyo, 1992, 167-191.

[59]. Kozak B., Dzierzawski J.; "Continuous Casting of Steel: Basic Principles"; SMS Damage.

[60]. W. Holzburber and /b. Termann: Steel times, 1967, Aug. 25, vol. 195, p. 217.

[61]. H. Muller; R. Jescher: Arch. Eisenhuettenw., 1973,vol. 44, p. 589, HB #9126.

[62]. H Garichen: Die Technique, 1967, vol. 22 p. 500, HB #7357.

[63]. W.R. Irving, Continuous Casting of Steel, (Institute of Metals, London, 1993).

[64]. K., Okuno, et al., "Dynamic Spray Cooling Control System for Continuous Casting," Iron and Steel Engineer, 4 (1987), 34-38.

[65]. K.-H., Spitzer et al., "Mathematical Model for Thermal Tracking and On-line Control in Continuous Casting," ISIJ International, 32 (7) (1992), 848-856.

[66]. S., Barozzi, P., Fontana, and P., Pragliola, "Computer Control and Optimization of Secondary Cooling During Continuous Casting," Iron and Steel Engineer, 12 (1986), 21-26.

[67]. J. Miettinen, "Calculation of Solidification-Related Thermophysical Properties for Steels", Met. Trans. B, 28B (1997), 281-297.

[68]. N M Vanaparthyy; Malur N Srinivasanz; "Modeling of solidification structure of continuous cast steel"; Modeling Simul. Mater. Sci. Eng. 6 (1998) 237-249.

[69]. Compendium of weld metal microstructures and properties; 1985, Abington, Woodhead Publishing.

[70]. Classification of microstructures in low carbon low alloy steel weld metal and terminology; Committee of Welding Metallurgy of Japan Welding Society, IIW Doc IX-1282-83.

[71]. Thewlis T.; "Classification and quantification of microstructures in steels"; Materials Science and technology; Vol. 20, Feb. 2004, 143-159.

[72]. Definitions and Causes of continuous Casting Defects; I. S. I.; Pub. 106,1967.

[73]. R. Kiessling, " Nonmetallic Inclusions in Steel (Part III)", ISI Publication 115, 1968.

[74]. V. A. Tipnis, N. H. Cook, "Influence of MnS-Bearing Nonmetallic Inclusions on Flow and Fracture in a Machining Shear Zone", AIME mechanical working, 1965, p. 285-308.

[75]. J. Harza, D. Caffarrelli, S. Ramalingma, " Free Machining Steels- the behavior of type I MnS inclusions in Machining" No. 73-WA/Prod-10, Transactional ASME, 1973.

[76]. H. Optiz, W. Konig, n. Diederich, "Verbesserung der Zerspanbarkeit von Unlegierten Baustahlen Nicht-metallische Einschlusse bei Verwendung Bestimmter Desoxydationslegierrungen", Westdeutscher Verlag, Koln and Opladen, 1967.

[77]. E. J. Paliwoda, The role of oxygen in free cutting steels", Proceeding AIME Mechanical working of steel 2, Volume 26, 1964.

[78]. W. Crafts, D. C. Hilty, "Sulfide and oxide formulation in steel", Proceedings of Electric Furnace steel conference, 1953, 121ff.

[79]. R. Kiessling, B Hassler, C. Westman, "Selenide-Sulfide inclusions and synthetic compounds of (Mn, Me) (Se, S) type", J. Iron and steel Institute, volume 205, 1967, pp. 380-39.

[80]. R. H. Aborn, " The Role of Metallurgy, Particularly Bismuth, Selenium, and Tellurium, in the Machinability of Steel", Pamphlet published by American Smelting and Refining Company, 120 Broadway, New York, NY 1968.

[81]. R. W. Thompson, D. t. Quinto, B.S. Levy, "Scanning electron Microscopy and Auger Electron Spectroscopy Observations on the role of lead in the machining of steel", Proceedings NAMRC-II, 1974, pp. 545-559.

[82]. S. ramalingam, K. Basu, J Hazra, " The role of Lead and Its Effect on MnS Inclusions in Leaded free Cutting Steels", Proceedings NAMRC-III, 1975, pp. 374-384.

[83]. Taylor F. W.; "On the art of cutting metals";, Transactions ASME, Volume 28, 1907.

[84]. D. B. Evteev; berg Huettenmann; Montash., 1966, vol. 11, p, 238 HB #6973.

[85]. M. A. Shtremel; "Problems of the Metallurgical Quality of Steel (Non-metallic Inclusion)"; Moscow Institute of Steel and Alloys (Translated from Metallovedenie i Termicheskaya Obrabtka Metallov); No. 8 pp 2-6; 1980.

[86]. C. J. Adams: NOH-BOS Conference Proceeding, Pittsburgh, 1971, vol. 54, pp. 290-302.

[87]. H. F. Hall: "Second Report of Steel Castings. Research Committee", The Iron Inst., London, 1936, p. 65.

[88]. D. P. Evteev; N. K. Stepanov; V. P. Druzhinin; N. G. Gladyshev; V. N. Ustyuzhanin; "Continuous Casting of Steel"; ed. O.V. Matynov, Metallurgya Press, 1970, pp. 240-251.

[89]. A Fuchs; ESTEL- Berichte aus Forschung und Entwicklung unserer Werke, 1975, no. 3; pp. 127-135.

[90]. K. Matsubara; Trans. Iron steel Inst; Japan, 1966, vol. 6, pp. 139-148.

[91]. H. Mori; Tetsu-to Hagane; 1974, vol. 60(7), pp. 784-806.

[92]. Y Sugitani; Research report; Sumitomo Metal Industries.

[93]. Brimacomb J., sorimachi K., "Crack formation in the continuous cast products"; Continuous Casting, Volume 9, The Iron &Steel Society, 1997.

[94]. J. K. Brimacombe; "Short Course on Continues Casting"; 33rd Electric Furnace Conference; Houston Texas; 1975.

[95]. Grill, Brimacombe; Weinberg; presented at the 104th AIME Meeting; Feb 1975.

[96]. J. K. Brimacombe; "Defect Problem in Continuous casting"; 33rd electric furnace conference; Houston, texas, 1975.

[97]. L. I. Motozenskii; O. A. Mitenev; V. K. Krutikov; Stal in English; 1965; no. 4, pp. 272-276.

[98]. G. van Drunen, J. K. Brimacombe, F Weinerg; Iron Steelmaking; 1975, vol. 2(2), pp. 125-133.

[99]. L. Backer, P.Gosselin; NOH-BOS Conference Processing; Detroit, 1970, vol. 53. pp. 145-156.

[100]. C. I. Miller, Jr; NOH-BOS Conference Processing; Pittsburgh, 1971, vol. 54, pp. 316-321.

[101]. J. W. Donaldson; J. Metals, 1965, vol. 17, pp. 1339-1343.

[102]. H. Krainer; B. Tarmann; J. Iron Steel Inst., 1958, vol. 196, p. 105.

[103]. K. P. Korotkov et al; "The continous Casting of Steel in commercial Use", 1960, Oxford, Pergamon.

[104]. H. Mori; Tetsu to Hagane; 1972,vol. 58(10), pp. 1511-1525 [Henry Brutcher translation N. 9000-I].

[105]. L Schmit, H Fredriksson; Iron Steelmaking, 1975, vol. 2(1)

[106]. T. Oita: Iron Steel Eng., Sept. 1965, vol. 42, p. 169.

[107]. W. F. Pontius; C. R. Taylor; Proc. Elect. Furnace Conf., 1967, vol. 11 p. S-402, HB #8907.

[108]. Y. Aketa, et al.: Tetsu-To-Hagane, 1959, vol. 45, p. 1341, HB #5223.

[109]. A. A. Skvortsov, et al; "Continuous Casting of Steel"; p. 126, Metallurgizdat Press, Moscow, 1970, HB #7594.

[110]. Dawson et. al.; Iron &Steel Maker; 1998, 15(7), 42.

[111]. Dawson et. al.; Iron &Steel Maker; 1998, 15(8), 34.

[112]. Dawson et. al.; Iron &Steel Maker; 1998, 15(9), 56.

[113]. Dawson et. al.; Iron &Steel Maker; 1998, 15(10), 54.

[114]. Dawson et. al.; Iron &Steel Maker; 1998, 15(11), 63.

[115]. Dawson et. al.; Iron &Steel Maker; 1998, 15(12), 26.

[116]. Dawson et. al.; Iron &Steel Maker; 1999, 16(1), 44.

[117]. Dawson et. al.; Iron &Steel Maker; 1999, 16(2), 36.

[118]. Malkiewicz T, Rudnik; " Deformation of Non-metallic Inclusions During Rolling of Steel"; S. J Iron Steel Inst 1963: 201: 33-38

[119]. Debiesme et. al.; Revue de Metallurgie- CIT; 1993, 90(3), 387.

[120]. Persson A., Hogmark S., Bergstrom J.; "Simulation and evaluation of thermal fatigue cracking of hot work tool steels"; International Journal of Fatigue 26 (2004); 1095-1107.

[121]. Ekerot S. ; "The behaviour of silicate inclusions in steel during hot working"; Scand. J. Metallurgy 3 (1974) 21-27.

[122]. Scruby C. B., Young R. M. K., Bull C. E; "in situ ultrasonic methods for determining microstructures and transformation kinetics"; Ironmaking and Steelmaking, 1995,, Vol. 22, No. 1, pp: 84-87.

[123]. Eckel J. A. et. al.; in advances in the production and Use of Steel with Improved internal Cleanliness; J. K. Mahaney; eds., American Society for Testing and Materials (ASTM), West Conshohocken, USA, 1999, 1-11.

[124]. Lund T. B., Olund L. K. P.; in Advances in the production and Use of Steel with Improved Internal Cleanliness; J. K. Mahaney; eds., American Society for Testing and Materials (ASTM), West Conshohocken, USA, 1999, 32-48.

[125]. Batia N. K.; Chaskelis H. H.; NDT International, 1975, 8, 261.

[126]. Bastien P.; NDT International, 1977, 108, 297.

[127]. Furuya Y. et. al.; Tetsu-to Hagane, 2002, 88(10), 643.

[128]. Drury J. C.; "Ultrasonic Flaw Detection for Technicians"; 3rd ed., chapter 2

[129]. Non-destructive Testing Research Center, http://www.ndt-ed.prg/, 2006.

[130]. Entrapment of non-metallic inclusions, http://www.matter.org.uk/steelmatter/casting, 2000.

[131]. Murugaiyanl T.; "Time of Flight Diffraction (TOFD), Advanced Non-Destructive Testing Technique for Inspection of Welds for Heavy walled Pressure Vessels", 2001.

[132]. Askland D. R., Phule P. P.; "Essentials of Material Science and Engineering"; Toronto, Nelsa, 2004.

[133]. Davies G. V.; "Solidification and Casting", New York, Wiley, 1973.

[134]. Baker T. J., Gove K. B. Charles J. A.; "Inclusion deformation and toughness anisotropy in hot-rolled steels"; Metals Technology; 3; 1976; 1183-1193.

[135]. Maropoulos S., Ridley N.; "Inclusions and fracture characteristics of HSLA steel forgings"; Materials Science and Engineering, A, 348, 2004, 64-69.

[136]. Hodge J. M., Frazier R. M., Boulger f. W.; Trans. Met. Soc. AIME 215, 1959,745.

[137]. Hausild P., Berdin B., Bompard P., Verdiere N., Int. J. Press. Vessels Piping, 78, 2001, 607.

[138]. Wagner D. et. al.; J. Nucl. Mat.l 300, 2002, 78.

[139]. Thomason P. F.; Fat. Fract. Ent. Mater. Struct.; 21, 1998, 105.

[140]. Hauslid P. et. al.; mater Sci. Eng., A335, 2002, 164.

[141]. Nicholson A., Gladman T., Ironmaking Steelmaking, 13, 1986. 53.

[142]. Hood J., Jamieson R. M., J. Ir. St. Inst., 301, 1973, 369.

[143]. Maropoulos S., Ridley N., R., Karagiannis S., Mater. Sci. Eng. A, in Press.

[144]. Tossoll A., Berdin C., Prioul C., Int. J. Fract., 15, 2002, 205.

[145]. Thornton P. A. ; "The influence of nonmetallic inclusions on the mechanical properties of steel: A review "; Journal of Materials Science , Volume 6, Number 4, 1971, 347 - 356.

[146]. Dhua S.K.; Ray A.m.i.t.a.v.a.; Sen S.K.; Prasad M.S.; Mishra K.B.; Jha S.; "Influence of Nonmetallic Inclusion Characteristics on the Mechanical Properties of Rail Steel"; : Journal of Materials Engineering and Performance, Volume 9, Number 6, December 2000, pp. 700-709(10)

[147]. T. Uesuigi; Trans. ISIJ, 1988, 28, 893-899.

[148]. T. Lund and J. Lkesson; in "Effect of steel manufacturing process on the quality of bearing steel, (ed. I. J. C Hoo), ASTM STP987, 308-312; 1988, Philadelphia, PA, USA, American Society for testing and Materials.

[149]. Baker T. J., Charles J. A.; ibid., 79.

[150]. V. S. Ivanova, "Fatigue Failure of Metals" [in Russian], Moscow; 1963.

[151]. N. I Muskhelishvil, "Some Basic Problems in the Mathematical Theory of Elasticity"; Naukam Moscow; 1966.

[152]. H, Neuber, "Stress Concentrations"; GITTL; 1947.

[153]. G. N. Savin; "Stress Concentrations around Holes"; GITTL; 1951.

[154]. I. M. Pavlov, A. V. Krupin; Scientific Reports of Universities; No. 1; Metallurgiya; Moscow; 1958.

[155]. I. M. Pavlov, A. V. Krupin; " Transactions of the A. A. Baikov Institute of Metallurgy , No. 7 ; Izd. AN SSSR; 1969.

[156]. V. M. Finkel, O. P. Elesina, V. M. Zarichenko, E. A. Mizahakova; "The Effect of Nonmetallic Inclusion of the Strength of Steel"; Vol 13,number 4, April 1971, pp 293-297.

[157]. Vogels H. A.; Bruening F.; Arch. Eisenh., 1964, 35, 115.

[158]. Dahl W. et. al.; Stahl Eisenh., 1966, 86, 782.

[159]. Wahlster et. al.; ibid., 1969, 89, 1037.

[160]. Farrar J. C. M. et. al.; "Effect of second phase articles on mechanical properties of steel"; 171, 1971, London, The Iron and Steel Institute.

[161]. Gove K. B. Charles J. A.; "Further aspects of inclusion deformation" Metals Technology;, 1; 1974; 425-431.

[162]. Waudby P. E.; "Factor controlling the plasticity of silicate inclusion"; Steel Times Annual Review; 1972, pp. 147-152.

[163]. Rudnik S., "Discontinuities in hot-rollers steel caused by non metallic inclusions"; J. Iron Steel Inst.; 204, 1966, 374-376.

[164]. Hilty D. C., Kay D. A. R.; Electric Furnace Steelmaking Conference Proceedings; 1985, 43, 237.

[165]. Maunder PJH, Charles J. A. J Iron Steel Inst 1968: 206: 705-715.

[166]. Baker T. J., Charles J. A. ; "Deformation of MnS inclusions in steel"; J Iron Steel Inst 1972: 210: 680-690.

[167]. Klevebring B. I. ; "The Deformation of Non-Metallic Inclusions in Steel during Hot Working"; Scandinavian Journal of Metallurgy 3 (1974) 102-104.

[168]. Becker R., Smelser R. E., Richmond O.; "The Effect of Void Shape on the Development of Damage and Fracture in Plane-Strain Tension"; J. Mech. Phys. Solids. Vol. 37, no. 1, pp. 111-129. 1989.

[169]. Sundstrom B.; "Plastic deformation of an infinite plate with elliptic inclusion"; J. composite Materials; 5 (1970) 277-300.

[170]. Zeisloft R. H., Hosford N. F. ; "Deformation of artificial inclusions in compressive strain"; Tran. Am. Soc. Metals 62 (1969) 17-25.

[171]. Belchenko G. I.; Gubenko S. I.; "Deformation of nonmetallic inclusion during steel rolling"; Russian Metallurgy (4); 1983, 66-69.

[172]. Banks TM, Gladman T. Metal Technol 1979: 6: 81-94.

[173]. Gove KB, Charles JA. Metals Technol 1974: 1: 425-431.

[174]. Maunder P. J. H.; Charles J. A.; JISI, 1968, 206, 705.

[175]. Kissing R.; "Non-metallic inclusions in steel" (Part III); 1968, London, The Iron and Steel Institute.

[176]. Pickering F. B., Robinson S. W.; "The plastic deformation and fracture of silicate inclusions in steel (chapter 8); Institution of Metallurgists; Inclusions Monograph (3);1979;127-156.

[177]. Paliwoda E. J.; AIME, 6th Mech. Woeking Conf., Chicago, 1964.

[178]. Thomson R. D., Hancock J. W., "Stress and strain fields around inclusions in a plastically deforming matrix"; Proc. ICM4, Stockholm, Sweden, Vol. II, 1983, p. 723.

[179]. Baker T. J., Charles J. A.; J Iron Steel Inst 1973: 211: 187-192.

[180]. Scheil E, Schnell R. Stahl Eisen 1952: 72: 683-687.

[181]. Pickering FB. J Iron Steel Inst 1958: 178: 148-159.

[182]. Daniel I. , A. Durelli; Proc. Soc. Exper. Stress Analysis, No. 1; 1961.

[183]. K. E. Ebaum; Progress in Physics of Metals; Vol. 5; Metallurgizdat; Moscow; 1963.

[184]. Phyical Nature of Brittle Fracture of Metals; Naukova Dumka; Kiev; 1965.

[185]. Kuznetsov B. A; Zavod. Lab.; No. 5; 1957.

[186]. Kuznetsov B. A.; Dokl. Akad. Nauk SSSR; 159, No. 1; 1964.

[187]. Polukhin I. I. et al.; Fiz. Metal. Metalloved.; 15, No. 6; 1963.

[188]. K. A. Mirkovskii; P.I.Polukhin; Izv. Vuzov. Tsvetnaya Metallurgiya, No. 6; 1946.

[189]. Gaaf G., Appl. Optics, 3, No. 1; 1964.

[190]. Acvan L.; Trans. Met. Soc. AIME; 230, No. 2; 1964.

[191]. . Khesin G. L, V. I. Sakharov; Izv. Vuzov. Stroitel'stvo I Arkhitektura, No. 7 1963.

[192]. Werlefors T., Ekelund S.; Scand J. Metall; 1978, 7, pp: 60-70.

[193]. Gladman T.; Clean Steel 3. Balatonfured, Hungary; 1986, pp:50-59.

[194]. Johansson S.; Scand J Metall; 1990, 19, 79-81.

[195]. Spizig W. A., Sober R. J., Panseri N. J.; Metallography; 1983, 16, 171-198.

[196]. Chunhui Luo and Ulf Ståhlberg; "An alternative way for evaluating the deformation of MnS inclusions in hot rolling of steel"; Scandinavian Journal of Metallurgy 2002; 31: 184-190.

[197]. Gilormini P., Germain Y.; " A finite element analysis of the inclusion problem for power law viscous materials". Int. J. Solids Structures; 23, 1987, 413-437.

[198]. N. Nagayama, T. Abe and S. Nagaki 1989 ;Plastic deformation of inhomogeneous materials with elliptic inclusions; Computational Mechanics. 4:433-441

[199]. Pietzyk, M. Kusiak J., Kusiak K., Grosman F.; "Fields of strain around the inclusion of second phase in a uniform matrix undergoing plastic deformation"; Steel Research, 62, 1991, 507-511.

[200]. Milenin A. A.; "Theoretical analysis of the stress strain state in the region of the inclusion of second phase under plastic deformation of two phases materials"; Russian Metallurgy, 2, 1995, 97-103.

[201]. Varde A. S., Maniruzzaman M., Rundensteiner E. A., Sisson R. D.; "The QuenchMinerTM Expert System for Quenching and Distotion Control"; Heat Treating and Surface Engineering-Chemistry of Quenching, Indiana, USA, Sep 2003, ISBN: 0-87170-797-7, pp:174-183.

[202]. MacKenzie D. S., Lambert D.; "Effect of Quenching Variables on Distortion and Residual Stresses"; Heat Treating and Surface Engineering, Indiana, USA, Sep 2003, ISBN: 0-87170-797-7, pp:184-191.

[203]. US EPA Air Pollution Training Institute developed in collaboration with North Carolina State University, College of Engineering (NCSU).

[204]. MacKenzie D. S.; "Advances in Quenching- A Discussion of Present and Future Technoligies"; Heat Treating and Surface Engineering, Indiana, USA, Sep 2003, ISBN: 0-87170-797-7, pp:184-191.

[205]. Totten G. E., Tensi G. M., Canale F.; "Fundamental Interfacial Chemical Processes Involved in Quenching"; Heat Treating and Surface Engineering-Chemistry of Quenching, Indiana, USA, Sep 2003, ISBN: 0-87170-797-7, pp: 141-147.

[206]. Totten G. E., Tensi G. M., Canale F.; "Fundamental Thermophysical Processes Involved in Quenching"; Heat Treating and Surface Engineering-Chemistry of Quenching, Indiana, USA, Sep 2003, ISBN: 0-87170-797-7, pp:148-155.

[207]. Heat Treating and Surface Engineering, Indiana, USA, Sep 2003, ISBN: 0-87170-797-7.

[208]. Gur C. H., Tekkaya A. E.; "Finite element simulation of quench hardening"; Steel research (Steel res.) ISSN 0177-4832 CODEN STLRCX , 1996, vol. 67, no. 7, pp. 298-306 .

[209]. Aaronson H. I.; "Historical perspective on general international conferences on the physical metallurgy/materials science of solid -solid phase transformations"; Farmington, U.S.A., The Minerals Metals & Materials Society, 19941, ISBN No. 0-87-339-278-7, pp:1-6

[210]. Pittsburgh, U.S.A., ASM Phase Transformations Committee, 1981, ISBN No. 0-89520-452-5.

[211]. ASM international; "Introduction of steels and cast iron," Mettallographer's Guide: Iron and Steels, 0640G, 2002.

[212]. Griffiths R. B.; "Critical and multicritical transformations"; Pittsburgh, U.S.A., ASM Phase Transformations Committee, 1981, ISBN No. 0-89520-452-5, pp:15-23.

[213]. Soffa W.A., Laughlin D.E.; "Recent experimental studies of continuous transformations in alloys: an overview"; Pittsburgh, U.S.A., ASM Phase Transformations Committee, 1981, ISBN No. 0-89520-452-5, pp:159-183.

[214]. Yeomans J." Some recent advances in the theory of critical phenomena "Farmington, U.S.A., The Minerals Metals & Materials Society, 19941, ISBN No. 0-87-339-278-7, pp:9-23

[215]. Du L, Liu, X., Wang G.; "The quenching problem in the study of strain induced transformation of low carbon steel"; Acta Metallurgica Sinica (China). Vol. 38, no. 2, pp. 196-202. Feb. 2002.

[216]. Atkins M.; "Atlas of continuous cooling transformation diagrams for engineering steels"; 1977, Swinden Laboratories, Rotherham, British Steel Corporation (ISBN 0 9500451 44).

[217]. Zhang Z., Farrar R. A.; "An atlas of continuous cooling transformation diagrams applicable to low carbon, low alloy weld metals"; 1995, London, The Institute of Materials.

[218]. Honeycombe R. W. K., Bhadeshia H. K. D. H.; "Steels microstructure and properties"; 2nd ed., 35,1995, London, Edward Arnold.

[219]. Baker T. J., Charles J. A.; "Effect of Second Phase Particles on the Mechanical Properties of Steel"; M. J. Mau, eds., The Iron and Steel Institute, 1971, 88-94.

[220]. Bhadeshia H. K. D. H.; "Bainite in steels", 1st ed., 1992, London, the institute of Materials.

[221]. M. A. Shtremel et al; Izv. Vyssh. Uchebn. Zaved. Chern. Metall.; No. 5' 1980.

[222]. Speich G. R., Leslis W. C.; Metall. Trans., 1972, 3, 1043-1054.

[223]. Speich D.R., Miller R. L; "Hardenability of austenite after intercritical annealing of dual-phase steels"; Pittsburgh, U.S.A., ASM Phase Transformations Committee, 1981, ISBN No. 0-89520-452-5, pp: 843-848

[224]. Zhuravlev L. G.,; "Temperature dependence of the mechanical properties of high carbon austenitic steel"; translated from Metallovedenie I Termicheskaya Obrobotka Metallov, No. 2, pp: 38-40, Feb 1964.

[225]. Kobasko N. I.; Met. Term. Ob. Metallov, 2, 1964, pp: 53-54.

[226]. Prince J. C., Marono R., Leon F, ;"Thermo-mechanical analysis of a piercing mandrel for the production of seamless steel tubes"; Proc Instn. Mech. Enhrs Vol. 217 Part E: Process Mechanical Engineering.

[227]. Mantyla M. et. al.; J. Nucl. Mat.; 264, 1999, 257.

[228]. Morris J. W.; "The Influence of Grain size on the mechanical properties of steel"; University of California, Department of Material Science and Engineering.

[229]. Kametani H.; "Fractal Analysis of the Surface Cracks on Continuously Cast Steel Slabs"; Metallurgical and Materials Transactions, V 29B, December 1998-1261.

[230]. Mishnaevsky L., Lippmann N., Schmauder S.; "Mesomechanical simulation of crack propagation in real and quasi- real idealized microstructures of tool steels"; ECF 13--13th European Conference on Fracture; San Sebastian; Spain; 6-9 Sept. 2000. 251 pp. 2000.

[231]. Berns H., Broeckmann C., Weichert D.; Eng. Fract. Mech., 58, 4, pp:311-325

[232]. Gross-Weege A., Weichert D., Broeckmann C.; Comp. Mat. Sci., 7, pp:123-130.

[233]. Donnay B., Jeraman J. C., Leroy V., Lotter U., Grossterlinden R., Pircher H.; Proc. Int. Conf. on "Modeling of metal rolling processes", London, UK, 1996, The Institute of Materials.

[234]. Lee J. K., Han H. N.; "Thrmomechanical processing of steels"; Vol. 1, 245-54, 2000, London, The Institute of Materials.

[235]. Trowsdale J., Randerson k., Morris P. F., Husain Z., Crowther D. N.; "Thrmomechanical processing of steels"; Vol. 1, 332-341, 2000 . London, The Institute of Materials.

[236]. Parker K. V.; "Modeling of phase transformations in hot rolled steels"; PhD thesis, University of Cambridge, UK, 1997.

[237]. Smoljan B.; "Numerical Simulation of Steel Quenching"; ASM International, JMEPEG Volume 11(1) February 2002 11:75-79.

[238]. Ehlers M., Muller H., Lohe D.; "Simulation of steel hardening"; 11th Congress of the International Federation for Heat Treatment and Surface Engineering and the 4th ASM Heat Treatment and Surface Engineering Conference in Europe; Florence; Italy; 19-21 Oct. 1998. pp. 263-272. 1998.

[239]. Smoljan B., Liscic B.; "Computer simulation of quenching of steel workpieces with complex shape"; Hungarian Scientific Society of Mechanical Engineering, Heat Treatment and Surface Engineering of Light Alloys: Proceedings of the 7th International Seminar of IFHT (Hungary), pp. 339-342, Sept. 1999; 1999.

[240]. Chen X. L., Meekisho L.; "Computer simulation of temperature and thermal stress fields during quenching process"; Second International Conference on Quenching and the Control of Distortion; Cleveland, Ohio; USA; 4-7 Nov. 1996. pp. 241-247. 1996.

[241]. Jones S. J., Bhadeshia H. K. D. K.; "Kinetics of the simultaneous decomposition of austenite into several transformation products"; Irreversible phase transitions in steels, Math. Appl.Sci., 20, 1997, pp:59-77.

[242]. Reti T., Fried Z., Felde I.; "Computer simulation of steel quenching process using a multi-phase transformation model"; Computational Materials Science, Volume 22, Issues 3-4 , December 2001, pp: 261-278.

[243]. Hougardy, H. P., Yamazaki, K., An improved calculation of the transformation of steels, Steel Res., 57 (1986), 466-471.

[244]. Homberg, D., A mathematical model for the phase transitions in eutectoid carbon steel, IMA J. Appl. Math., 54 (1995), 31-57.

[245]. Homberg, D., Irreversible phase transitions in steel, WIAS Preprint No. 131, 1994.

[246]. Agarwal, P. K., Brimacombe, J. K., Mathematical Model of Heat Flow and Austenite-Pearlite Transformation in Eutectoid Carbon Steel Rods for Wire, Metall. Trans. B, 12 (1981), 121-133.

[247]. Buza, G., Hougardy, H. P., Gergely, M., Calculation of the isothermal transformation diagram from measurements with continuous cooling, Steel Res., 57 (1986), 650-653.

[248]. Hawbolt, E. B., Chau, B., Brimacombe, J. K., Kinetics of Austenite-Pearlite Transformation in Eutectoid Carbon Steel, Metall. Trans. A, 14 (1983), 1803-1815.

[249]. Hengerer, F., Str□assle, B., Bremi, P., Berechnung der Abk□uhlvorg□ange beim □ Ol{ und Lufth□arten zylinder- und plattenf□ormiger Werkst□ucke aus legiertem Verg□utungsstahl mit Hilfe einer elektronischen Rechenanlage, Stahl u. Eisen 89 (1969), 641-654.

[250]. Verdi, C., Visintin, A., A mathematical model of the austenite-pearlite transformation in plain steel based on the Scheil's additivity rule, Acta Metall., 35, No.11 (1987), 2711-2717.

[251]. Visintin, A., Mathematical Models of Solid-Solid Phase Transitions in Steel, IMA J. Appl. Math., 39 (1987), 143-157.

[252]. Jones S. J., Bhadhesia H. K. D. H.; Acta. Metall., 1997, 45(7), 2911-2820.

[253]. Jones S. J.; "Modeling inclusion potency and simultaneous transformation kinetics in steels"; PhD thesis, University of Cambridge, UK, 1996.

[254]. Ichikawa K., Bhadhesia H. K. D. H.; "Mathematical modeling of weld phenomena 4"; 302-320, 1998, London, The Institute of Materials.

[255]. Subhajyoti Sen ,Balasubramaniam R.,Seturuman R.; "Finite element evaluation of elastic and plastic accommodation energies during hydride precipitation and dissolution"; Farmington, U.S.A., The Minerals Metals & Materials Society, 19941, ISBN No. 0-87-339-278-7, pp:25-30.

[256]. Simonelli G, Pasianot R., Savino R. J.; "Materials Theory and Modeling"; Broughton J., Bristowe P. Newsam J., eds., Mat. Res. Soc. Symp. Proc V.291. Boston, Ma 1993, 567-572.

[257]. Hondros E. d., Proc. Roy. Soc. Ser. S, 1965,286, 479-498.

[258]. Inman M. C., Tipler H. R., Met. Rev,. 1963, 8, 105.

[259]. Chen J.K.,Farkas D., Reynolds W.T.; "Atomistic stimulation of fcc. bcc. interphase boundary structures and energies"; Farmington, U.S.A., The Minerals Metals & Materials Society, 19941, ISBN No. 0-87-339-278-7, pp:1097-1102.

[260]. Wang Y., Chen L-Q.,Khachaturyan A. ;"Computer simulation of microstructure evolution in coherent solids"; Farmington, U.S.A., The Minerals Metals & Materials Society, 19941, ISBN No. 0-87-339-278-7, pp: 245-265.

[261]. Homberg, D.;"A numerical simulation of the Jominy end-quench test".

[262]. Scheil E; Arch. Einsenhuttenwes, 12, 1935, pp:565-570.

[263]. Askeland D. R., Phule P. P.; ISBN: 0-534-25309-1, 2004.

[264]. Johnson W. A., Mehl R.. F.; Trans. Amer. Inst. Min. Metallurg. Eng., Iron Steel Div., 135, 1939, pp:416-458.

[265]. Koistinen D. P. , Marburguer R. E.; Acta Metall. 7, 1959, pp:59-61.

[266]. Ortiz M., Popov E. P.; Int. J. Num. Meth. Engng. 21, 1985, pp:1561-1576.

[267]. Umansev A. R. ; "Continuum methods in the kinetic theory of phase transformations" Farmington, U.S.A., The Minerals Metals & Materials Society, 19941, ISBN No. 0-87-339-278-7, pp:31-37.

[268]. Wang K. F., Chanderansekar R S., Yang H. T. Y.; "Experimental and computational study of the quenching of carbon steel"; Journal of manufacturing science and engineering (J. manuf. sci. eng.) ISSN 1087-1357, 1997, vol. 119, no3, pp. 257-265.

[269]. Lusk M., Jou Y. K.; "A global material model for simulating the transformation kinetics in low alloy steels"; Proc. 7th international Seminar of IFHT, Budapest, Hungary, 1999, pp:273-282.

[270]. Saimoto A., Nistiani H.; "Crack propagation simulation in a plate with cracks and an inclusion"; Transaction on Engineering Sciences, Vol 19, ISSN 1743-3533, 1998.

[271]. Yu H. J.; Brechnung von Abkuhlungs, Umwandlungs, Schqweib, sowie Verformungseignspannungen mit Hilfe der Methode der Finiten Elenmente, Karlsruhe 1977,(Dr, -ing, thesis)

[272]. Hildenqall B.; "Prediction of the residual stresses created during quenching"; Linkoping, 1979, (PhD thesis).

[273]. Sjostrom S, Mater. Sci. Technol., 1985, pp:823-829.

[274]. Denis S., Gautier S., Simon A., Beck G.; Mater. Sci. Technol., 1985, pp:805-814.

[275]. Leblond j. B., Mottet G, Devaux J. C., ; Mater. Sci. Technol., 1985, pp:815-822.

[276]. Wittmann F. H.; "Crack formation and fracture energy of normal and high strength concrete"; Sadhana Vol. 27, Part 4, August 2002, pp. 413-423.

[277]. SUZUKI M., HAYASHI H., SHIBATA H., EMI T., LEE I.-J. ; “Simulation of transverse crack formation on continuously cast peritectic medium carbon steel slabs”; Steel research (Steel res.) ISSN 0177-4832 CODEN STLRCX, 1999, vol. 70, n°10, pp. 412-419.

[278]. Saimoto A., Nisitani H.; "Crack propagation criterion and simulation under biaxial ,loading'; Damage and Fracture Mechanics VII, CA Brebbia, & SI Nishida (Editors), ISBN 1-85312-926-7.

[279]. E. H. Smith; Mechanical Engineer's Reference Book, 12th Edition. Elsevier, Amsterdam, 1998.

[280]. Argon A. S., Im J., Safoglu R.; "Cavity formation from inclusions in ductile fracture"; Metall. Trans. 6A, 1975, 825-837.

[281]. Hoods S. H; "Brown L. M.; "The nucleation of cavities by plastic deformation"; Acta. Metakk., 27, 1979, 1-15.

[282]. Fisher J. R., Gurland J.; "The effect of alloy deformation on the average spacing parameters of non-deforming particles"; Metall. Trans., 12A,1981, 167-171.

[283]. Thomson R. D., Hancock J. W.; "Ductile failure by void nucleation, growth and coalescence"; Int. J. Fract., 26, 1984, 363-371.

[284]. McClintock F. A.; "A criterion for ductile fracture by the growth of holes", Journal of Applied Mechanics, 35, 1968, 363-371.

[285]. Lay B., Brunet M., Boivin M.; "Modeling of void nucleation and fiber debonding in a composite material"; Journal of Materials Processing Technology, 77, 1998, 254-59.

[286]. Spitzig W. A. , Metall. Trans. 14A, 1983, 271.

[287]. Ueda Y., Tanigawa M. , Murakawa H. ; "An evaluation method for ductile crack propagation in pre-strained plates"; Journal of the Society of Naval Architects of Japan (J. Soc. Nav. Archit. Jpn.) ISSN 0514-8499 , 1996, vol. 179, pp. 399-406.

[288]. Beer, F.P., Johnston, Jr., E.R. (1981), Mechanics of Materials, McGraw-Hill, Inc. (New York).

[289]. Pehlke R. D.; "Heat Transfer I"; Short course on Continuous Casting, 33rd Electric furnace conference, Houston, Texas, Dec, 1975.

[290]. Jezy A Owczarek, "Introduction of Fluid Mechanics", 1968, 68-16206

[291]. http://hyperphysics.phy-astr.gsu.edu/

[292]. Turcotte, Donald L.; Schubert, Gerald (2002). Geodynamics, 2nd Edition, Cambridge. ISBN 0-521-66624-4.

[293]. Incropera F. P., DeWitt D. P.; "Fundamentals of Heat and Mass Transfer", 5th Edition, Wiley. (August 9 2001), ISBN 0-471-38650-2.

[294]. F. P. Incropera, D. P. DeWitt, Fundamentals of heat and Mass Transfer, 6th Edition, Willey and Sons, 2006.

[295]. Gomez M., Garcia C. I., Haezebrouck D. M., DeArdo A. J.; "Compositional Design Concepts Using Al and Si as Alloying Elements in TRIP Steels"; International Conference on Microalloyed Steels: Processing, Microstructure, Properties and Performance, Iron & Steel Technology, July, 2007, Pittsburgh, Pennsylvania, USA.

[296]. Baird J. D.; Preston R. R.; Processing and Properties of Low Carbon SDteels; J. Gray; Ed,. American Institute of Mining, Metallurgical, and Petroleum Engineers, 1973, p 1.

[297]. Pickering F. B.; "Physical Metallurgy and the Design of the Steels", Applied Science, London, 1978, p 140.

[298]. Gladman T., Dullieu D., Mclvor I. D.; Microalloying 75, M. Korchynsly et al., Ed., Union Carbide Corporation, 1977, p32.

[299]. Backofen W. A.; Deformation Processing, Addison Wesley, 1972, p 57.

[300]. Dieter G. E.; Mechanical Metallurgy, 3rd ed,. McGraw-Hill. 1986, p 471.

[301]. Onink M, Brakman S. M., Tichelaar F. D., Mittemeijer E. J., Van der Zwag S.; Scripta Mater. 1993, 29:1011.

[302]. Lee S. J., Lusk M. T., Lee K. Y.; "Conversional model of transformation strain to phase fraction in low alloy steels"; Acta Materalia, 55, (2007), 875-882.

[303]. Aketa Y., Ushinjama K. ;Tetsu To Hogane, 46, 1733 (1960).

[304]. DeHoff R. T.; "Thermodynamics in materials science"; McGraw Hill (1993), ISBN: 0-07-016313-8, page 43.

[305]. Wayman C.M.; "Martenistic transformations: an overview"; Pittsburgh, U.S.A., ASM Phase Transformations Committee, 1981, ISBN No. 0-89520-452-5, pp: 1119-1144.

[306]. Beachamp P., William J.P.; "Computer determination of minimum energy path in the bcc-fcc transformation by homogeneous deformations "Pittsburgh, U.S.A., ASM Phase Transformations Committee, 1981, ISBN No. 0-89520-452-5, pp: 1221-1225

[307]. Material Science Forum; ISSN 0255-5476, Volume 3, 1985.

[308]. Rath B. B.; "The overall kinetics of isothermal transformations"; Pittsburgh, U.S.A., ASM Phase Transformations Committee, 1981, ISBN No. 0-89520-452-5, pp: 1097-1103.

[309]. McPherson N. A., Mercer R. E.; "Continuous Casting of Slabs au BSC Ravenscraig Works"; Ironmaking and Steelmaking, 1980, No. 4, pp: 167-179.

[310]. Harada S., et al.; "A formation mechanism of transverse cracks on CC slab surface", ISIJ international, Vol, 30, No. 4, 1990, pp:310-316

[311]. Stuart H., Ridley M.; J. Iron & Steel Inst 1970 (May):469.

[312]. Release 11.0 Documentation for ANSYS.

[313]. Brandes E. A.; "Smithells Metals Reference Book"; 6th edition, Butterworth, London, 1983.

[314]. Bower A. F.; "EN222: Mechanics of Solids II, Constitutive models"; Brown University.

[315]. Bonet J, Wood R. D.; "Nonlinear continuum mechanics for finite element analysis"; Cambridge University, 1997, ISBN 0 251 57272.

[316]. Lis?c?ic´ B. Tensi H., Luty W.; "Theory and Technology of Quenching"; ed., Springer-Verlag, 1992.

[317]. Nye J. F.; "Physical Properties of Crystals: Their Representation by Tensors and Matrices", Clarendon Press, Oxford (1957).

[318]. Hansen T., Jonsson P.; 2001 Electric Furnace Conference Proceedings; ISS, Warrendale, PA, 2001, 59, 71-81.

[319]. A. B. Kuslitskii; "Nonmetallic Inclusions and Fatigue of Steel"; Tekhnika, Kiev; 1976.

[320]. L. T. Berezhnitskii, R. S. Gromyak, I. I. Trusch; Fiz. Khim. Mekh. Mater.; No. 5, 40; 1973.

[321]. Garcia, C I; Pytel, S; Deardo, A J; The effect of Non-inclusions on the hot ductility of continuously cast low-alloy steel; ECF6 Fracture Control of Engineering; vol. 3. pp. 1811-1823, June 1986.

[322]. Kardomateas, G A; "Fractographic Observations in Asymmetric and Symmetric Fully Plastic Crack Growth"; Scr. Metall. Vol. 20, no. 5, pp. 609-614. May 1986.

[323]. Gubenko S. I. ; "Deformation mechanism for a steel matrix close to inclusions under compression", Metal Science and Heat Treatment ,Volume 25, 1983, 368 - 371.

[324]. Moore C.; M. Met. Thesis, 1968, University of Sheffield.

[325]. Pickering J. B.; ibid., 1958, 189, 148.

[326]. Stadnyk M. M. ; "Stress Concentration near an Elastic Ellipsoidal Inclusion in an Infinite Body"; Materials Science , Volume 38, Number 6, November 2002, 789 - 797.

[327]. Chunhui Luo and Ulf Ståhlberg ; "FEM simulation of void formation close to an inclusion in a uniform matrix during plastic deformation"; Simulation of Materials Processing; Theory, Methods and Applications, Rotterdam, 1998, pp 379-384.

[328]. Harik V. M., Cairncross R. A.; "Evolution of interfacial voids around a cylindrical inclusion" Journal of Applied Mechanics, 66, 1999, 310-314.

[329]. Gurland, J., Plateau, J., Trans. ASM, vol. 56, pp. 42.

[330]. Argon, A.S., JM, J., Sagoflu, R., Metall. Trans., vol. 6A, 1975. pp. 825.

[331]. Brunet JC, Bellot J; "Deformation of MnS inclusions in steel"; J Iron Steel Inst 1973: 211: 511.

[332]. Shi G.; Atkinson H.V.; Sellars C.M.; Anderson C.W.; Yates J.R.; Computer simulation of the estimation of the maximum inclusion size in clean steels by the generalized Pareto distribution method ; Volume 49, Number 10, 13 June 2001, pp. 1813-1820(8).

[333]. Paulo Rangel Riosa, Fulvio Siciliano Jrb, Hugo Ricardo Zschommler Sandimc*, Ronald Lesley Plautd, Angelo Fernando Padilhad; "Nucleation and Growth During Recrystallization"; Materials Research, Vol. 8, No. 3, 225-238, 2005.

[334]. Mullins M 1984 Computer simulation of fracture using long range pair potentials Acta Metall. 32 381.

[335]. International Iron and Steel Institute, ISSN 1379-9746; 2006.

[336]. Baker T.J., J.A. Charles, Effect of Second Phase Particles on the Mechanical Properties of Steel, Iron and Steel Institute, London, 1971, p. 79.

[337]. Allazadeh M.R., Garcia C.I., Alderson K.J., DeArdo A.J.; "Using NDT Image Processing Analysis to Study the Soundness and Cleanliness of Accelerated Cooled Continuously Cast Steel Slabs"; Materials Science & Technology 2008 Conference, pages 1853-1864.

[338]. Bruce Carter,_ Chuin-Shan Chen,_ L. Paul Chew,_ Nikos Chrisochoides,_ Guang R. Gao, Gerd Heber,_ Antony R. Ingraffea,_ Roland Krause,_ Chris Myers,_ Demian Nave,_ Keshav Pingali,_ Paul Stodghill,_ Stephen Vavasis,_ Paul A. Wawrzynek_; "Parallel FEM Simulation of Crack Propagation Challenges, Status, and Perspectives".

[339]. Randle V.; "The measurement of grain boundary geometry"; Inst physics pub., Bristol UK 1993.

[340]. Randle V.; "The role of coincidence site lattice in grain boundary engineering"; 1996, ISBN 1-86125-006-1.

[341]. Kameda J. McMahon C. J. ; "The Effects of Sb, Sn, and P on the Strength of Grain Boundaries in a Ni-Cr Steel"; Metallurgical Transactions, 1SSN 0360-2133/81/0112-003, V 12A, January 1981, pp31-37.

[342]. Yuan Z.-X., Jia J., Guo A.-M.,. Shen D.-D, Song S.-H.; "Cooling-induced tin segregation to grain boundaries in a low-carbon steel"; Pergamon, PII: S13 5 9-6 4 62 (0 2)0 03 5 7- 3, Scripta Materialiw 48 (2003) 203–206

[343]. Ishida T. Tekkoukai 1988;38(8).

[344]. Suzuki HG, Nishimura S, Yamaguchi S. Trans Iron Steel Inst Jpn 1982;22:48.

[345]. Hannerz NE. Trans Iron Steel Inst Jpn 1985;25:149.

[346]. Abushosha R, Vipond R, Mintz B. Mater Sci Technol 1991;7:1101.

[347]. Ohmura M. ISIJ Int 1997;37:255.

[348]. Faulkner RG. J Mater Sci 1981;16:373.

[349]. Doig P, Flewitt PEJ. Acta Metall 1981;29:1831.

[350]. Xu T-D, Song S-H. Acta Metall 1989;37:2499.

[351]. Song S-H, Xu T-D, Yuan Z-X. Acta Metall 1989;37:319.

[352]. Faulkner G.; "Non-equilibrium grain-boundary segregation in austenitic alloys"; Journal of Materials Science 16 (1981) 373-383.

[353]. M.P. SEAH and E. D. HONDROS, *lnt. Met. Rev.* 222 (1977) 262.

[354]. McMahon C.J., Jr.: Acta Metall., 1966, vol. 14, p. 839.

[355]. Jolly and P. Goux C.: Mem. Sci. Rev. Met., 1969, vol. 66, p. 605.

[356]. Dumoulin h., M. Foucault, M. Palmier, M. Wayman, M. Biscondi, and M. Guttman: Mere. Sci. Rev. Met., 1979, vol. 76, p. 187.

[357]. Xu, X-P and Needleman, A. "Numerical simulations of fast crack growth in brittle solids", Journal of the Mechanics and Physics of Solids, Vol. 42, pp. 1397-1434 (1994).

[358]. Alfano, G. and Crisfield, M.A., "Finite Element Interface Models for the Delamination Analysis of Laminated Composites: Mechanical and Computational Issues", International Journal for Numerical Methods in Engineering, Vol. 50, pp. 1701-1736 (2001).

[359]. http://www.efunda.com/

[360]. Brady, G.S., et al. (ed.) (1997), Materials Handbook, 14th ed., McGraw-Hill (New York).

[361]. Brandes, E.A., et al. (ed.) (1992), Smithells Metals Reference Book, 7th ed., Butterworth-Heinemann (UK).

[362]. Budinski, K.G., Budinski, M.K. (ed.) (1999), Engineering Materials: Properties and Selection, 6th ed., Prentice Hall (Upper Saddle River, NJ).

[363]. Callister, W.D. (1985), Materials Science and Engineering: An Introduction, John Wiley (New York).

[364]. Carter, G.F., Paul, D.E. (ed.) (1991), Materials Science and Engineering, ASM International (materials Park, OH).

[365]. Hu S Y, Ludwig M, Kizler P and Schmauder S 1998 Atomistic simulations of deformation and fracture of alpha-Fe Modelling Simul. Mater. Sci. Eng. 6 567.